Exploring Quantum Superpositions of Macroscopic Systems as Detectors for Particles

Eva Kilian

UNIVERSITY COLLEGE LONDON

Department of Physics and Astronomy

Submitted to University College London (UCL) in partial fulfilment of the requirements for the award of the degree of Doctor of Philosophy.

Primary supervisor:	**Prof. Sougato Bose**
Secondary supervisor:	**Prof. Peter Barker**
Examining committee:	**Dr. James Bateman**
	Prof. Dan Browne

Thesis submission date: **13th May 2023**

Declaration

I, **Eva Kilian**, confirm that the work presented in this thesis is my own. Where information has been derived from other sources, I confirm that this has been indicated in the thesis.
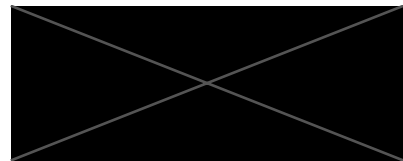
Eva Kilian

London, United Kingdom

13th May 2023

Abstract

I delve into the promising possibilities of using quantum superposition in macroscopic systems as detectors for weakly interacting relativistic particles. I take a closer look at the specific example of neutrinos with MeV-scale energy scattering from a solid object via neutral-current neutrino-nucleus scattering. Using parameters from a nuclear fission reactor as an (anti-)neutrino source, I establish the optimal spatial separation between the quantum superposed components for maximum sensitivity in detecting these particles. In addition, I study the temporal evolution of the sensing system, taking into account the effects of cooling and background suppression. Through my research, I demonstrate that a single gram scale mass placed in a superposition of spatial components separated by 10^{-14} m can yield a potentially measurable relative phase between quantum superposed components, opening up exciting possibilities for future applications. Furthermore, I investigate the broader implications of utilizing quantum superpositions in sensing. By analyzing the effects of scattering interactions between directional environments and systems in quantum superposition, I discovered that there exists an optimal superposition size for measuring incoming particles via a relative phase. An interesting feature of my research is the observation of a novel limiting behaviour in the properties of the system's density matrix, which is linked to the wavelength of the scatterer. This highlights the anisotropy of the environment and its impact on quantum sensing. As a platform for a practical realisation of macroscopic superpositions, I investigate an atom-nanoparticle system and discuss the possibility of

treating the nanoparticle as a spatial qubit. Overall, my thesis presents a comprehensive examination of the potential of quantum superposition in macroscopic systems as detectors for weakly interacting relativistic particles. It demonstrates that exploiting quantum mechanics for directional sensing offers unprecedented possibilities and has the potential to revolutionize the field of quantum sensing.

Impact Statement

The concept of quantum superposition has revolutionized our understanding of the microscopic world, and its potential impact extends far beyond theoretical physics. This impact statement highlights the transformative effects of utilizing quantum superposition as a tool for sensing and measurement across various fields. Harnessing the power of quantum superpositions has unlocked new possibilities in metrology, quantum computation, and recently particle physics. The work presented in this thesis illustrates the significance of research focused on utilizing macroscopic systems in quantum superposition as detectors for weakly interacting relativistic particles. By examining the explicit case of neutrinos with MeV-scale energy scattering from solid objects, valuable insights have been gained and only further promoted the vast applicability of quantum sensors to the exploration of open fundamental physics questions. Notably, I demonstrate the potential for detecting neutrino signatures via a measurable relative phase between quantum superposed components. Achieving this outcome requires careful consideration of factors such as spatial separation, cooling techniques, and background suppression. These findings provide a foundation for the development of innovative quantum sensing technologies that could revolutionize the fields of low energy neutrino and non-standard particle physics.

The secondary focus of this work is placed on exploring the scattering interactions of more general directional particulate environments with a system in a quantum superposition. By investigating this scenario, I have uncovered the existence of an "optimal superposition" size, which

may facilitate the design of superposition based experiments aiming to sense particles via coherent phases. The implications of the findings here presented are significant, as they contribute to the development of optimized quantum sensing strategies.

The study of an atom-nanoparticle system in ion-trap settings is particularly relevant in all of the above mentioned contexts, as it may lead to the creation of large-mass superpositions which can be used for the sensing of neutrinos, dark matter particles and gravitational effects.

Acknowledgements

I would like to express my deepest gratitude to my primary supervisor, Prof. Sougato Bose, for his guidance and support throughout my academic journey. His insightful feedback, unwavering passion for fundamental science, and patient encouragement, especially so of women in science, have been invaluable in shaping my research and developing my skills. Without his supervision, this achievement would not have been possible. Equally, I would like to thank Prof. Peter Barker for including me in regular meetings of his optomechanics group and providing the valuable viewpoint of an experimentalist. I also want to express my sincere appreciation for the supervision of Dr. Marko Toroš, whose willingness to engage in debates about even the most seemingly trivial formalistic subtleties, and whose commitment to jointly work out suitable solutions, even if these treacherous trivialities turn into figurative elephants, I highly value.

I am particularly grateful to my partner, Markus Rademacher, who has stood by my side throughout four years marked by a severe worsening of my chronic condition and has cared for me in a way I would have thought unthinkable, all while conducting his own doctoral studies. It is in part owed to his encouragement that I have gained the confidence to apply for prestigious conferences and career opportunities in physics. In this sense, I also want to thank Dr. Sofia Qvarfort for her advice to aim high and throw my hat in the ring for highly competitive academic positions. Lastly, I would like to express my gratitude to my parents Karl and Andrea Kilian, for accepting my desire to study a subject that is as foreign

to them as the nature of their professions is to me, my sister Romana Kilian and my close friends Julia and Nikola Mandl, all of whom are a constant source of strength and inspiration.

Contents

List of Figures

List of Tables

Research Paper Declaration Form

Referencing the doctoral candidate's own published work

First Paper

1. **1. For a research manuscript that has already been published** (if not yet published, please skip to section 2)**:**

   (a) **What is the title of the manuscript?**

   Requirements on quantum superpositions of macro-objects for sensing neutrinos

   (b) **Please include a link to or doi for the work:**

   `https://doi.org/10.1103/PhysRevResearch.5.023012`

   (c) **Where was the work published?**

   Physical Review Research

   (d) **Who published the work?**

   The American Physical Society

   (e) **When was the work published?**

   7 April 2023

   (f) **List the manuscript's authors in the order they appear on the publication:**

   Eva Kilian, Marko Toroš, Frank F. Deppisch, Ruben Saakyan,

and Sougato Bose

(g) **Was the work peer reviewed?**

Yes

(h) **Have you retained the copyright?**

Attribution 4.0 International (CC BY 4.0). This license permits unrestricted use, distribution, and reproduction in any medium, provided attribution to the author(s) and the published article's title, journal citation, and DOI are maintained.

(i) **Was an earlier form of the manuscript uploaded to a preprint server (e.g. medRxiv)? If 'Yes', please give a link or doi**

`https://doi.org/10.48550/arXiv.2204.13095`

If 'No', please seek permission from the relevant publisher and check the box next to the below statement:

⊠ *I acknowledge permission of the publisher named under 1d to include in this thesis portions of the publication named as included in 1c.*

2. **For a research manuscript prepared for publication but that has not yet been published** (if already published, please skip to section 3)**:**

(a) **What is the current title of the manuscript?**

(b) **Has the manuscript been uploaded to a preprint server 'e.g. medRxiv'?**

If 'Yes', please please give a link or doi:

(c) **Where is the work intended to be published?**

(d) **List the manuscript's authors in the intended authorship order:**

(e) **Stage of publication:**

3. **For multi-authored work, please give a statement of con-**

tribution covering all authors (if single-author, please skip to section 4)**:**

Eva Kilian designed the theoretical framework and performed the calculations and wrote the initial draft. Marko Toroš assisted with the computations. All authors edited and co-wrote the final manuscript. Marko Toroš, Frank F. Deppisch, Ruben Saakyan, and Sougato Bose gave supervision and advice during this work.

4. **In which chapter(s) of your thesis can this material be found?**

   Chapter 2

e-Signatures confirming that the information above is accurate (this form should be co-signed by the supervisor/ senior author unless this is not appropriate, e.g. if the paper was a single-author work)**:**

Candidate:
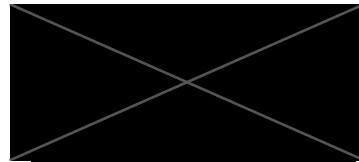
Eva Kilian

Date: 13th May 2023

Supervisor/Senior Author signature (where appropriate)**:**
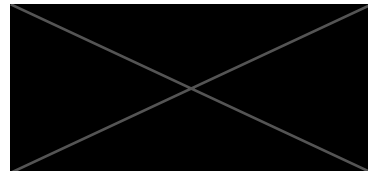
Sougato Bose

Date: 13th May 2023

Second Paper

1. **1. For a research manuscript that has already been published** (if not yet published, please skip to section 2)**:**

   (a) **What is the title of the manuscript?**

   (b) **Please include a link to or doi for the work:**

   (c) **Where was the work published?**

   (d) **Who published the work?**

   (e) **When was the work published?**

   (f) **List the manuscript's authors in the order they appear on the publication:**

   (g) **Was the work peer reviewd?**

   (h) **Have you retained the copyright?**

   (i) **Was an earlier form of the manuscript uploaded to a preprint server (e.g. medRxiv)? If 'Yes', please give a link or doi**

   If 'No', please seek permission from the relevant publisher and check the box next to the below statement:

   ☐ *I acknowledge permission of the publisher named under 1d to include in this thesis portions of the publication named as included in 1c.*

2. **For a research manuscript prepared for publication but that has not yet been published** (if already published, please skip to section 3)**:**

   (a) **What is the current title of the manuscript?**

   Optimal Superpositions for Particle Detection via Quantum Phase

   (b) **Has the manuscript been uploaded to a preprint server 'e.g. medRxiv'?**

If 'Yes', please please give a link or doi:

`https://doi.org/10.48550/arXiv.2307.15186`

(c) **Where is the work intended to be published?**

Physical Review Letters

(d) **List the manuscript's authors in the intended authorship order:**

Eva Kilian, Marko Toroš, P.F. Barker, and Sougato Bose

(e) **Stage of publication:**

In preparation for submission.

3. **For multi-authored work, please give a statement of contribution covering all authors** (if single-author, please skip to section 4)**:**

Eva Kilian designed the theoretical framework and performed the calculations and wrote the initial draft. Marko Toroš assisted with the computations. All authors edited and co-wrote the final manuscript. Marko Toroš, P.F. Barker, and Sougato Bose gave supervision and advice during this work.

4. **In which chapter(s) of your thesis can this material be found?**

Chapter 3

e-Signatures confirming that the information above is accurate (this form should be co-signed by the supervisor/ senior author unless this is not appropriate, e.g. if the paper was a single-author work)**:**

Candidate:
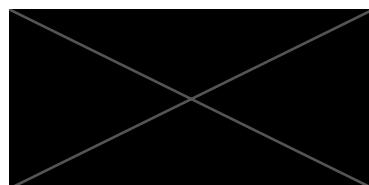
Eva Kilian

Date: 13th May 2023

Supervisor/Senior Author signature (where appropriate)**:**
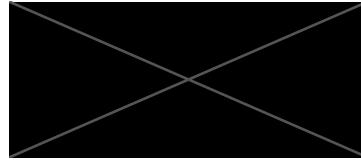
Sougato Bose

Date: 13th May 2023

Chapter 1

Introduction

Contents

1.1 Preamble

Cutting-edge quantum technologies offer immense potential for discovering long-predicted and yet unobserved features of fundamental theory.

Quantum sensors may capture information that classical sensors cannot capture, and their ability to detect extremely weak signatures makes them ideally suited for high-precision measurements. They offer unique advantages in answering questions on the limits of quantum theory, the nature of gravity, dark matter and dark energy, and the validity of numerous extensions to the standard model of particle physics.

This thesis is centred on the ambitious objective of addressing a specific of these fundamental and unanswered questions: Is it possible to sense elusive particles, particularly neutrinos, through large masses placed in quantum superposition? Suppose current technological limitations, especially with respect to the rapid decoherence of large mass quantum sensors, can be overcome in the near future. What minimum requirements would such detectors have to meet?

In this thesis, I address the above broad objectives through three pieces of original work. Firstly (as reported in Chapter 2), I develop a formalism to describe the time evolution of a sensing particle under the influence of neutrinos scattering from it. I find the parameter regimes required. Secondly (as reported in Chapter 3), I describe a general relationship between the directionality and wavelength of an environmental particle source and the emergence of an optimal window for the quantum sensor's superposition size. I find the tradeoff between coherent phase and decoherence as a function of the superposition size. Third (as reported in Chapter 4), I consider a specific protocol for the creation of large mass superpositions of nanoparticles through their interaction with atoms. I find that an atom and a nanoparticle in adjacent ion traps is a good setting for generating such superpositions.

Since the majority of the aspects discussed in this work require a metaphorical walk on a bridge between matter-wave interferometry and neutrino physics, with both of these fields equally vast in their depth and complexity, I aim to provide the reader with two reasonably distinct introductory

themes: one which is focused on matter-wave interferometry with atoms and large-mass objects and another which discusses neutrinos in the context of particle physics. Sections 1.2-1.5 will provide an overview of the former, and Sections 1.6-1.9 will delve into the latter topic.

1.2   Matter-Wave Interferometry for Fundamental Physics Research

The field of matter-wave interferometry was born in 1924 [1] when Louis de Broglie wrote about the then hypothetical wave-particle duality of massive particles of matter in his doctoral thesis. He proposed that, in a similar fashion to photons in Einstein's famous theory of light, a massive particle of a given momentum $p = mv$ may exhibit wave-like behaviour with a wavelength $\lambda_{dB} = \frac{h}{mv}$. As a consequence of this behaviour, massive matter particles shot onto double slits or other types of diffraction structures should result in the appearance of an interference pattern. Three short years thereafter, Davisson and Germer [2] confirmed de Broglie's notion by directing a beam of electrons at a crystalline target, resulting in the observation of a diffraction pattern in accordance with theoretical expectations. The first exploration of a matter-wave interferometry setup that incorporated the splitting and recombination an electron beam followed much later, in 1953 [3], involving an arrangement of three crystals which were used as amplitude beam-splitters. Interference of de Broglie waves of electrons in a double-slit experiment was first demonstrated in [4].

All matter-wave experiments share a commonality: they harness the wave-like nature of atoms [5, 6], molecules [7, 8], nanoparticles [9] and, at least conceptually, macroscopic composite objects of even larger masses and stimulate the development of quantum sensors capable of detecting

exceptionally weak signatures, for instance very low transfers of momentum. In general, interferometric experiments are based on the creation, coherent manipulation and subsequent measurement of quantum superpositions. Interference of the superposed wavepackets can be used to extract information from the system, such as fluctuations in the gravitational field which may appear in the form of a variation in the relative phases between the components of a spatial superposition [10, 11]. A relatively novel direction of fundamental physics research is the application of matter-wave interferometry to the sensing of particulate matter [12, 13]. While scattering interactions involving high momentum transfers to the sensor will lead to fast decoherence of the system, optomechanical sensors based on quantum superpositions may be ideal candidates for measuring rare events through small momentum transfers [14]. Important conceptual details for fundamental physics research and the sensing of neutrinos using matter-wave interferometers are presented in Sections 1.3-1.9.

1.3 Physical Realisation of Atomic Two-State Systems

Practical implementations of matter-wave interferometers necessitate the realisation of robust physical qubits[1] which are constructed from two orthogonal states of a quantum system. A simple and natural realisation of a well-defined qubit is a spin 1/2 system, such as an electron in a magnetic field [15], for which the spin projections along the field direction $|m_S = -\frac{1}{2}\rangle = |0\rangle$ and $|m_S = +\frac{1}{2}\rangle = |1\rangle$ are associated with the qubit basis states $|0\rangle$ and $|1\rangle$.

Continuous variable systems may equally be engineered as effective qubits. One possible way to design an atom as a two-state quantum sys-

---

[1]Physical qudits will not be discussed in this thesis.
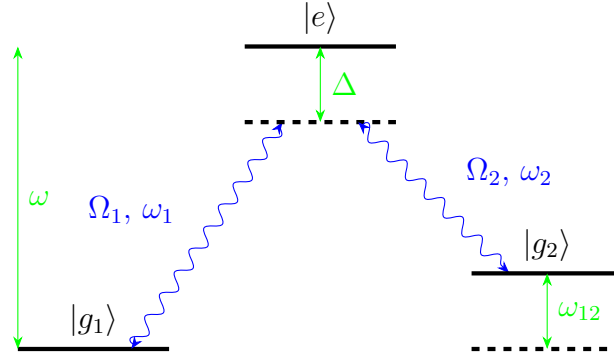
Figure 1.1: Depiction of an atomic three-level system with optically active transitions $|g_1\rangle \leftrightarrow |e\rangle$ and $|e\rangle \leftrightarrow |g_2\rangle$. The frequency difference of $|g_1\rangle$ and $|e\rangle$ is characterised by ω. The quantity Δ is a detuning from the frequency of the excited state $|e\rangle$. The frequencies $\omega_1 + \Delta$ and $\omega_2 + \Delta$ are associated with the transitions between $|g_1\rangle \leftrightarrow |e\rangle$ and $|e\rangle \leftrightarrow |g_2\rangle$ while Ω_1 and Ω_2 denote the corresponding coupling strengths of the lasers. The frequency ω_{12} corresponds to the frequency difference between the levels $|g_1\rangle$ and $|g_2\rangle$.

tem is to utilize its internal degrees of freedom, specifically its hyperfine ground and excited states. To illustrate how an internal superposition state of this kind can be induced in an atomic system, I will discuss a particular, classic example of the coherent interaction of an atom with laser light, where the atom is assumed to exhibit an energy level configuration which is termed a three-level Λ structure [16]. This structure is visualised schematically in Figure 1.1. It features two optically individually addressable hyperfine ground states $|g_1\rangle$ and $|g_2\rangle$ of similar energies E_{g_1} and $E_{g_2} = E_{g_1} + \hbar\omega_{12}$, which will be identified as the qubit, and an excited state $|e\rangle$ to which both hyperfine ground states couple through dipole transitions. Direct transitions between $|g_1\rangle$ and $|g_2\rangle$ are dipole-forbidden and the hyperfine ground states can not decay to other lower energy states via single-photon transitions. The quantities Ω_1 and Ω_2 are frequency measures of the dipolar interaction between the atom and the electromagnetic field of the laser light $V_{dip} = -\mathbf{E} \cdot \hat{\mathbf{d}}$, where $\hat{\mathbf{d}} = e\hat{\mathbf{r}}$ is the dipole operator and $\hat{\mathbf{r}}$ is the position operator of the electron. Ω_1 and Ω_2 are also known as Rabi frequencies. They define the coupling strengths of the two lasers prompting the transitions $|g_1\rangle \leftrightarrow |e\rangle$ and $|e\rangle \leftrightarrow |g_2\rangle$ and are given by $\Omega_j = \frac{\langle e|\hat{\mathbf{d}}|g_j\rangle \cdot \mathbf{E}}{\hbar}$. In this concrete example, both lasers

are detuned by an equal amount Δ from the transitions between the excited and ground states, a practice which is generally used in order to avoid resonant excitations to $|e\rangle$. Given a sufficiently large detuning Δ, two-photon transitions between the two hyperfine ground states are stimulated without populating the excited level, thus enabling the physical realisation of an ideal qubit. The ensuing oscillations occuring between $|g_1\rangle$ and $|g_2\rangle$ via the higher level $|e\rangle$ are also known as Raman transitions.

Suppose for now that the atom in the Λ configuration is interacting with classical light. The electromagnetic field is of the form

$$E_j = E_{0,j}\Big(\epsilon_j e^{i\omega_j t - i\mathbf{k}_j \mathbf{r}} + \epsilon_j^* e^{-i\omega_j t + i\mathbf{k}_j \mathbf{r}}\Big) \tag{1.3.1}$$

where $\mathbf{r}$ is the distance vector, $\mathbf{k}_j$ is the wave vector, ϵ_j are the field polarizations and $E_{0,j}$ the real field amplitudes of two different light fields, neglecting additional phases. For an atomic system located at $r = 0$, the expression simplifies to $E_j = E_{0,j}\Big(\epsilon_j e^{i\omega_j t} + \epsilon_j^* e^{-i\omega_j t}\Big)$. Using the definition of the Rabi frequency and associating g_1 with the zero energy, the total Hamiltonian can be expressed in the basis $|g_1\rangle, |g_2\rangle, |e\rangle$ as

$$H_\Lambda(t) = \hbar \begin{pmatrix} 0 & 0 & \Omega_1 \cos\omega_1 t \\ 0 & \omega_{12} & \Omega_2 \cos\omega_2 t \\ \Omega_1 \cos\omega_1 t & \Omega_2 \cos\omega_2 t & \omega. \end{pmatrix} \tag{1.3.2}$$

In order to eliminate the explicit time dependence, a transformation to the rotating frame can be used. This transformation of the Hamiltonian is of the form[2] $H' = UHU^\dagger + i\hbar U\frac{dU^\dagger}{dt}$. Switching to the rotating frame

---

[2]A result which can be recovered when looking at a transformation of the quantum state $|\psi'(t)\rangle = U(t)|\psi(t)\rangle$ and inserting it into the Schrödinger equation.

by employing the unitary transformation

$$U(t) = \begin{pmatrix} 1 & 0 & 0 \\ 0 & e^{-i(\omega_1 - \omega_2)t} & 0 \\ 0 & 0 & e^{-i\omega_2 t} \end{pmatrix} \tag{1.3.3}$$

one recovers the Hamiltonian

$$H'_\Lambda(t) = \frac{\hbar}{2} \begin{pmatrix} 0 & 0 & \Omega_1(1 + e^{2i\omega_1 t}) \\ 0 & 2(\omega_{12} + \omega_2 - \omega_1) & \Omega_2(1 + e^{2i\omega_2 t}) \\ \Omega_1(1 + e^{-2i\omega_1 t}) & \Omega_2(1 + e^{-2i\omega_2 t}) & 2(\omega - \omega_1). \end{pmatrix}$$

$$\tag{1.3.4}$$

The rotating wave approximation is then utilized to justify the elimination of fast rotating terms in the Hamiltonian.

$$H'_\Lambda = \frac{\hbar}{2} \begin{pmatrix} 0 & 0 & \Omega_1 \\ 0 & 2(\omega_{12} + \omega_2 - \omega_1) & \Omega_2 \\ \Omega_1 & \Omega_2 & 2(\omega - \omega_1). \end{pmatrix} \tag{1.3.5}$$

When the two light beams are equally detuned as depicted in Figure 1.1, where $\Delta_1 = \omega - \omega_1$ is equal to $\Delta_2 = \omega - \omega_2 - \omega_{12}$ and hence $\Delta_1 = \Delta_2 = \Delta$, and the detuning is regarded in the limit where $\Delta \gg \Omega_j$, this Hamiltonian can be treated in the context of time-independent degenerate perturbation theory. Following the perturbative treatment, the atom can then be described as an effective two-level system with the Hamiltonian becoming

$$H_{\text{eff}, \Delta \gg \Omega_j} = -\frac{\hbar}{4\Delta} \left(\Omega_1^2 |g_1\rangle\langle g_1| + \Omega_2^2 |g_2\rangle\langle g_2| \right) \tag{1.3.6}$$
$$- \hbar\Omega_{\text{eff}} \left(|g_1\rangle\langle g_2| + |g_2\rangle\langle g_1| \right)$$

where $\Omega_{\text{eff}} = \frac{\Omega_1 \Omega_2}{4\Delta}$ is an effective Rabi frequency. As is evident from the off-diagonal terms, the population oscillates between the two ground

states. Formulated in terms of Pauli operators Z and X, the Hamiltonian of Eq. (1.3.6) can also be written as

$$H_{\text{eff},\Delta\gg\Omega_j} = -\frac{\hbar}{4\Delta}\left(\frac{\Omega_1^2}{2}(\mathbb{I}+Z) + \frac{\Omega_2^2}{2}(\mathbb{I}-Z)\right) \qquad (1.3.7)$$
$$ - \hbar\Omega_{\text{eff}}X$$

where $Z = |g_1\rangle\langle g_1| - |g_2\rangle\langle g_2|$ and $X = |g_1\rangle\langle g_2| + |g_2\rangle\langle g_1|$ and $\mathbb{I}$ is the identity matrix. In approximate versions of the effective Hamiltonian, the term $-\frac{\hbar}{4\Delta}\left(\frac{\Omega_1^2+\Omega_2^2}{2}\right)\mathbb{I}$ is often neglected and $H_{\text{eff},\Delta\gg\Omega_j} \simeq -\frac{\hbar}{4\Delta}\left(\frac{\Omega_1^2-\Omega_2^2}{2}\right)Z - \hbar\Omega_{\text{eff}}X$. If $\Omega_1 = \Omega_2$, which is also the situation depicted in Figure 1.1, a perfect $\pi/2$ pulse for an atom initially in a state $|g_1\rangle$ can be realized by evolving the quantum state for a time $\tau = \frac{\pi}{2\Omega_{\text{eff}}}$.

The fully quantum treatment of atom-motional mode interactions requires a more subtle mathematical description [17]. For illustrative purposes, I will consider an ion in a linear Paul trap, whose center-of-mass motion is quantized due to the action of electric potentials and static electric fields. In such a scenario, the motion of the ion in the directions $i = x, y, z$ behaves to good approximation like a simple quantum harmonic oscillator with the Hamiltonian

$$H = \hbar\omega_i(\hat{N}_i + 1/2) \qquad (1.3.8)$$
$$\simeq \hbar\omega_i\hat{N}_i \qquad (1.3.9)$$

where $\hat{N}_i = a_i^\dagger a_i$ is the number operator and $a_i^\dagger = \sqrt{\frac{m\omega}{2\hbar}}(\hat{x}_i - \frac{i}{m\omega}\hat{p}_i)$, $a_i = \sqrt{\frac{m\omega}{2\hbar}}(\hat{x}_i + \frac{i}{m\omega}\hat{p}_i)$ are the common raising and lowering operators, with m being the mass of the ion. Identifying the z-axis as that running in parallel to the rods of the Paul trap, the position of the ion in the z-direction $\hat{z} = \delta_z(a_z^\dagger + a_z)$ and $\delta_z = \sqrt{\frac{\hbar}{2m\omega_z}}$ is the spread or uncertainty of the ground state. Importantly, the quantization of the motion introduces discrete vibrational states $|n\rangle$, which are eigenstates of the harmonic os-

cillator also termed Fock states or phonon number states.

The electromagnetic field is not quantized in this treatment and, for the sake of simplicity, will be treated here as a single mode radiation field propagating in the z-direction, polarized in x. It is written as

$$E_j = E_{0,j}\vec{e}_x\left(e^{i(\omega_j t - k_j \hat{z} + \phi_j)} + e^{-i(\omega_j t + k_j \hat{z} - \phi_j)}\right) \qquad (1.3.10)$$

where the position of the ion has been quantized, $\vec{e}_x$ is the unit vector in x and ϕ_j are the phases of the two lasers. The dipole operator component in the x-direction can be expressed as $\hat{d} = \sigma_+^{(j)}\langle e|d|g_j\rangle + \sigma_-^{(j)}\langle g_j|d|e\rangle$ with $\sigma_+^{(j)} = |e\rangle\langle g_j|$, $\sigma_-^{(j)} = |g_j\rangle\langle e|$. The interaction Hamiltonian

$$
\begin{aligned}
H_I = &-\hat{d}\cdot E \qquad (1.3.11)\\
&-\sum_{j=1,2}\left[E_{0,j}\left(e^{i(\omega_j t - k_j \hat{z} + \phi_j)} + e^{-i(\omega_j t + k_j \hat{z} - \phi_j)}\right)\right.\\
&\qquad\qquad \left.\left(\langle e|\hat{d}|g_j\rangle^*\sigma_+^{(j)} + \langle g_j|\hat{d}|e\rangle\sigma_-^{(j)}\right)\right]
\end{aligned}
$$

is accompanied by the Hamiltonian H_0 for the atom and motion

$$
\begin{aligned}
H_0 = &\hbar\omega_z a^\dagger a + \frac{\hbar\omega}{2}\left(|e\rangle\langle e| - |g_1\rangle\langle g_1|\right) \qquad (1.3.12)\\
&+ \frac{\hbar(\omega - \omega_{12})}{2}\left(|e\rangle\langle e| - |g_2\rangle\langle g_2|\right)
\end{aligned}
$$

where ω and ω_{12} are the transition frequencies shown in Figure 1.1. Now I am introducing an important distinction to the previous case. Instead of the lasers being equally detuned from the transitions to the excited level, the frequency difference $\omega_1 - \omega_2$ of the lasers is detuned by a further amount δ from the ground state difference ω_{12}. In the rotating frame,

the interaction Hamiltonian of Eq. (1.3.11) becomes

$$H_I = - E_{0,1}\left[\left(e^{i(\omega_1 t - k_1 \hat{z} + \phi_1)} + e^{-i(\omega_1 t + k_1 \hat{z} - \phi_1)}\right)\right. \tag{1.3.13}$$
$$\left.\left(d_1^* \sigma_+^{(1)} e^{i\omega t} + d_1 \sigma_-^{(1)} e^{-i\omega t}\right)\right]$$
$$- E_{0,2}\left[\left(e^{i(\omega_2 t - k_2 \hat{z} + \phi_2)} + e^{-i(\omega_2 t + k_2 \hat{z} - \phi_2)}\right)\right.$$
$$\left.\left(d_2^* \sigma_+^{(2)} e^{i(\omega - \omega_{12})t} + d_2 \sigma_-^{(2)} e^{-i(\omega - \omega_{12})t}\right)\right]$$

where $d_j = \langle e|\hat{d}|g_j\rangle$ has been used for notational convenience. The rotating wave approximation can then be used to drop fast-rotating terms in the Hamiltonian.

$$H_I = - E_{0,1}\left(e^{i((\omega_1 - \omega)t - k_1 \hat{z} + \phi_1)} d_1 \sigma_-^{(1)} + e^{-i((\omega_1 - \omega)t + k_1 \hat{z} - \phi_1)} d_1^* \sigma_+^{(1)}\right) \tag{1.3.14}$$
$$- E_{0,2}\left(e^{i((\omega_2 - \omega + \omega_{12})t - k_2 \hat{z} + \phi_2)} d_2 \sigma_-^{(2)} + e^{-i((\omega_2 - \omega + \omega_{12})t + k_2 \hat{z} - \phi_2)} d_2^* \sigma_+^{(2)}\right)$$

The phases ϕ_j can be used to compensate the complex parts of d_j, into which the sign can also be absorbed, allowing for the Hamiltonian to be rewritten in terms of the Rabi frequencies Ω_j. Due to the additional detuning δ, one obtains

$$H_I = \hbar\Omega_1\left(e^{-i(\Delta t + k_1 \hat{z})} \sigma_-^{(1)} + e^{i(\Delta t + k_1 \hat{z})} \sigma_+^{(1)}\right) \tag{1.3.15}$$
$$+ \hbar\Omega_2\left(e^{-i((\Delta - \delta)t + k_2 \hat{z})} \sigma_-^{(2)} + e^{i((\Delta - \delta)t + k_2 \hat{z})} \sigma_+^{(2)}\right)$$

An effective 2-level Hamiltonian can again be obtained through perturbative methods, yielding

$$H_{I,2D} = \hbar\frac{\Omega_1 \Omega_2}{4\Delta}\left(e^{-i(\tilde{k}\hat{z} - \delta t)} \sigma_- + e^{i(\tilde{k}\hat{z} - \delta t)} \sigma_+\right) \tag{1.3.16}$$

with $\tilde{k}$ now a difference vector and $\sigma_+ = |g_2\rangle\langle g_1|$, $\sigma_- = |g_1\rangle\langle g_2|$. At this stage, the quantization of the motion will play a more prominent role. In the interaction picture, $\hat{z} = \delta_z\left(ae^{-i\omega_z t} + a^\dagger e^{i\omega_z t}\right)$, with δ_z again denoting the zero-point motion of the ion. The Lamb-Dicke approximation

assumes that the light-induced coupling between the ion's motion and internal effective qubit levels is sufficiently small such that $\tilde{k}\delta_z = \eta \ll 1$. In this limit, one can hence expand the exponential functions, which, up to and including first order, results in the Hamiltonian

$$
\begin{aligned}
H_{I,LDA} =& \hbar \frac{\Omega_1 \Omega_2}{4\Delta} \Big(e^{i\delta t} \big(\mathbb{I} - i\eta \big(a e^{-i\omega_z t} + a^\dagger e^{i\omega_z t} \big) \big) \sigma_- \\
&+ e^{-i\delta t} \big(\mathbb{I} + i\eta \big(a e^{-i\omega_z t} + a^\dagger e^{i\omega_z t} \big) \big) \sigma_+ \Big).
\end{aligned}
\tag{1.3.17}
$$

For a blue-detuned laser, $\omega_z = \delta$ (the sign depends on the definition of δ) and

$$
H_{I,LDAb} = i\hbar\eta \frac{\Omega_1 \Omega_2}{4\Delta} \big(a^\dagger \sigma_+ - a\sigma_- \big).
\tag{1.3.18}
$$

For a red-detuned laser $\omega_z = -\delta$ and

$$
H_{I,LDAr} = i\hbar\eta \frac{\Omega_1 \Omega_2}{4\Delta} \big(a\sigma_+ - a^\dagger \sigma_- \big).
\tag{1.3.19}
$$

In this thesis, I will use the standard technique of combination (simultaneous driving) of the blue and red detuned transitions to generate Schrödinger Cat states of the atom. Combining the above terms together gives

$$
= \hbar\eta\Omega_{\text{eff}} \big(a + a^\dagger \big) \sigma_y
\tag{1.3.20}
$$

$$
= \hbar\eta \frac{\Omega_{\text{eff}}}{\delta_z} \hat{z}\sigma_y.
\tag{1.3.21}
$$

By choosing the laser phases appropriately, for example $\phi_{\text{red}} = 0$ and $\phi_{\text{blue}} = -\pi$, it is possible to change the ion operator to $\hat{p}_z$ and/or the atomic operator to σ_x. The above Hamiltonian acting on ionic states $|\sigma_y = +1\rangle$ and $|\sigma_y = -1\rangle$ for a time δt, will lead to opposite momentum

kicks in the z direction given by

$$= \hbar \eta \frac{\Omega_{\text{eff}}}{\delta_z} \delta t \tag{1.3.22}$$

$$= \hbar \tilde{k} \Omega_{\text{eff}} \delta t \tag{1.3.23}$$

Thus in a time of the order of one oscillation with the effective Rabi frequency Ω_{eff} of oscillation between $|g_1\rangle$ and $|g_2\rangle$, a momentum $\sim \hbar \tilde{k}$ is transferred to the ion. Slightly different ideas have also been proposed to generate the Schrödinger Cat states faster, as has been used in [18], where sequences of ultra-fast laser pulses applying spin-state dependent kicks (SDKs) to the ions have been used to achieve larger separations.

1.4 Atom Interferometry

Atoms are attractive platforms for matter-wave interferometry experiments [19], allowing for precision measurements of fundamental constants, including the fine structure constant α[20] and the gravitational constant G [21, 22], measurements of gravity gradients [23], gravitational field curvature [24] and local gravitational acceleration [25]. They can be manipulated by electrostatic, magnetic and electromagnetic fields and modern techniques such as laser-cooling and trapping offer excellent control over their internal degrees of freedom [7]. Importantly, both internal and external degrees of freedom can be utilized to construct interference experiments. While interference arises exclusively due to internal states in Ramsey interferometers, it may also develop as a consequence of relative phases accumulating between distinct physical paths or a combination of internal and external degrees of freedom [26].

The development and subsequent demonstration of the first atom interferometers dates back to the year of 1991, when Carnal and Mlynek [27] and Keith and others [28] built quantum mechanical analogues of Young-
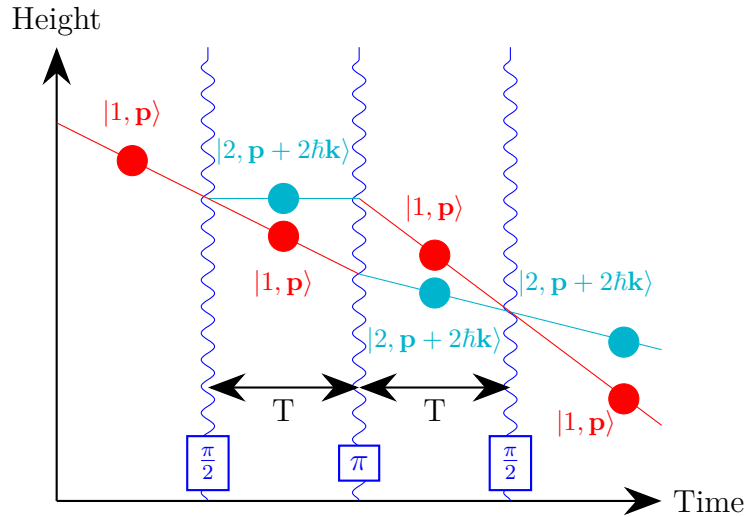
Figure 1.2: Illustration of a light-pulse atom interferometer based on a $\frac{\pi}{2} - \pi - \frac{\pi}{2}$ pulse sequence, using superpositions of internal and external degrees of freedom. The state $|j, \mathbf{p}_j\rangle$ denotes the internal level j and the external momentum p_j. Displayed are the key steps of the interferometric experiment, where the motional paths for the superposed components are coloured in red and turquoise. (1) The application of a $\frac{\pi}{2}$ laser pulse creates an initial superposition state $c_1|1, \mathbf{p}\rangle + c_2|2, \mathbf{p} + 2\hbar\mathbf{k}\rangle$. (2) The state evolves for a duration T, causing both parts of the velocity-separated superposition to propagate away from each other. (3) A π pulse is applied to swap the states $|1, \mathbf{p}\rangle \leftrightarrow |2, \mathbf{p} + 2\hbar\mathbf{k}\rangle$. (4) After another time interval T, a final $\frac{\pi}{2}$ pulse acts as a beamsplitter, mixing the wave-packets and completing the interferometry. The accumulated phase difference between the two parts of the superposition is measured, e.g., via fluorescence detection, to reveal the effects of gravitational and other forces on the atoms.

type optical double slit interferometers from micro-fabricated slits and transmission gratings, confirming the presumed wave-like behaviour of meta-stable Helium and Sodium atoms. Following their discoveries, a different category of atom interferometers [29, 30] using sequences of optical light pulses in order to coherently spatially separate the atoms were realised mere months thereafter. In the latter, the separation of the motional wave-packet of the quantum state is created due to the recoil following the interaction with an electromagnetic field. Together, these pioneering works laid the foundation for the development of a wide range of atom interferometry-based sensors, such as accelerometers [31], gyroscopes [32], and gravimeters [33]. The majority of present-day atom interferometers are reliant on atom-light interactions in some capacity [34,

35] and Raman transitions are used in order to place an atom initially prepared in a ground state in an equal superposition of internal states, but also external momentum states. As outlined in Section 1.3, two laser beams can be used to drive coherent transitions between two hyperfine states $|1\rangle$ and $|2\rangle$ when the frequency difference of the lasers matches $\hbar(\omega_{L1} - \omega_{L2}) = E_2 - E_1$ and the intermediate state remains scarcely populated. In the scenario where the two Raman beams are propagating in opposite directions, the absorption of a photon with momentum $\hbar\mathbf{k_1}$ and stimulated emission of one with momentum $\mathbf{k}_2 \simeq -\mathbf{k}_1$ causes the atom to recoil with twice the momentum kick in the same direction. By applying a suitable laser pulse for a duration $\tau_{\text{in}} = \frac{\pi}{2\Omega_{\text{eff}}}$, turning it off after a quarter oscillation, an initial superposition state of the form $c_1|1, \mathbf{p}\rangle + c_2|2, \mathbf{p} + 2\hbar\mathbf{k}\rangle$ is created. Many atom interferometers then use a basic pulse sequence $\frac{\pi}{2} - \pi - \frac{\pi}{2}$ like the one depicted in Figure 1.2 or a modified version thereof. In schemes using the aforementioned pulse sequence, following the preparation of the superposition, the state evolves for a duration T, causing both parts of the velocity-separated superposition to propagate away from each other. A π pulse is applied thereafter to swap the states $|1, \mathbf{p}\rangle \leftrightarrow |2, \mathbf{p} + 2\hbar\mathbf{k}\rangle$. Following the passage of a further time interval T, a last $\frac{\pi}{2}$ pulse takes on the role of a beamsplitter, mixing the wave-packets and completing the interferometry. The phase difference accumulated between the two parts of the superposition can be inferred by measuring the internal states of multiple atoms in the output ports, for example via fluorescence detection. Gravitational and other force effects may be reflected in the deviations in the measured relative phases.

In recent years, Stern-Gerlach type interferometers for freely propagating single atoms [36–38], in which instead of light, magnetic gradient fields are employed to control the atoms during their flight through the

interferometer, have gained attention. After the initial application of a $\pi/2$ radio frequency pulse, which is used to create an internal spin-state superposition of the atoms, four magnetic field gradient pulses are used to split, stop, reverse and stop to recombine the spin-coupled external position and momentum states. A popular candidate for the practical realisation of such interferometers is Rubidium. Most modern Stern-Gerlach type atom interferometers are using a Bose-Einstein condensate of ^{87}Rb atoms, initialized in equal superpositions of the two spin states $|F = 2, m_f = 2\rangle$ and $|F = 2, m_f = 1\rangle$ and magnetic field gradients produced by currents through gold wires on an atom chip. The Rubidium atoms are initially confined in a magnetic trap below the atom chip and subsequently released, while a homogeneous magnetic bias field in the y-direction is applied to create the effective two-level system (coupling to the y-direction of the spin). Following the preparation of the equal superposition state via RF pulses, a first magnetic field gradient pulse creates a state-dependent force $F_j = \mu_j \partial B_y/\partial z \mathbf{e_z}$ on the atoms, with μ_j being the mean magnetic dipole moment of state $|j\rangle$. After a delay time T_d, two further magentic gradient pulses of equal duration but opposite polarity are applied, such that the momentum difference is compensated and the direction of motion is effectively reversed. After a second delay time T_d, a fourth gradient pulse matching the polarity of the first one is used to close the interferometer in both momentum and position. The experimentally achieved visibilities of current-state of the art Stern-Gerlach interferometers for weak momentum-splitting are high (>95%) [39], but the recombination accuracy of the wave packets still presents a challenge.

1.5 Large-Mass Interferometry

In addition to measurements of fundamental constants and studies of gravitational and collapse models, a further key objective for tests of

fundamental theory is the generation of macroscopic quantum superpositions. As a natural extension of early interference experiments with electrons [4, 40], neutrons [41] and atoms [27], the field of matter-wave interferometry has expanded and prompted the development of experiments based on the delocalisation and interference of matter-waves of macromolecules and composite macroscopic objects of much larger masses.

An important experimental milestone was reached when the first diffraction of hot C_{60} and C_{70} fullerenes at mechanical [42] and optical [43] gratings demonstrated the emergence of an interference pattern. Subsequently, Talbot-Lau interferometers for fullerenes, which did not require the collimation of the inital molecular beam to achieve separation of the diffraction orders, were developed. These types of interferometers are based on the Talbot-Lau effect[3], which arises due to Fresnel-diffraction. Using such interferometers, the heaviest objects shown to exhibit matter-wave interference to date are molecules consisting of up to 2000 atoms [44]. Whether there exists a fundamental limit of the macroscopic scales at which quantum effects can at most be observed, a limit to the size or the mass of an object in superposition, is presently an open question.

One emerging platform to access unprecedented scales of large-mass superpositions are levitated optomechanical systems [45]. These sensors consist of mechanical objects confined by intense optical, electric quadrupole or magnetic fields. They offer a high degree of control over the sensing particle's translational and rotational degrees of freedom and con-

---

[3]The Talbot effect occurs when a coherent source of particles pass through a periodic structure. It leads to a self-imaging pattern of the original grating due to constructive interference at specific distances $L_T = d^2/\lambda$ of the Talbot length with d being the grating constant and λ the wavelength or de Broglie wavelength. The repetition happens at both even and odd multiples, but for a plane wave travelling along z and a grating structure in the x, y plane is shifted in x at odd multiples by an amount $d/2$. The Talbot-Lau effect is a similar self-imaging effect for incoherent sources.

stitute a powerful quantum technology for precise measurements of accelerations and forces. The scheme presented in [46] extends Talbot-Lau interferometry to mass regimes of $m > 10^6$ amu. In [47], a Stern-Gerlach Ramsey interferometer for large mass objects of up to $m \sim 10^9$ amu featuring an embedded single spin, with the exemplary candidate being a nanodiamond crystal with a spin-1 nitrogen-vacancy center, is introduced.

Based on the possibility to create meso- and macroscopic superpositions, schemes relying on a combination of two adjacent matter-wave interferometers have been proposed for tests of quantum gravity theories only recently [48, 49]. The underlying assumption of these proposals is that if the two masses in spatial superposition of both interferometers become entangled due to an interaction with the gravitational field, this mediating field must necessarily be quantized, since local operations and classical communication (LOCC) can only account for local operations on each mass and classical communication between them, but LOCC alone cannot entangle the test masses. Large-mass superpositions of levitated objects [46, 50] have also become highly topical in particle physics and dark matter searches, mainly since other classical physics-based experiments such as CDMS or CRESST are insensitive to low-mass dark matter candidates. The use of massive quantum superpositions for directional dark matter searches is discussed in [13, 14, 51]. The sensing of neutrinos through quantum superpositions is presented and discussed extensively in Section 2.

1.6   Neutrinos - A very brief History

In 1930, Wolfgang Pauli postulated the existence of a particle he originally termed the *neutron*[52] in order to explain a most curious experimental observation – an apparent violation of the principle of energy

conservation. It was known at the time that when a nuclear isotope such as Tritium undergoes beta-decay,

$$^3_1\text{H} \rightarrow ^3_2\text{He} + e^-$$

(1.6.1)

one of its neutrons transforms to a proton under the emission of an electron. The law of energy conservation would then require the emitted electron to have a specific kinetic energy, which should have been precisely defined through the difference between the Tritium and Helium rest masses and kinetic energies. In addition, the conservation of momentum should have resulted in the electron and Helium having equal and opposite momenta [53]. Upon measuring the kinetic energies of emitted electrons however, instead of the predicted monochromatic spectrum for the electron energy, a continuous spectrum was recorded. There was also a discrepancy in the conservation of angular momentum, since experimental evidence implied that a mother nucleus of integer spin would decay to a daughter nucleus of integer spin, which could not be consistently explained given the electron's spin $\frac{1}{2}$.

Circumventing the notion of a violation of several conservation laws, Pauli proposed the existence of an undetected third particle of low mass and neutral electric charge. When Enrico Fermi further developed the theory of beta decay, he included this elusive particle in his description, renaming it *neutrino* [54]. Following this new formulation, the beta decay process of a neutron could be described as

$$n \rightarrow p + e^- + \bar{\nu}_e.$$

(1.6.2)

It would take until 1956 for the existence of the neutrino to be finally confirmed experimentally by Cowan and Reines [55] through the detection

reaction

$$\bar{\nu}_e + p \rightarrow e^+ + n, \tag{1.6.3}$$

which represents what is known as inverse beta decay. Subsequent experiments on the nature of neutrinos demonstrated the difference between the flavour states ν_e, ν_μ and ν_τ, parity violation in weak interactions, the neutrino's helicity of $\mathcal{H}(\nu) = \frac{\vec{\sigma} \cdot \vec{p}}{|\vec{\sigma}||\vec{p}|} = -1$, the existence of weak neutral currents and the weak gauge bosons $W^\pm$, Z.

While Fermi was first to provide a theoretical description of the weak interaction in the form of a contact interaction through his work on beta decay, Glashow, Weinberg and Salam developed a model for the electroweak interaction, mediated by particles, that became an integral part of what is now commonly referred to as the Standard Model (SM) of particle physics [56–58].

1.7 Neutrinos in the Standard Model

The SM is a renormalisable[4] quantum field theory living in Minkowski space [53, 59] that satisfies special relativity and has its own internal symmetries. It is invariant under transformations of the group

$$\mathcal{G}_{SM} = SU(3) \times SU(2) \times U(1), \tag{1.7.1}$$

where $SU(3)$ is associated with the colour group of quantum chromodynamics, $SU(2)$ with the weak isospin and $U(1)$ with hypercharge. The symmetry group for the electro-weak section is

$$\mathcal{G}_{EW} = SU(2) \times U(1). \tag{1.7.2}$$

---

[4]a field theory is renormalisable if divergences (infinities) can be removed from physical observables

$$\begin{pmatrix} \nu_e \\ e \end{pmatrix}_L \Bigg| \begin{pmatrix} \nu_\mu \\ \mu \end{pmatrix}_L \Bigg| \begin{pmatrix} \nu_\tau \\ \tau \end{pmatrix}_L$$
$$e_R \quad \Big| \quad \mu_R \quad \Big| \quad \tau_R$$

Table 1.1: Lepton content of the SM. Electrons e, muons μ, tauons τ and three types of neutrinos $\nu_{e,\mu,\tau}$ are grouped into three generations and displayed from left to right in ascending order with respect to the electron, muon and tauon masses. Left-handed leptons (indexed with the subscript L) are arranged as doublets whereas right-handed leptons (indexed with a subscript R) are represented as singlets.

Each particle in the SM is labelled by how it transforms under a specific representation of the group $\mathcal{G}_{SM}$. These representations are typically labelled in the order $(SU(3), SU(2), U(1))$. Fermionic particles of spin $1/2$ that transform trivially under the colour group, meaning that they do not interact with the strong force, are termed leptons. Left-handed leptons of the representation $(1, 2, -\frac{1}{2})$, where the first two indices indicate the dimension of a quantum field's representation under $SU(3)$ and $SU(2)$ and the last index represents the charge under $U(1)$, are distinct from right-handed leptons with $(1, 1, +1)$ in the SM. Notably, the left-handed leptons transform as 2-component vectors (doublets), whereas the right-handed leptons are arranged as singlets as is illustrated in Table 1.1. In the earliest versions of the SM, there are no right-handed neutrino singlets, since, in accordance with the first experimental observations, long before the resolution of the solar neutrino problem, the left-handed neutrinos were assumed to be massless.

The mathematical concept through which most particles in the SM gain mass is spontaneous symmetry breaking of a gauge symmetry via the Higgs mechanism[5]. To illustrate how the gauge bosons for the electroweak interaction acquire mass [59] through the breaking of $SU(2) \times U(1)$ to $U(1)$, let φ denote the complex scalar Higgs-field and $(D_\mu \varphi)_i = \partial_\mu \varphi_i - i[g_2 A_\mu^a T^a + g_1 B_\mu Y]_i^j \varphi_j$ its covariant derivative, with $T^a = \frac{1}{2}\sigma^a$ and σ^a as

---

[5]Gauge-independent formulations of the Higgs mechanism were later developed by Higgs and Kibble.

the Pauli matrices and the hypercharge generator $Y = -\frac{1}{2}I$. The field φ is further assumed to have a potential $V(\varphi) = \frac{1}{4}\lambda(\varphi^\dagger\varphi - \frac{1}{2}v^2)^2$, where $v^2 = 4|m^2|/\lambda$. Formally, up to a scaling factor, this is equivalent to an often used rewritten version of the "Mexican hat-shaped" potential as $\tilde{V}(\varphi) = -\mu^2\varphi^\dagger\varphi + \lambda(\varphi^\dagger\varphi)^2$, where $-\mu^2$ is interpreted as a negative mass. Disregarding, for the sake of the argument, the fact that the Higgs field is a two-component quantity and looking only at one field component, it becomes evident that the minimum of the potential $\tilde{V}(\varphi)$ results in a ground state, and thus a vacuum expectation value for the field component, that is not zero. Instead, the minimum lies on a circle where $\langle 0|\varphi(x)|0\rangle = -\mu/\sqrt{\lambda} = v/\sqrt{2}$. As a consequence of this observation, a particular configuration for the Higgs doublet is chosen and defined as the vacuum state

$$\varphi_0 = \frac{1}{\sqrt{2}}\begin{pmatrix} 0 \\ v \end{pmatrix}. \tag{1.7.3}$$

In addition to the potential term, the kinetic term for the field φ is recovered via $-(D^\mu\varphi)^\dagger D_\mu\varphi$. Noting that

$$g_2 A_\mu^a T^a + g_1 B_\mu Y = \frac{1}{2}\begin{pmatrix} g_2 A_\mu^3 - g_1 B_\mu & g_2(A_\mu^1 - iA_\mu^2) \\ g_2(A_\mu^1 + iA_\mu^2) & -g_2 A_\mu^3 - g_1 B_\mu \end{pmatrix} \tag{1.7.4}$$

inserting the covariant derivate into the kinetic part of the Lagrangian for the Higgs field taken at the vacuum expectation value results, after rigorous computation, in the emergence of a mass term

$$\mathcal{L}_{mass} = -\frac{(g_2 v)^2}{4}W^{+\mu}W_\mu^- - \frac{(g_2 v)^2}{8\cos^2\theta_w}Z^\mu Z_\mu \tag{1.7.5}$$

where the fields Z_μ and $W_\mu^\pm$ come from a redefinition of the terms in Eq. (1.7.4) as $Z_\mu = \cos\theta_w A_\mu^3 - \sin\theta_w B_\mu$, $W^\pm = \frac{1}{\sqrt{2}}(A_\mu^1 \mp iA_\mu^2)$ and $A_\mu = \sin\theta_w A_\mu^3 + \cos\theta_w B_\mu$ with $\theta_w = \tan^{-1}(g_1/g_2)$ defining what is known

as the weak mixing angle. Missing in this mass Lagrangian is the field A_μ, which remains massless and implies that one of the symmetry subgroups is unbroken, specifically the $U(1)$ charge conservation symmetry (implies photon and gluons remain massless). The remaining terms in this part of the Lagrangian are condensed into

$$\mathcal{L}_{mass} = -M_W^2 W^{+\mu} W_\mu^- - \frac{M_Z^2}{2} Z^\mu Z_\mu \tag{1.7.6}$$

and describe the observed masses $M_W^2 = \frac{g_2 v}{2}$ and $M_Z^2 = \frac{M_W}{\cos\theta_w}$ of the Z^0 and $W^\pm$ exchange particles. From experiment, these are estimated to be $M_W \sim 80.4\text{GeV}$ and $M_Z \sim 91.2\text{GeV}$.

Since all fermions, including neutrinos, would still be massless at this point in the theory, it is desirable to find an extension term that can be added to the electroweak sector Lagrangian and similarly result in the appearance of mass terms while being (initially) invariant under $SU(2)$ and $U(1)$ transformations. Excluding neutrinos, this is achieved for all other fermions through the introduction of Yukawa coupling terms. For the case of electrons [60], the coupling term looks like

$$\mathcal{L}_{\text{Yukawa}} = -c_e\Big(\bar{e}_R \varphi^\dagger \begin{pmatrix} \nu_{eL} \\ e_L \end{pmatrix} + (\bar{\nu}_e, \bar{e}_L \varphi e_R)\Big) \tag{1.7.7}$$

and with φ again being replaced by its vacuum expectation value, the symmetry will be broken and the Lagrangian reads

$$\mathcal{L}_{\text{Yukawa}} = -\frac{c_e}{\sqrt{2}}\Big(\bar{e}_R v e_L + \bar{e}_L v e_R)\Big) \tag{1.7.8}$$

$$= -c_e \frac{v}{\sqrt{2}} \bar{e} e \tag{1.7.9}$$

with c_e an arbitrary coupling constant and the mass of the electron following $m_e = c_e \frac{v}{\sqrt{2}}$. Equivalently, the doublets and singlets of the other fermions are combined with the Higgs doublet to obtain mass terms. Neutrinos again remain without mass due to the absence of righthanded

ν_R singlets. In principle, the masses could be generated by including three generations of ν_R in the particle content, but until the observation of neutrino oscillations, it was not a necessity to account for the possibility of massive neutrinos.

In the SM description, the equation of motion for a spin-$\frac{1}{2}$ particle is the (Lorentz-invariant) Dirac equation

$$(i\gamma^\mu \partial_\mu - m)\psi(x) = 0 \tag{1.7.10}$$

in natural units, where γ^μ are Dirac spin matrices denoted as

$$\gamma^0 = \begin{pmatrix} 0 & 1 \\ 1 & 0 \end{pmatrix}, \qquad \gamma^i = \begin{pmatrix} 0 & \sigma^i \\ -\sigma^i & 0 \end{pmatrix} \tag{1.7.11}$$

in the chiral representation and σ^i are the Pauli matrices. The fields ψ transforming under boosts and rotations constructed from these Dirac matrices are sometimes termed Dirac spinors. Free particle solutions satisfying the Dirac equation can be found by writing the Dirac fields in terms of plane waves $\psi(x) = u(p)e^{-ip\cdot x}$ for $p^0 > 0$ and $\psi(x) = v(p)e^{+ip\cdot x}$ for $p^0 < 0$ and inserting them into the equation, noting that p^0 is the first component of the four-momentum $p^\mu = (\mathrm{E}/c, \mathbf{p}_x, \mathbf{p}_y, \mathbf{p}_z)$. Two linearly independent solutions for $u(p)$ and $v(p)$ are found for both the positive and negative frequency case

$$u^s(p) = \begin{pmatrix} \sqrt{p \cdot \sigma}\,\xi^s \\ \sqrt{p \cdot \bar{\sigma}}\,\xi^s \end{pmatrix}, \qquad v^s(p) = \begin{pmatrix} \sqrt{p \cdot \sigma}\,\eta^s \\ -\sqrt{p \cdot \bar{\sigma}}\,\eta^s \end{pmatrix} \tag{1.7.12}$$

where $\bar{\sigma} = (\mathbb{I}, -\sigma^i)$ and ξ^s and η^s are two-component spinors. The label $s = 1, 2$ indicates the two spin-orientations spin "up" and spin "down" of the physical states. To give an example for ξ^s, the spinor basis is often chosen as eigenstates of the Pauli matrix σ^3, $\xi^1 = (0, 1)^T$, $\xi^2 = (1, 0)^T$ but

other basis choices are equally possible. Regardless of the actual choice, the solutions fulfil the normalization conditions $u(p)^{r\dagger}u(p)^s = 2E_{\mathbf{p}}\delta^{rs}$ and $v(p)^{r\dagger}v(p)^s = 2E_{\mathbf{p}}\delta^{rs}$. Another observation that can be made and understood in light of the form of the solutions is that the spinors can be reduced to two separate blocks of two-component objects, hence

$$\psi = \begin{pmatrix} \psi_L \\ \psi_R \end{pmatrix} \tag{1.7.13}$$

which are left-handed and right-handed chiral spinor components. These components can also be projected out from ψ by applying the projection operators $P_{R,L} = \frac{1 \pm \gamma_5}{2}$

$$\psi_L = \frac{1 - \gamma_5}{2}\psi \tag{1.7.14}$$

$$\psi_R = \frac{1 + \gamma_5}{2}\psi. \tag{1.7.15}$$

with $\gamma_5 = i\gamma_0\gamma_1\gamma_2\gamma_3$. In the case of massless neutrinos, $m = 0$ and the Dirac equation for ψ_L and ψ_R decouples into two Weyl equations

$$i\frac{\partial}{\partial x^0}\psi_R = i\sigma_i\frac{\partial}{\partial x^i}\psi_R \tag{1.7.16}$$

$$i\frac{\partial}{\partial x^0}\psi_L = -i\sigma_i\frac{\partial}{\partial x^i}\psi_L. \tag{1.7.17}$$

It shall be noted that for the case $m = 0$, chirality, which is defined through the eigenvalues of the eigenequations $\gamma_5\psi_{R,L} = \pm\psi_{R,L}$, and helicity are the same. The projection operators $P_{R,L}$ are then intimately tied to the notion of helicity, since P_L projects out left-handed (spin and direction of motion are anti-parallel and $H = -1$) particles and P_R right-handed anti-particles (spin and direction of motion are parallel and $H = +1$). For massive fermions, there would be no decoupling and chirality and helicity are not identical. Charge conjugation $\psi^c = C\psi C^{-1} = \eta_c C(\bar{\psi}^T)$, where the transpose of the conjugate field is $\bar{\psi}^T = (\psi^\dagger\gamma^0)^T$ and η_c is a phase factor, of Dirac spinors interchanges

particles with antiparticles. For the special case of electrically neutral fermions, it is also possible to define a field that is its own charge conjugate $\psi^C = \psi$ and still obeys the Dirac equation by introducing a redefinition of the γ matrices where each of the matrices is complex, effectively rendering all solutions to be real. Fermions with this property are termed Majorana fermions and particles of this type are their own antiparticles. The distinction between the two types of Dirac and Majorana fermions became relevant when the observation of neutrino oscillations implied a non-zero restmass. To date, none of the two possibilities of the neutrino being either Majorana or Dirac particle have been excluded.

1.8 Neutrino Oscillations

Oscillation experiments regarding the nature of quarks and neutrinos suggest that while the flavour eigenstate of a particle may be observed, these eigenstates should not be considered identical to mass eigenstates, which are eigenstates of the free Hamiltonian. Instead, the flavour eigenstate may arise as a result of a mixing in the mass eigenstates. For neutrinos, this mixing is formally described by the unitary Pontecorvo–Maki–Nakagawa–Sakata (PMNS) matrix

$$
\begin{pmatrix} \nu_e \\ \nu_\mu \\ \nu_\tau \end{pmatrix} = \begin{pmatrix} U_{e1} & U_{e2} & U_{e3} \\ U_{\mu 1} & U_{\mu 2} & U_{\mu 3} \\ U_{\tau 1} & U_{\tau 2} & U_{\tau 3} \end{pmatrix} \cdot \begin{pmatrix} \nu_1 \\ \nu_2 \\ \nu_3 \end{pmatrix} \tag{1.8.1}
$$

and its elements $U_{a,i}$ where $a = \{e, \mu, \tau\}$ labelling the flavours and $i = \{1, 2, 3\}$ labelling the masses can be interpreted as the probabilities of measuring a neutrino in a mass eigenstate $\nu_{i=1,2,3}$ in a flavour eigenstate $\nu_{a=e,\mu,\tau}$. The theory of neutrinos changing their flavour after travelling long distances is widely accepted. It solves the solar neutrino problem, which is a discrepancy between actual and predicted neutrino fluxes from the sun. When measured on Earth, detectors sensitive to

interactions with electron neutrinos detect less than the expected fluxes calculated from solar models. The influence of neutrino oscillations has been disregarded in Chapter 2, since the quantum sensor is assumed to be placed at very short distances $d \sim 20\mathrm{m}$ away from a neutrino reactor source, where the effects of neutrino oscillations are considered negligible, since > 0.5 km length baselines are typically required to detect significant flavour oscillations [61].

1.9   Neutrinos and their Interactions with Matter

As is briefly discussed in Chapter 1.7, the existence of gauge bosons Z^0 and $W^{\pm}$ was already postulated in early formulations of the SM. These bosons are mediators of electroweak interactions, through which neutrinos can interact with matter. Standard neutrino interactions through the weak force can be grouped loosely into two main categories: interactions involving charged (CC) and neutral currents (NC). Couplings to the Z boson are neutral current interactions that do not involve a transfer of electric charge. Interactions mediated by $W^{\pm}$ do involve a transfer of charge and are hence termed charged current interactions. The full derivation of the Lagrangian describing weak leptonic sector interactions is extensive and will therefore not be discussed in this introduction, it can however be found in reference [59]. The respective Lagrangians for neutrino charged and neutral interactions are of the form

$$\mathcal{L}_{NC} = -\frac{g}{2\cos\theta_W} J_Z^{\mu} Z_{\mu} \tag{1.9.1}$$

$$\mathcal{L}_{CC} = -\frac{g}{2\sqrt{2}}\left(J_W^{\mu} W_{\mu} + J_W^{\mu\dagger} W_W^{\dagger} \right) \tag{1.9.2}$$

where g is a dimensionless coupling constant and

$$J_Z^\mu = 2 \sum_{a=e,\mu,\tau} g_L^\nu \bar{\nu}_{aL} \gamma^\mu \nu_{aL} + g_L^f l_{a,L} \gamma^\mu l_{aL} + g_R^f \bar{l}_{aR} \gamma^\mu l_{aR} \qquad (1.9.3)$$

$$J_W^\mu = 2 \sum_{a=e,\mu,\tau} \bar{\nu}_{aL} \gamma^\mu l_{aL} \qquad (1.9.4)$$

are neutral and charged leptonic currents with left-handed and right-handed leptonic fields $\nu_{aL(R)}$ and $l_{aL(R)}$ for the neutrino and other leptons. The constants g_L^ν, g_L^f and g_R^f similarly are couplings for processes involving interactions with the respective fields. The structure of neutrino interactions with charged leptons already contains an intrinsic feature of the weak interaction. Only left-handed neutrinos interact and they do so exclusively with left-handed components of the other leptons, since terms involving the right-handed projections of lepton spinors $\bar{\nu}_L \gamma^\mu \frac{1}{2}(1+\gamma_5)\psi_a = 0$. The general structure $\bar{\psi}\gamma^\mu(1-\gamma_5)\psi$ as a combination of an object transforming as a vector ($\bar{\psi}\gamma^\mu\psi$) and an object transforming as an axial vector ($\bar{\psi}\gamma^\mu\gamma_5\psi$) under Lorentz transformations is the characteristic $V-A$ structure of weak interactions, originating from $V-A$ theory, which accurately described experimental observations.

Instead of a grouping into CC and NC interactions, neutrino scattering processes can also be classified into coherent and incoherent processes [62]. In the low energy regime, where the neutrino's energy E_ν is on the order of a few MeV, neutrinos may coherently scatter from an entire nucleus

$$\nu + A_N^Z \rightarrow \nu + A_N^Z \qquad (1.9.5)$$

via a neutral current process. The condition of coherence is satisfied so long as the transferred momentum q is sufficiently small compared to the nucleus' radius r and $q \cdot r \ll 1$. Since this type of interaction is the dominant neutrino-matter interaction process in the low-energy regime, which

is owed to a coherent enhancement factor in the cross section that scales as the square of the number of neutrons in the target nucleus, it is the process guiding the analysis in Chapter 2, where the scenario of reactor neutrinos scattering from a quantum superposition has been treated using an open quantum systems approach. Accordingly, the corresponding cross-section and computational details are described in Chapter 2.

Neutrinos can also elastically scatter from electrons via charged and neutral currents and such signatures are useful for the detection of solar neutrinos through Cherenkov detectors. Another possible interaction in the low-energy regime is neutrino capture on radioactive nuclei, an exothermic reaction $\nu + A_N^Z \rightarrow e^- + A_{N-1}^{Z+1}$ similar to beta decay. Inverse beta decay $\bar{\nu} + p \rightarrow e^+ + n$ is of particular historical relevance and a further likely interaction to be observed in the low energy regime. While there are numerous other possible interactions of neutrinos with matter, those that have been mentioned are among the most prevailing, with the shared commonality that all of them have exceptionally small cross-sections of typically much less than $10^{-38}\,\mathrm{cm}^2$ in the sector $E_\nu < 10$ MeV since for most processes $\sigma \propto E_\nu^2$.

1.10   Neutrino Sources

The universe offers a rich variety of neutrino sources, each emitting particles of vastly different energies and providing equally variable fluxes. Since a key objective of this thesis is to determine the ability of interferometry setups based on meso- and macroscale levitated objects to detect neutrinos, only a few of these sources, visually represented in Fig. 1.3, will suitably match the aim. Relic neutrinos originating from the decoupling early universe, also known as the cosmic neutrino background (CνB), may be abundant but are estimated to exhibit extremely low average energies of $\langle E_\nu \rangle \sim 5.28 \cdot 10^{-4}\,\mathrm{eV}$ [60] and their interactions with mat-
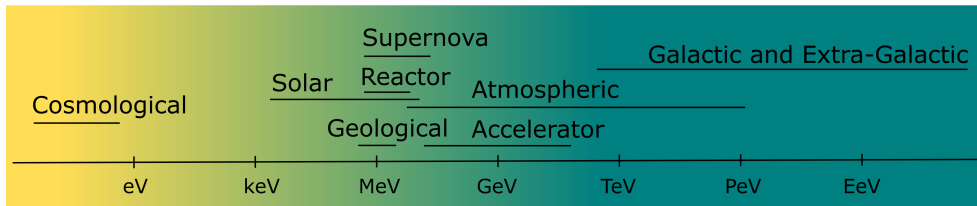
Figure 1.3: Illustration of different neutrino sources, displayed against neutrino energy. Black bars below the respective sources serve as a rough indication of the corresponding expected neutrino energy ranges. Cosmological neutrinos, known as the cosmic neutrino background, are at the low end of the energy spectrum, whereas galactic and extra-galactic neutrinos span the high-energy end of the spectrum.

ter are further characterised by exceptionally small cross-sections. On the other end of the energy scale, galactic and extra-galactic neutrino sources are able to produce neutrinos with energies exceeding 10^{18} eV, but offer only low fluxes, which are typically difficult to calculate, diffuse and uncertain. Further to this, the detection of ultra-high energy events usually requires large detector volumes to capture an event and operate with sensible expected event rates.

The detection method analysed in Chapter 2 is in its essence a momentum recoil detector. As mentioned, coherent interactions of neutrinos, such as the coherent neutral-current interaction of a neutrino with a nucleus, can loosely be observed when the absolute momentum $q \cdot r < 1$ of the mediator (Z^0) is smaller than the inverse radius of the scatterer [63]. This, in turn, restricts the energy of the scattering neutrinos to the low MeV sector since the transferred momentum needs to be appropriately small. Candidates like supernova, solar, reactor neutrinos or geological neutrinos with typical energies ranging from $10 \, \text{keV} - 20 \, \text{MeV}$ are therefore favourable for further consideration. Crucially, a detector's ability to sense neutrinos from either of these sources is the magnitude of the flux at the detector site. A comparison of the particle fluxes narrows the field of ideal neutrino sources for the purpose at hand. The expected fluxes at earth's surface for solar neutri-

nos [64] $\Phi_{solar} \sim 6.5 \cdot 10^{10}\,\mathrm{cm}^{-2}\mathrm{s}^{-1}$, geoneutrinos [65] $\Phi_{geo} \sim 10^6\,\mathrm{cm}^{-2}\mathrm{s}^{-1}$ and supernova neutrinos [66, 67] $\Phi_{supernova} \sim 10\,\mathrm{cm}^{-2}\mathrm{s}^{-1}$ (for diffuse supernovae) are comparably small with respect to the expected reactor neutrino fluxes $\Phi_{reactor} \sim 1.7 \cdot 10^{13}\,\mathrm{cm}^{-2}\mathrm{s}^{-1}$ derived in Chapter 2 for a detector placed at a distance of 20 m to the source. Reactor neutrinos have therefore been selected as the most suitable candidate for an initial estimation of the phase accumulation due to neutrino scattering off massive matter-wave interferometers.

1.11 Modern Neutrino Experiments

The large variety of neutrino energies necessitates the development of a multitude of highly specialised detector designs, of which a select few will be discussed in this section.

A popular large-scale detector facility is known as the IceCube Neutrino Observatory. It is a cubic-kilometer neutrino telescope featuring a surface layer and an in-ice detector consisting, among other components, of photo-multiplier-type detection modules. It functions like a Cherenkov detector, observing the Cherenkov radiation produced by charged particles resulting from neutrino interactions, and is well suited for the observation of neutrino events in the $E_\nu \sim \mathrm{GeV} - \mathrm{PeV}$ energy regime such as those associated with blazar flares and particle emissions of active galactic nuclei. Its DeepCore detection module has a neutrino energy threshold of 10 GeV [68], meaning that it is insensitive to neutrino events far below this energy threshold. Aside from its use in atmospheric neutrino oscillation studies, the IceCube detector measures high-energy event cross-sections and is used for the investigation of non-standard neutrino interactions.

Another long-standing Cherenkov detector of particular relevance to

neutrino physics is Super-Kamiokande, an ultra-pure water tank lined with photo-multiplier-tube detection modules located in the Kamikoa mine. Atmospheric neutrino data published in 1998 [69] describing a deficit of measured muon neutrinos contributed to the discovery of solar neutrino oscillations and resulted in the award of a Nobel prize in 1995, shared between physicists from Super-Kamiokande and the Sudbury Neutrino Observatory. The early Kamiokande detector also successfully observed neutrinos from the SN 1987A supernova explosion, which constitutes the only direct observation of such an event to date. At present, the lowest achieved neutrino energy threshold is on the order of $3.5\,\mathrm{MeV}$ for solar neutrino events. It is anticipated that a modification in the form of a gadolinium-doped variant of the ultra-pure water detector may capture signatures of reactor neutrinos originating from reactor facilities in its vicinity, with an expectation of around 400 events possibly being observed annually [70].

Likely closest in its comparably reduced total detector mass to the experiment proposed in Chapter 2 is the Nucleus experiment, an arrangement of gram-scale Sapphire and Calcium Tungstate cryogenic calorimeters totalling a detector mass of $10\,\mathrm{g}$. In contrast to measuring relative phases between components of a superposition, this detector captures phonons created due to nuclear recoil-induced lattice vibrations. It is expected to reach a recoil threshold on the order of $20\,\mathrm{eV}$, which would, in principle, allow for the high-precision measurements of low-energy coherent neutrino-nucleus interactions. It has recently demonstrated its sensitivity to nuclear recoils induced by neutron capture. The observed recoil peak at $112\,\mathrm{eV}$ appearing due to the capture interaction may in itself provide a useful method of calibration for future coherent-elastic neutrino-nucleus scattering (CEνNS) experiments [71].

A different recently proposed experiment in the realm of levitated optomechanical systems aims to detect heavy sterile neutrinos via the recoil of an optically levitated sensor [12] following nuclear β decay. According to theoretical estimates, radioisotopes embedded in a trapped nanosphere of $100\,\mathrm{nm}$ size, for which the momentum can be measured continuously, should be a viable platform for capturing momentum kicks resulting from decays to sterile neutrinos with masses greater than $100\,\mathrm{keV}$. Interestingly, the setup may be used to determine the absolute neutrino mass through full energy and momentum reconstruction of the recoiling sphere and emitted secondary particles, provided the necessary sensitivity can be reached. Similarly to the work presented in Chapter 2, the sensitivity could be lowered by events in which the recoiling nucleus leaves the nanosphere. In addition, the reconstruction of the energy of secondary emitted particles, such as electrons, may propagate and result in an erroneous estimate of the neutrino's momentum and mass. Nevertheless, the advantage of such an approach would be its comparably low sensor mass, enabling its realisation with existing experimental techniques. However, it should be stressed that the quantumness of the sensing object is not (yet) harnessed and that the method does not constitute a direct measurement of the neutrino.

Chapter 2

Neutrino Detection via Superpositions of Macroscopic Objects

Contents

We examine a macroscopic system in a quantum superposition of two spatially separated localized states as a detector for a stream of weakly interacting relativistic particles. We do this using the explicit example of neutrinos with MeV-*scale energy scattering from a solid object via neutral-current neutrino-nucleus scattering. Presuming the (anti-)neutrino source to be a nuclear fission reactor, we utilize the estimated flux and coherent elastic neutrino-nucleus cross section to constrain the spatial separation* Δx *and describe the temporal evolution of the sensing system. Particularly, we find that a potentially measurable relative phase between quantum superposed components is obtained for a single gram scale mass placed in a superposition of spatial components separated by* 10^{-14} m *under sufficient cooling and background suppression.*

In this chapter I elucidate the application of matter-wave interferometric sensors for the detection of low energy neutrinos, emitted by a nuclear reactor source. Through their scattering off a massive sensing particle in superposition, the momentum imparted due to the interaction results in the acquisition of a relative phase between the components of

the superposition. I discuss the requirements on the sensor and the conditions, i.e. the necessary suppression of the environment, under which such a phase can potentially be measured in an experiment.

2.1 The Context

Despite extensive scientific efforts, neutrinos still pose a puzzling enigma, decades after they were first observed experimentally [73]. While it may be known that neutrinos interact only through the weak and the gravitational forces, many of the questions on the very nature of these particles remain unanswered to this day. As all other fermions in the Standard Model, neutrinos were formerly assumed to be representable by Dirac spinors and additionally thought to be massless. However, oscillation experiments have shown that particles produced in a particular, well-defined flavour eigenstate can, after having travelled a sufficiently long distance, with a certain probability be detected in a different flavour state [69]. A consequence of these findings is that neutrinos do have mass and that their flavor eigenstates are different from their mass eigenstates, as stated in Chapter 1.7. As a result of being massive, neutrinos could be either Dirac or Majorana particles and it is currently unknown which of the two they are. Present day oscillation experiments enable measurements of mass squared differences of the three neutrino mass eigenstates, but they are not capable of measuring absolute neutrino masses, on which limits however do exist [74]. In addition, oscillation experiments have also seen hints for the existence of so-called sterile neutrinos. These neutrinos are not explicitly treated here, since they are hypothetical additional species of neutrinos that do not experience any of the Standard Model forces but would mix with the three standard neutrinos.

The vast multitude of unknowns provides a motivation to seek novel methods to detect neutrinos, especially to examine if the detector size
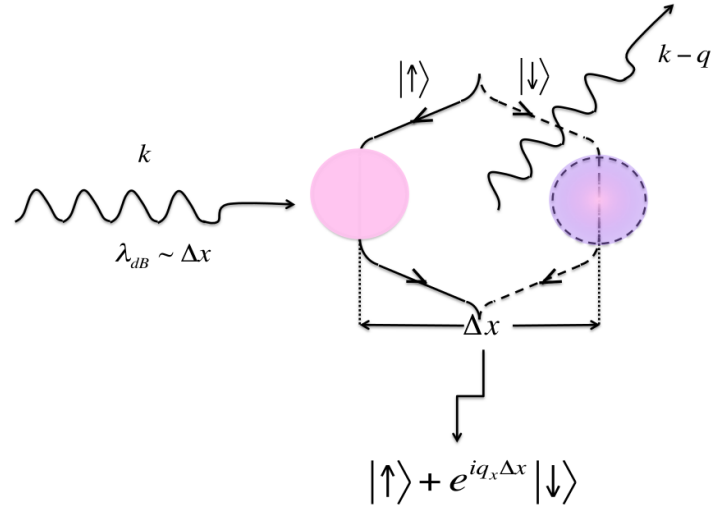
Figure 2.1: The working mechanism of a system detecting the momentum recoil of a crystal due to the scattering of a particle of initial momentum k from it through a relative phase between two components of a superposition. In a general Stern-Gerlach interferometer, the phase difference between two spatially separated components ends up as a phase difference between two spin states (indicated by $|\uparrow\rangle$ and $|\downarrow\rangle$) and can be measured as a phase difference between spin components. The separation Δx is assumed to be on the order of the incoming scatterer's de Broglie wavelength λ_{db}.

can be reduced. In this work, I will introduce one such approach aiming to study reactor anti-neutrinos with energies of a few MeV through their *momentum transfer* in scattering from a macroscopic system placed in a quantum superposition of distinct centre of mass positions, with the momentum transfer appearing as a relative phase between the components of the superposition.

The field of matter-wave interferometry in which a large mass, such as a solid object or crystal of several atoms, goes to a quantum superposition of being "here" and "there" is an emerging area still in development, with several nascent ideas. For an inexhaustive list see [38, 46, 47, 75–84]. These developments have so far been primarily steered by the aim to extend the boundaries of quantum mechanics *empirically* to larger objects, as the quantum behaviour of the centre of mass (COM) of sufficiently

macroscopic masses remains untested. Unlike in the case of interference experiments with several atoms from a cold source, for example a Bose-Einstein condensate, where each atom goes one way or another, here *all* atoms of the crystal go one way together or *all* atoms of the crystal go the other way together. On the experimental side these developments are stimulated, on the one hand, by the demonstration of quantum superpositions of the COM of large molecules consisting of up to ∼ 2000 atoms [44] and on the other hand, by the achievement of cooling of the COM of much larger masses such as 10^{-17} kg silica nanoparticles [85–88] and 10 kg masses [89] close to their quantum mechanical ground states. While this may still indicate a significant gap between what has been demonstrated, and what needs to be achieved in order to realise experiments with the COM of large masses in a superposition, there are the above well formulated schemes and conditions which could be adapted.

Quantum superpositions of the COM of large masses can have a great potential as a sensor [90]. It has already been theoretically demonstrated that they can measure tiny gravitational effects including the detection of low frequency gravitational waves [10], and, ultimately, even evidence the quantum nature of gravity [48, 49, 91, 92] or be able to test new forces [93] and the weak Equivalence principle in a quantum regime [94]. The decoherence of quantum superpositions may also be a sensitive detector for dark matter [13, 14, 51]. Once a quantum superposition of a large mass being in two positions is produced, external forces cause a relative phase shift between the two components of this superposition. Hence, I propose that it might also be possible to detect tiny momentum transfers due to the scattering of weakly interacting particles from such superpositions. In particular, recently the approach of detecting particles beyond the SM via the momentum recoil of levitated nano-objects in localized (classical) states has become topical [95–97]. It is natural thus to ask

whether quantum superpositions can aid further. I study this herewith using neutrinos as an example, importantly in a regime in which they scatter coherently from entire nuclei as that significantly enhances the cross section.

Predicted more than 40 years ago in 1974 [98] and recently observed experimentally [99], coherent elastic scattering of neutrinos from nuclei (CEνNS) is the dominant scattering channel for incoming neutrino energies $E_\nu \ll 100$ MeV. The scattering coherence manifests in an enhancement of the cross-section, which scales with N^2, with N being the number of neutrons in the nucleus. Up until recently, it has however been of great difficulty to detect such neutral current events, in part due to the large detector volumes (enough nuclei) and low energy thresholds required to detect the keV to sub-keV recoils of the nuclei.

In light of the advent of proposals for small-scale neutrino detectors [100, 101] that aim to exploit the small recoil energies and relatively large CEνNS cross section associated with scattering events in the (sub-)MeV neutrino energy regime, I consider the suitability of matter-wave interferometric schemes for detecting such processes. I emphasise that in contrast to classical methods, this approach is based on the detection of neutrinos via massive quantum devices and hence exploits features which are inherently quantum.

2.2   Detecting Particulate Matter by Measuring a Phase

The essence of the type of detector that I am considering here is given in Fig.2.1. A mass is prepared in a quantum superposition of spatially

distinct states and, in line with most particle physics literature, natural units have been assumed in detoting the phase contribution. An ideal way to generate such a spatial superposition is by employing a Stern-Gerlach type interferometric scheme with a single spin embedded in a mass. An archetypal example is the Nitrogen-Vacancy (NV) point defect in a diamond crystal, which carries a spin-1 (made of two electrons) [102]. However, any other point defect with an electronic spin in any other crystal [103] or a single dopant atom with an unpaired electronic spin implanted in a solid, as for example, used in certain designs of solid state quantum computers [104] will serve the purpose. It is understood that the atom carrying this spin is tightly bound to the rest of the crystal. It also has to be ensured that there is this single spin which can couple to external magnetic fields strongly (i.e. with the strength of a Bohr magneton) while there may be unpaired nuclear spins on various atoms in the crystal which couple with the much lower strength of a nuclear magneton. While detailed studies can be found in Refs.[38, 39, 47, 80–84], here I present only a schematic description. The spin is initially prepared in a quantum superposition $\frac{1}{\sqrt{2}}(|\uparrow\rangle_s + |\downarrow\rangle_s)$ and the mass bearing the spin is subjected to an inhomogeneous magnetic field. This couples its spin and motional degrees of freedom: for $|\uparrow\rangle_s$ spin state, the mass accelerates to the left, and for the $|\downarrow\rangle_s$ spin state, the mass accelerates to the right. They can be brought to a halt at a given superposition size Δx by flipping the spins at appropriate times. The resulting entangled state between spin and centre of mass degree of freedom of the mass generated is

$$|\Psi_0\rangle_S = \frac{1}{\sqrt{2}}\Big(|\uparrow\rangle_s|\bar{x}_0\rangle_C + |\downarrow\rangle_s|\bar{x}_1\rangle_C\Big), \qquad (2.2.1)$$

where $|\bar{x}_0\rangle_C$ and $|\bar{x}_1\rangle_C$ respectively refer to both parts of the superposition, each one describing the center-of-mass motion of the test mass (crystal), while the subscript S denotes the combined system of spin and

crystal. The states $|\bar{x}_j\rangle$ are to be understood as Gaussian wavepackets localized around the position $(\bar{x}_j, 0, 0)$, and momentum $p \approx 0$. The superposition size is $\Delta x = \bar{x}_1 - \bar{x}_0$. For simple notation, I treat the macroscopic mass as a single particle and write the COM state of the macroscopic mass as

$$|\bar{x}_j\rangle_C = \left(\frac{1}{\sigma_c\sqrt{2\pi}}\right)^{\frac{1}{2}} \int_{-\infty}^{\infty} dx \ e^{-\frac{(x-\bar{x}_j)^2}{2\sigma_c^2}} \Psi_C^\dagger(x)|0\rangle, \qquad (2.2.2)$$

where $\Psi_C^\dagger(x)$ creates the whole crystal at position $(x, 0, 0)$ and $|0\rangle$ is the vacuum state. Fundamentally, $|\bar{x}_j\rangle$ is a many-particle state. Hence $\Psi^\dagger(x)_C$ is equal to a product of proton, neutron and electron creation operators at positions locked to, and distributed around, the COM position $(x, 0, 0)$.

I will now illustrate what happens to the above Gaussian state $|\bar{x}_j\rangle$ when a momentum $\boldsymbol{q}$ is transferred to it. To model this, I assume momentum creation and annihilation operators of the mass to be $b_{\boldsymbol{k}}^\dagger$ and $b_{\boldsymbol{k}}$ respectively, and study the action on the state

$$\left(\int d^3\boldsymbol{k} \ b_{\boldsymbol{k}+\boldsymbol{q}}^\dagger b_{\boldsymbol{k}}\right) \int_{-\infty}^{\infty} dx \ e^{-\frac{(x-\bar{x}_j)^2}{2\sigma_c^2}} \Psi^\dagger(x)|0\rangle$$

$$\propto \int_{-\infty}^{\infty} dx \ e^{-\frac{(x-\bar{x}_j)^2}{2\sigma_c^2}} \int d^3\boldsymbol{k} \ b_{\boldsymbol{k}+\boldsymbol{q}}^\dagger b_{\boldsymbol{k}} \int d^3\boldsymbol{k}' e^{ik_x'x} b_{\boldsymbol{k}'}^\dagger |0\rangle$$

$$= \int_{-\infty}^{\infty} dx \ e^{-\frac{(x-\bar{x}_j)^2}{2\sigma_c^2}} e^{-iq_x x} \int d^3(\boldsymbol{k}+\boldsymbol{q}) \ e^{i(k_x+q_x)x} b_{\boldsymbol{k}+\boldsymbol{q}}^\dagger |0\rangle$$

$$= \int_{-\infty}^{\infty} dx \ e^{-\frac{(x-\bar{x}_j)^2}{2\sigma_c^2}} e^{-iq_x x} \Psi^\dagger(x)|0\rangle$$

$$= e^{-iq_x\bar{x}_j} e^{-\frac{q_x^2\sigma_c^2}{2}} \int_{-\infty}^{\infty} dx \ e^{-\frac{(x-\bar{x}_j+iq_x\sigma_c^2)^2}{2\sigma_c^2}} \Psi^\dagger(x)|0\rangle. \qquad (2.2.3)$$

Considering the special case when the width of the Gaussian wavepacket is much smaller than the length scale of the transferred momentum $\sigma_c \lesssim$

$1/q_x$, the state of the Gaussian after the momentum transfer is

$$e^{-iq_x \bar{x}_j} \int_{-\infty}^{\infty} dx \ e^{-\frac{(x-\bar{x}_j)^2}{2\sigma_c^2}} \Psi^\dagger(x)|0\rangle = e^{-iq_x \bar{x}_j}|\bar{x}_j\rangle, \qquad (2.2.4)$$

implying that the initial state of a superposed mass and a scattering particle evolves as

$$|\Psi_0\rangle_S |\boldsymbol{p}\rangle_B \to |\Psi_{q_x}\rangle_S |\boldsymbol{p} - \boldsymbol{q}\rangle_B, \qquad (2.2.5)$$

where I have introduced the label B to denote the bath environment comprised of the scattering particle(s) and the subscript S to refer to the superposed target mass. The state $|\Psi_{q_x}\rangle_S$ is given by

$$|\Psi_{q_x}\rangle_S = \frac{1}{\sqrt{2}} \Big(|\uparrow\rangle |\bar{x}_0\rangle + e^{-iq_x \Delta x} |\downarrow\rangle |\bar{x}_1\rangle \Big), \qquad (2.2.6)$$

where the difference in center-of-mass position is $\Delta x = \bar{x}_1 - \bar{x}_0$. A particle scattering from the above state and transferring a momentum $\boldsymbol{q}$ to it, could be detected as a phase difference of $\frac{q_x \Delta x}{\hbar}$ (restoring the $\hbar$) between the components of the superposition, where q_x is the x-component of the momentum transfer. While a transfer of momentum with negligible transverse contributions represents an idealised scenario, it should be implicitly clear that in a more general scenario, I would have to consider the three-dimensional nature of the problem. In a typical Stern-Gerlach interferometry experiment, the two components $|\bar{x}_0\rangle$ and $|\bar{x}_1\rangle$ are brought back to completely overlap with each other by reversing the process which created them, as shown in Fig. 2.1 so that the spin state becomes $|\psi_{q_x}\rangle_s = \frac{1}{\sqrt{2}} \Big(|\uparrow\rangle_s + e^{-iq_x \Delta x} |\downarrow\rangle_s \Big)$. Thus the phase is measurable purely from the off-diagonal component $\langle\uparrow |\rho_s| \downarrow\rangle$ of the density matrix $\rho_s = |\psi_{q_x}\rangle\langle\psi_{q_x}|_s$ of the spin. In general, the scattering neutrinos will scatter with a distribution of momenta, so that there will be a mixed state density matrix, while the process itself will lead to a decoherence as well. I will therefore treat the evolution in terms of open quantum

systems techniques, deriving a master equation to be followed by the density matrix.

2.3 Coherent Elastic Neutrino-Nucleus Scattering Cross Section

In this section, I discuss the CEνNS cross section in the regime of reactor anti-neutrinos, since the calculation of the matrix element is directly related to the interaction Hamiltonian. For this purpose, I outline the description of coherent elastic scattering of a neutrino with incident four momentum $p_i = (E_\nu, \mathbf{p}_i)$ by a nucleus of mass m_{nucl} and incident four momentum $k_i = (m_{\mathrm{nucl}}, 0)$, restricting ourselves to the dominant neutral current CEνNS processes for the reason of simplicity. An illustration of the process is depicted in Fig. 2.2, where I have assumed the comparably heavy nucleus to be at rest and the final momenta to be of the form $p_f = (E_{\nu,f}, \mathbf{p}_f)$ and $k_f = (E_{n,f}, \mathbf{k}_f)$.
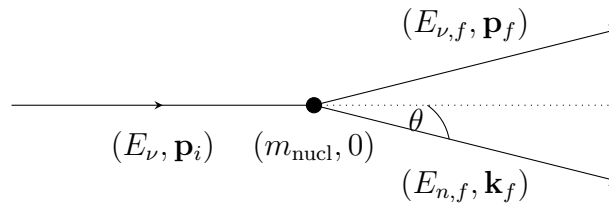
Figure 2.2: Elastic scattering illustration with the scattering angle denoted as θ, the initial momenta p_i, k_i and the final momenta p_f, k_f.

The incoming and outgoing four momenta can be reformulated in terms of the incoming neutrino energy E_ν, the kinetic energy transferred due to scattering T and the nucleus mass m_{nucl}

$$p_i = (E_\nu, \mathbf{p}_i), \tag{2.3.1}$$

$$k_i = (m_{\mathrm{nucl}}, 0), \tag{2.3.2}$$

$$p_f = (E_\nu - T, \mathbf{p}_f), \tag{2.3.3}$$

$$k_f = (m_{\mathrm{nucl}} + T, \mathbf{k}_f). \tag{2.3.4}$$

The tree-level Feynman diagram representing such a process is shown in Fig. 2.3. In order to recover the cross section, the standard approach
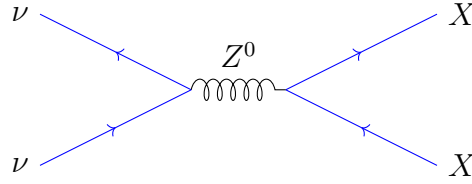
Figure 2.3: Feynman diagram for neutral current coherent elastic ν-nucleus scattering, where time runs vertically. The label ν refers to the neutrino whereas the symbol X represents the nucleus.

is to determine the scattering amplitude $\mathcal{M}_{ss'}$ using the neutral current interaction Lagrangian

$$\mathcal{L} = \frac{G_F}{\sqrt{2}} J^\mu_\nu J_{\mu,\text{nucl}}, \tag{2.3.5}$$

where the Fermi constant G_F is given in Table 2.1, and the relevant Feynman rules [105]. The quantities described by J^μ_ν and $J_{\mu,\text{nucl}}$ denote the neutral currents of neutrino and nucleus. Neutral fermionic currents are given by

$$J^\mu_f = \sum_i \overline{\psi}_{f_i} \gamma^\mu (g_V^{f_i} - g_A^{f_i} \gamma^5) \psi_{f_i} \tag{2.3.6}$$

where ψ_f denote the respective fermionic fields. Omitting the sum and inserting its couplings $g_V^\nu = 1/2$ and $g_A^\nu = 1/2$, the neutrino neutral current is

$$J^\mu_\nu = \overline{\psi}_\nu \gamma^\mu \frac{1}{2} (1 - \gamma^5) \psi_\nu. \tag{2.3.7}$$

It is a general feature of the weak interaction that its exchange bosons couple only to left-handed neutrinos or right-handed anti-neutrinos. For the nucleus neutral current, I choose a description in terms of its weak

coupling constant and the four-momenta k_i, k_f,

$$J_{\mu,nucl} = \frac{Q_W}{2} F(q^2)(k_i + k_f)_\mu, \qquad (2.3.8)$$

where Q_W refers to the weak charge and $F(q)$ to the form factor dependent on the exchanged momentum q. Equation (2.3.5) can now be used to recover the Feynman amplitude $\mathcal{M}$, which is then formulated as follows

$$i\mathcal{M}_{ss'} = -i\frac{G_F Q_W F(q^2) g_L^\nu}{\sqrt{2}}$$
$$\times \bar{u}^{s'}(p_f)\gamma^\mu(1-\gamma^5)u^s(p_i)(k_i + k_f)_\mu. \qquad (2.3.9)$$

In the laboratory frame, the differential cross section with respect to the transferred kinetic energy is related to the absolute square of the matrix element as $\frac{d\sigma}{dT} = \frac{\sum_{ss'}|i\mathcal{M}_{ss'}|^2}{32\pi m_{nucl}E_\nu}$ and hence given by [106]

$$\frac{d\sigma}{dT} = \frac{G_F^2 Q_W^2 |F(q^2)|^2 m_{nucl}}{4\pi}\left(1 - \frac{T}{E_\nu} - \frac{m_{nucl}T}{2E_\nu^2}\right). \qquad (2.3.10)$$

The differential cross section for the scattering of anti-neutrinos is derived analogously. Following the expression of the differential cross-section with respect to the solid angle Ω as given in [107], $\frac{d\sigma}{d\Omega} = \frac{G_F^2 Q_W^2 E_\nu (1+\cos\theta)|F(q^2)|^2}{16\pi^2}$, it becomes evident that the emitted neutrinos scatter mostly in the forward direction. Assuming a scattering angle θ between the initial neutrino and final nucleus momenta, the amount of kinetic energy T transferred to the nucleus can be expressed as follows

$$T = \frac{2m_{nucl}E_\nu^2 \cos^2\theta}{(m_{nucl} + E_\nu)^2 - E_\nu^2 \cos^2\theta}. \qquad (2.3.11)$$

The maximum kinetic energy transfer is then obtained for $\theta=0$. The coherent elastic neutrino-nucleus cross section can be recovered from Eq. (2.3.10), following integration over kinetic energy. In all further calculations, I have approximated the form factor as $F(q) \sim 1$. This

is appropriate solely for the energy range considered, since interactions involving higher neutrino-energies and therefore higher momentum transfers may be able to resolve the nucleus and eventually result in a suppression and flattening of the coherent cross-section. It should be noted that the cross section increases not only with neutrino energy, but also with increasing number of neutrons N in the target nucleus, which will impact the choice of detector material best suited for neutrino sensing. The latter dependency becomes evident through a closer inspection of the weak charge

$$Q_W = ((1 - 4\sin^2\theta_W)Z - N). \qquad (2.3.12)$$

For the purpose of a real-world experiment, this means that the target material does play an important role in the ability to detect any scattering phase effect from neutrino scattering on nuclei.

2.4　Quantum Open Systems and the Born-Markov Approximation

I consider the scenario of a heavy nucleus in the presence of a (fermionic) bath of neutrinos scattering from it. Since in an experiment, one typically has no control over a specific scattered neutrino, but I nonetheless wish to describe the evolution of a comparably heavy nucleus, I resort to an open quantum systems approach. Following the description in [108], the total Hamiltonian of a weakly interacting system and bath is

$$H = H_S + H_B + H_{SB} \qquad (2.4.1)$$

where H_{SB} refers to the interaction between S and B. In order to derive the master equation of the system, it is of convenience to write the

interaction Hamiltonian as

$$H_{SB} = \sum_\alpha S_\alpha B_\alpha \qquad (2.4.2)$$

with S_α and B_α denoting the system and bath operators. I will hence have to map the respective parts of the non-standard interaction Hamiltonian for coherent elastic neutrino-nucleus scattering onto system and bath operators. The summation will become an integral over all relevant external three momenta. It shall also be noted that I impose hermiticity on H_{SB}. Taking the bath correlation time to be much shorter than the timescale over which the system evolves, I resort to a description in the Born-Markov approximation. Born-Markov master equations are based on two assumptions, namely

1. the Born approximation, which assumes weak coupling between the system and the environment, such that the change in the density matrix of the environment is negligibly small and the combined quantum state remains an approximate product state during time evolution

$$\rho_{tot}(t) \sim \rho_S(t) \otimes \rho_B \qquad (2.4.3)$$

2. the Markov approximation, which assumes memory effects of the environment to be negligible, meaning that the quantum evolution of the environment state depends only on its present, but not on its past. Compared to the characteristic timescale over which the system evolves, the bath correlation function decays fast.

The master equation for the system in this approximation is governed by

$$\frac{d\rho_S}{dt} = -\frac{i}{\hbar}[H_S, \rho_S] - \left\{ \int_0^\infty d\tau \sum_{\alpha\beta} C_{\alpha\beta}(-\tau) \right.$$
$$\left. \times [S_\alpha S_\beta(-\tau)\rho_S - S_\beta(-\tau)\rho_S S_\alpha] + \text{H.c.} \right\}, \tag{2.4.4}$$

where

$$C_{\alpha\beta} = \frac{1}{\hbar^2} Tr[\rho_B B_\alpha B_\beta(-\tau)] \tag{2.4.5}$$

is the bath correlation function, which contains all the relevant properties of the environment, and the time dependence of the operators S_β and B_β is determined by

$$S_\beta(-\tau) = e^{-\frac{iH_S\tau}{\hbar}} S_\beta e^{\frac{iH_S\tau}{\hbar}}, \tag{2.4.6}$$

$$B_\beta(-\tau) = e^{-\frac{iH_B\tau}{\hbar}} B_\beta e^{\frac{iH_B\tau}{\hbar}}. \tag{2.4.7}$$

As I work in natural units, I set $\hbar = c = 1$ for now.

2.4.1   Quantum Master Equation for Neutrino-Nucleus Scattering

The Lagrangian density [109] for the interaction of neutrino ν and nucleus n is is given by Eq. (2.3.5). Hence, the interaction Hamiltonian $H_{n,\nu}$ corresponds to

$$H_{n,\nu} = -\int d^3x \mathcal{L}(x)$$
$$= -\frac{G_F}{\sqrt{2}} \int d^3x J_\nu^\mu(x) J_{\mu,\text{nucl}}(x) = H_{SB}. \tag{2.4.8}$$

Choosing to rewrite the neutrino current in second quantised form, I observe that

$$
\begin{aligned}
J_\nu^\mu(x) &= \overline{\psi}_\nu(x)\frac{1}{2}\gamma^\mu(1-\gamma^5)\psi_\nu(x) \\
&= \int \frac{d^3p_i d^3p_f}{(2\pi)^6\sqrt{4E_{p_i}E_{p_f}}}a_{p_f}^\dagger a_{p_i}e^{-i(p_i-p_f)x} \\
&\quad \times \overline{u}^{s'}(p_f)\frac{1}{2}\gamma^\mu(1-\gamma^5)u^s(p_i),
\end{aligned}
\tag{2.4.9}
$$

so that the Hamiltonian is

$$
\begin{aligned}
H_{n,\nu} &= -\frac{G_F Q_W F(q)}{2\sqrt{2}}\int d^3x \times \frac{d^3p_i d^3p_f d^3k_i d^3k_f}{(2\pi)^{12}\sqrt{16E_{p_i}E_{p_f}E_{k_i}E_{k_f}}} \\
&\quad \times e^{-i(k_i+p_i-k_f-p_f)x}a_{p_f}^\dagger a_{p_i} \\
&\quad \times \overline{u}^{s'}(p_f)\gamma^\mu(1-\gamma^5)u^s(p_i)c_{k_f}^\dagger c_{k_i}(k_f+k_i)_\mu.
\end{aligned}
\tag{2.4.10}
$$

Note that although here I have generically used k_i, k_f to label 3-momenta, $(k_f + k_i)_\mu$ stand for 4-momenta. Noting that the only x-dependence is now in the exponential, I can perform the spatial integration. Further to this, the factor $F(q) \sim 1$ in this scenario and can therefore be neglected,

$$
\begin{aligned}
H_{n,\nu} &= -\frac{(2\pi)^3 G_F Q_W}{2\sqrt{2}}\int \frac{d^3p_i d^3p_f d^3k_i d^3k_f}{(2\pi)^{12}\sqrt{16E_{p_i}E_{p_f}E_{k_i}E_{k_f}}} \\
&\quad \times \delta^3(k_i+p_i-k_f-p_f)a_{p_f}^\dagger a_{p_i} \\
&\quad \times \overline{u}^{s'}(p_f)\gamma^\mu(1-\gamma^5)u^s(p_i)c_{k_f}^\dagger c_{k_i}(k_f+k_i)_\mu \\
&= -\frac{(2\pi)^3 G_F Q_W}{2\sqrt{2}}\int \frac{d^3p_i d^3p_f d^3k_i d^3k_f}{(2\pi)^{12}16E_{p_i}E_{p_f}E_{k_i}E_{k_f}} \\
&\quad \times \overline{u}^{s'}(p_f)\gamma^\mu(1-\gamma^5)u^s(p_i)(k_f+k_i)_\mu \\
&\quad \times \delta^3(k_i+p_i-k_f-p_f)|p_f\rangle\langle p_i| \otimes |k_f\rangle\langle k_i|,
\end{aligned}
\tag{2.4.11}
$$

with one-particle states $|p,s\rangle = \sqrt{2E_p}a_p^{s\dagger}|0\rangle$. In Eq. (2.4.11), I have treated the nucleus and neutrino as single particles and applied a mapping to suitable momentum-basis states. Using the matrix element for the neutrino-nucleus scattering $\mathcal{M}_{p_i,k_i,p_f,k_f} = -\frac{G_F Q_W}{2\sqrt{2}}\overline{u}^{s'}(p_f)\gamma^\mu(1-\gamma^5)u^s(p_i)(k_f+k_i)_\mu$ and by computing the integral over the final nucleus momentum k_f

I obtain

$$
\hat{H}_{n,\nu} = \int \frac{d^3 p_i d^3 p_f d^3 k_i d^3 k_f}{(2\pi)^9 2E_{p_i} 2E_{p_f} 2E_{k_i} 2E_{k_f}} \mathcal{M}_{p_i,k_i,p_f,k_f}
$$

$$
\delta^3(k_i + p_i - k_f - p_f) |p_f\rangle\langle p_i| \otimes |k_f\rangle\langle k_i|
$$

$$
= \int \frac{d^3 p_i d^3 p_f d^3 k_i \mathcal{M}_{p_i,k_i,p_f,k_i+p_i-p_f}}{(2\pi)^9 2E_{p_i} 2E_{p_f} 2E_{k_i} 2E_{k_i+p_i-p_f}}
$$

$$
|p_f\rangle\langle p_i| \otimes |k_i + p_i - p_f\rangle\langle k_i| \tag{2.4.12}
$$

$$
= \int \frac{d^3 p_i d^3 p_f d^3 k_i \mathcal{M}_{p_i,k_i,p_f,k_i+p_i-p_f}}{(2\pi)^9 2E_{p_i} 2E_{p_f} 2E_{k_i} 2E_{k_i+p_i-p_f}}
$$

$$
|p_f\rangle\langle p_i| \otimes e^{i(p_i-p_f)\hat{x}} |k_i\rangle\langle k_i|
$$

where I have used the fact that the momentum state $|k_i + p_i - p_f\rangle$ can be rewritten in a suitable manner. Now I make a crucial simplifying approximation: I assume the nucleus mass to be sufficiently large compared to its momenta $m_{\text{nucl}} \gg |k|$. Being inside the crystal which is stationary, I treat the nucleus as being effectively at rest so that the expression of the matrix element implies $\mathcal{M}_{p_i,k_i,p_f,k_f} \sim \mathcal{M}_{p_i,0,p_f,0}$. It is useful to write the nucleus integrals explicitly, so that $d\mu_\nu$ now only comprises the neutrino momentum integrals.

$$
\hat{H}_{n,\nu} = \int d\mu_\nu \int d^3 k_i \frac{\mathcal{M}_{p_i,0,p_f,0}}{(2\pi)^3 (2E_{k_i} 2E_{k_i+p_i-p_f})}
$$

$$
\times |p_f\rangle\langle p_i| \otimes e^{i(p_i-p_f)\hat{x}} |k_i\rangle\langle k_i| \tag{2.4.13}
$$

For a very heavy nucleus, I further assume that I can approximate the quantity $2E_{k_i} 2E_{k_i+p_i-p_f} \sim 4m_{\text{nucl}} E_{k_i}$. Seeing as the difference in the neutrino momenta is small and the energy of the nucleus is predominantly dependent on its heavy mass, I take this to be a reasonable justification for the model at hand. As a consequence, I observe that the Hamiltonian reduces further, for I am now able to use the definition for the one-particle state identity resolution.

$$
\hat{H}_{n,\nu} = \int d\mu_\nu \frac{\mathcal{M}_{p_i,p_f}}{2m_{\text{nucl}}} |p_f\rangle\langle p_i| \otimes e^{i(p_i-p_f)\hat{x}} \mathbb{I} \tag{2.4.14}
$$

Next, I associate the operators of the bath with the integrals over the amplitudes, whereas the rest of the above Hamiltonian is kept in the system operators. In the case at hand, I identify

$$S_\alpha = \frac{1}{2m_{\text{nucl}}} e^{i(p_i - p_f)\hat{x}} \mathbb{I}, \quad B_\alpha = \mathcal{M}_{p_i, p_f} |p_f\rangle \langle p_i|, \tag{2.4.15}$$

and I pack all dependencies on the Feynman amplitudes into the bath operators. Further, I argue that the COM of the crystal (to which the nucleus belongs) is trapped in a very low frequency trap, so that the time evolution of the operator S_β can be neglected. In order to time evolve the neutrino state, I assume the neutrino rest mass to be negligible with respect to its total energy. I further neglect flavor oscillations, which is a reasonable assumption over the short distances of $d \sim 20$ m I consider, so that the neutrino bath has the free Hamiltonian

$$H_B = \int \frac{d^3 p}{(2\pi)^3} E_p a_p^\dagger a_p. \tag{2.4.16}$$

At first I will consider a single neutrino scattering from the nucleus, thus I need to find the bath correlation function for a single neutrino bath. In order to do that, I need to use an incoming neutrino in a sufficiently momentum localized state $|\psi\rangle$ normalised to $\langle \psi | \psi \rangle = 1$. This is achieved by starting with a generic Gaussian initial momentum state

$$\begin{aligned}
|\psi\rangle &= \int \frac{d^3 p}{(2\pi)^3 \sqrt{2E_p}} \psi(p) |p\rangle \\
&= \int \frac{d^3 p}{(2\pi)^3 \sqrt{2E_p}} \frac{(2\pi)^{3/2}}{(2\pi\sigma^2)^{3/4}} e^{-\frac{(p-p_0)^2}{4\sigma^2}} |p\rangle.
\end{aligned} \tag{2.4.17}$$

I substitute $\tilde{\sigma} = \sqrt{2}\sigma$, such that the state is properly normalised to $\langle\psi|\psi\rangle = 1$ and regard it in the limit of a very narrow wavefunction.

$$\lim_{\tilde{\sigma}\to 0}|\psi\rangle = \lim_{\tilde{\sigma}\to 0}\int \frac{d^3p \, (4\pi\tilde{\sigma}^2)^{3/4} e^{-\frac{(p-p_0)^2}{2\tilde{\sigma}^2}}}{(2\pi)^{3/2}\sqrt{2E_p}(2\pi\tilde{\sigma}^2)^{3/2}}|p\rangle$$

$$= \epsilon\int \frac{d^3p}{\sqrt{2E_p}}(\tilde{\sigma})^{3/2}\delta^3(p-p_0)|p\rangle \qquad (2.4.18)$$

$$= \frac{\epsilon\tilde{\sigma}^{3/2}}{\sqrt{2E_{p_0}}}|p_0\rangle$$

Here, ϵ represents the collected numerical factors. I will use this simplified form in the last step above for subsequent computations. Thus,

$$C_{\alpha,\beta} = Tr[\rho_\nu B_\alpha B_\beta(-\tau)]$$

$$= Tr[|\psi\rangle\langle\psi|\mathcal{M}_{p_i,p_f}\mathcal{M}^*_{p'_f,p'_i}e^{-i(E_{p'_i}-E_{p'_f})\tau}|p_f\rangle\langle p_i|p'_f\rangle\langle p'_i|]$$

$$= (2\pi)^3\mathcal{M}_{p_i,p_f}\mathcal{M}^*_{p'_f,p'_i}2E_{p_i}\delta^3(p_i-p'_f)$$

$$\times \langle\psi|\psi\rangle\langle\psi|e^{-i(E_{p'_i}-E_{p'_f})\tau}|p_f\rangle\langle p'_i|\psi\rangle \qquad (2.4.19)$$

$$= (2\pi)^3\mathcal{M}_{p_i,p_f}\mathcal{M}^*_{p'_f,p'_i}2E_{p_i}\delta^3(p_i-p'_f)$$

$$\times \langle\psi|e^{-i(E_{p'_i}-E_{p'_f})\tau}|p_f\rangle\langle p'_i|\psi\rangle$$

$$= (2\pi)^9\epsilon^2\tilde{\sigma}^3\mathcal{M}_{p_i,p_f}\mathcal{M}^*_{p'_f,p'_i}2E_{p_i}\delta^3(p_i-p'_f)$$

$$\times e^{-i(E_{p'_i}-E_{p'_f})\tau}2E_{p'_i}\delta^3(p_0-p_f)\delta^3(p'_i-p_0).$$

In tracing over the neutrino's degrees of freedom, I have obtained the bath correlation function $C_{\alpha,\beta}$ as a function of the relevant neutrino momenta, with α and β respectively labelling the dashed and undashed momenta. I then proceed to insert the expression into the general formula for the master equation. For $d\rho_S/dt$ this results in the second term of Eq. (2.4.4)

given by

$$
\begin{aligned}
\frac{d\rho_S}{dt} = & -\frac{\epsilon^2\tilde{\sigma}^3}{4m_{\text{nucl}}^2}\int d\tau \int \frac{d^3p_i d^3p_f d^3p_i' d^3p_f'}{(2\pi)^3 16 E_{p_i}E_{p_f}E_{p_i'}E_{p_f'}} \\
& \times 4E_{p_i}E_{p_i'}\mathcal{M}_{p_i,p_f}\mathcal{M}_{p_f',p_i'}^*\delta^3(p_i - p_f') \\
& \times e^{-i(E_{p_i'}-E_{p_f'})\tau}\delta^3(p_0 - p_f)\delta^3(p_i' - p_0) \\
& \times \{-e^{i(p_i'-p_f')\hat{x}}\rho_S e^{i(p_i-p_f)\hat{x}} + e^{i(p_i-p_f)\hat{x}}e^{i(p_i'-p_f')\hat{x}}\rho_S + \text{H.c.}\} \\
= & -\frac{\epsilon^2\tilde{\sigma}^3}{4m_{\text{nucl}}^2}\int d\tau \int \frac{d^3p_f d^3p_i' d^3p_f'}{(2\pi)^3 4E_{p_f}E_{p_f'}} \times \mathcal{M}_{p_f',p_f}\mathcal{M}_{p_f',p_i'}^* \qquad (2.4.20) \\
& \times e^{-i(E_{p_i'}-E_{p_f'})\tau}\delta^3(p_0 - p_f)\delta^3(p_i' - p_0) \\
& \times \{-e^{i(p_i'-p_f')\hat{x}}\rho_S e^{i(p_f'-p_f)\hat{x}} + e^{i(p_f'-p_f)\hat{x}}e^{i(p_i'-p_f')\hat{x}}\rho_S + \text{H.c.}\} \\
= & -\frac{\epsilon^2\tilde{\sigma}^3}{8m_{\text{nucl}}^2 E_{p_0}}\int d\tau \frac{d^3p_f'}{(2\pi)^3 2E_{p_f'}}|\mathcal{M}_{p_0,p_f'}|^2 e^{-i(E_{p_0}-E_{p_f'})\tau} \\
& \times \{-e^{i(p_0-p_f')\hat{x}}\rho_S e^{i(p_f'-p_0)\hat{x}} + e^{i(p_f'-p_0)\hat{x}}e^{i(p_0-p_f')\hat{x}}\rho_S + \text{H.c.}\}.
\end{aligned}
$$

Lastly, I obtain

$$
\begin{aligned}
\frac{d\rho_S}{dt} = & -\frac{\epsilon^2\tilde{\sigma}^3}{64\pi^2 m_{\text{nucl}}^2 E_{p_0}}\int \frac{d^3p_f'}{E_{p_f'}}|\mathcal{M}_{p_0,p_f'}|^2 \\
& \times \delta(E_{p_0} - E_{p_f'})\{-e^{i(p_0-p_f')\hat{x}}\rho_S e^{i(p_f'-p_0)\hat{x}} \qquad (2.4.21) \\
& + e^{i(p_f'-p_0)\hat{x}}e^{i(p_0-p_f')\hat{x}}\rho_S + \text{c.c.}\}.
\end{aligned}
$$

It is always possible to find a suitable parameterisation of the momenta p_0 and p_f' in terms of an energy and appropriate angles. Therefore $\mathcal{M}_{p_0,p_f'} = \mathcal{M}(E_{p_f'},\Omega) \equiv \mathcal{M}(\Omega)$. Setting $\alpha = \frac{\epsilon^2\tilde{\sigma}^3}{64\pi^2 m_{\text{nucl}}^2}$ for brevity, I am able to write the factor before the curly brackets as

$$
\begin{aligned}
\Gamma = & -\alpha \int \frac{E_{p_f'}^2 dE_{p_f}' d\Omega}{E_{p_0}E_{p_f'}}|\mathcal{M}(E_{p_f'},\Omega)|^2\delta(E_{p_0} - E_{p_f'}) \\
= & -\frac{\epsilon^2\tilde{\sigma}^3}{64\pi^2 m_{\text{nucl}}^2}\int d\Omega |\mathcal{M}(\Omega)|^2.
\end{aligned} \qquad (2.4.22)
$$

It shall be noted that the factor $\epsilon^2\tilde{\sigma}_p^3 = 2^{-\frac{3}{2}}(2\pi\tilde{\sigma}_x^2)^{-\frac{3}{2}} = (2\pi\sigma_x^2)^{-\frac{3}{2}} = V_x^{-1}$ is essentially the volume of a Gaussian times a factor. Seeing as the spread $\sigma_x = (\int x^2|\psi(x)|^2 dx)^{1/2}$ for a conventionally normalised $\psi(x)$, the

normalised Gaussian in position space yields the recovered prefactor. The prefactor can be interpreted as the expectation value of finding a particle within the volume element V_x, which implies that the number of particles per unit volume $n = 1/V_x$. The neutrino's velocity $|p_\nu|/E_\nu \sim c = 1$. Hence, its flux is given by

$$F = nc = n, \tag{2.4.23}$$

where n is the number of particles per unit volume. I have normalized the single neutrino wavefunction to 1 particle per unit volume. Thus I have, in terms of the flux of 1 particle, F_1, the evolution of the reduced density matrix of the nucleus as given by

$$\frac{d\rho_S}{dt} = -\frac{F_1}{64\pi^2 m_{\text{nucl}}^2} \int d\Omega |\mathcal{M}(\Omega)|^2$$
$$\times \{-e^{i(\Delta(E_0,\Omega))\hat{x}}\rho_S e^{-i(\Delta(E_0,\Omega))\hat{x}} + \rho_S + c.c.\}, \tag{2.4.24}$$

and hence

$$\langle x|\dot{\rho}_S|y\rangle = -\frac{2F_1}{64\pi^2 m_{\text{nucl}}^2} \int d\Omega |\mathcal{M}(\Omega)|^2$$
$$\times \{-e^{i(\Delta(E_0,\Omega))(x-y)} + 1\}\langle x|\rho_S|y\rangle. \tag{2.4.25}$$

In writing the above, I have implicitly assumed that the system, i.e. the nucleus, has a negligible evolution due to its own Hamiltonian H_S during the time scale of the experiment. In addition, I have labelled $E_{p_0} \equiv E_0$.

I am now in a position to compute the change in the density matrix of the centre of mass of the whole crystal which is comprised of multiple nuclei subject to a large flux of neutrinos from a reactor. It shall be noted that the approximations yield a result which is qualitatively very close to the form of Gallis-Fleming [110] for non-relativistic particles scattering from a mass. Moreover, Eq. (2.4.25) has a very intuitive interpretation, with $\frac{F_1}{64\pi^2 m_{\text{nucl}}^2}d\Omega |\mathcal{M}(\Omega)|^2$ being the incident flux multiplied by the scattering cross section for a solid angle $d\Omega$. It is thus the rate of scattering in

G_F	$1.1664 \cdot 10^{-11} [\mathrm{MeV}^{-2}]$
u	$931.5 [\mathrm{MeV} \cdot \mathrm{c}^{-2}]$
m_{nucl} [111]	$(Z+N)u - 0.00054858 Z \cdot u +$ $(14.4381 Z^{2.39} + 1.55468 \cdot 10^{-6} Z^{5.35}) 10^{-6}$
Flux	$1.7 \cdot 10^{13} [\mathrm{s} \cdot \mathrm{cm}^{-2}]$
Δx	$10^{-14} [\mathrm{m}]$
S(E)	$\frac{1}{\sigma_E \sqrt{2\pi}} e^{-(E-E_0)^2/(2\sigma_E^2)}$
σ_E	$0.75 [\mathrm{MeV}]$
E_0	$2.6 [\mathrm{MeV}]$

Table 2.1: Constants and definitions. G_F denotes the Fermi constant, u the atomic mass unit, m_{nucl} the mass of a nucleus. The flux listed is the projected neutrino flux at a distance of 20 m from the source and Δx refers the superposition size. The function $S(E)$ is a spectral distribution function over the energies E, with standard deviation σ_E and mean energy E_0.

a given solid angle $d\Omega$. Each scattering direction $d\Omega$ imparts a different momentum to the nucleus, which is given by the operator $e^{i(\Delta(E_0,\Omega))\hat{x}}$.

2.4.2 Calculation of the Relative Phase between Superposed Components of a Crystal and its Detection

In order for the formalism to apply to a whole crystal in the form of a bulk material consisting of multiple nuclei scaling as N_{Atoms} and a flux of incoming neutrinos with a spectral distribution of energies $S(E)$, Eq. (2.4.25) will have to be modified to

$$\frac{d\rho_S}{dt} = -\frac{2F_1 \cdot N_{\mathrm{Atoms}}}{64\pi^2 m_{\mathrm{nucl}}^2} \int dE S(E) \int d\Omega |\mathcal{M}(\Omega)|^2$$
$$\left\{ -e^{i(\Delta(E,\Omega))\hat{x}} \rho_S e^{-i(\Delta(E,\Omega))\hat{x}} + \rho_S + c.c. \right\}. \tag{2.4.26}$$

Anti-neutrino production rates for nuclear reactor sources are typically on the order of $r \sim 2 \cdot 10^{20} s^{-1}/\mathrm{GW}_{th}$ [112, 113], with anti-neutrino energies ranging from $1-10\mathrm{MeV}$. Seeing as I assume the detectors to be placed at a distance d=20 m to a nuclear fission reactor source of 4.5

GW$_{\text{th}}$ gigawatt of thermal power, I obtain an estimated flux of

$$F_1 = \frac{r_{4.5\,\text{GW}_{th}}}{4\pi d^2} \sim 1.7 \cdot 10^{13} \text{cm}^{-2}\text{s}^{-1}. \tag{2.4.27}$$

As described earlier, the centre of mass C of the crystal will be initialized in a joint state with with its spin s, in the motional superposition state $|\Psi_0\rangle_S = \frac{1}{\sqrt{2}}\Big(|\uparrow\rangle_s|\bar{x}_0\rangle_C + |\downarrow\rangle_s|\bar{x}_1\rangle_C\Big)$.

Labelling the orthonormal states $|\uparrow\rangle_s|\bar{x}_0\rangle_C$ and $|\downarrow\rangle_s|\bar{x}_1\rangle_C$ with $|0\rangle$ and $|1\rangle$, respectively, for simplicity, I get the initial density matrix in the $\{|0\rangle, |1\rangle\}$ basis as

$$\rho_0 = \frac{1}{2}\begin{pmatrix} 1 & 1 \\ 1 & 1 \end{pmatrix}. \tag{2.4.28}$$

As I have discussed, for low momentum transfer with respect to the inverse of the width of the Gaussians $\bar{x}_0$ and $\bar{x}_1$, they can be treated effectively as position eigenstates $|\bar{x}_0\rangle$ and $|\bar{x}_1\rangle$ in the phase expression. Thus, the evolution of the density matrix in a time Δt, which I call the final density matrix ρ_f is given by

$$
\begin{aligned}
\langle 0|\rho_f|1\rangle &= \langle 0|\rho_S(\Delta t)|1\rangle \\[4pt]
&= \langle 0|\rho_S(0)|1\rangle \\
&\quad - \frac{2F_1 \cdot N_{\text{Atoms}}}{64\pi^2 m_{\text{nucl}}^2}\int dE S(E)\int d\Omega |\mathcal{M}(\Omega)|^2 \\
&\quad \{-e^{i(\Delta(E,\Omega))(\bar{x}_0 - \bar{x}_1)} + 1\}\langle 0|\rho_S(0)|1\rangle \Delta t.
\end{aligned}
\tag{2.4.29}
$$

I then split the solid angle integration into polar and azimuthal integrals over $\tilde{\varphi}$ and θ and choose the parameterization of the problem such that $\Delta(E, \Omega) = E(1 - \cos\theta)$. As a result of the above evolution, I will obtain a final density matrix of the general form

$$\rho_f = \begin{pmatrix} a & Ae^{-i\varphi} \\ Ae^{i\varphi} & b \end{pmatrix}, \tag{2.4.30}$$

in terms of a phase φ and an amplitude A. Unlike in the case of a simple phase acquisition, the amplitude accompanying the off diagonal term of the density matrix, where the phase is encoded, has also decayed because of the open systems treatment. In other words, I am averaging over all angles of scattering, which amounts to averaging over all momenta and incident energies. To extract the effect of the scattering, the centre of mass C will be decoupled using the interferometry methods described in [10, 48]. The relative phase acquired between $|\uparrow\rangle_s|\bar{x}_0\rangle_C$ and $|\downarrow\rangle_s|\bar{x}_1\rangle_C$ will appear between spin states $|\uparrow\rangle_s$ and $|\downarrow\rangle_s$ and be measured after suitable transformations between them. At the end of interferometry, $|\uparrow\rangle_s|\bar{x}_0\rangle_C$ and $|\downarrow\rangle_s|\bar{x}_1\rangle_C$ are mapped to spin states $|\uparrow\rangle_s$ and $|\downarrow\rangle_s$, respectively and I can continue to use $|0\rangle$ and $|1\rangle$ as the basis with the understanding that these now refer to the spin states $|\uparrow\rangle_s$ and $|\downarrow\rangle_s$ which are measured. Unitary operations on spin states typically comprise sending microwave pulses of appropriate frequencies to spin states [102] differing in energies due to the Zeeman effect in an external magnetic field, hyperfine interactions or crystal field anisotropies. The entire toolbox of quantum computation is available and I will use two quantum operations, the Hadamard gate H and the phase gate S [114], on the spins before measuring the populations of $|\uparrow\rangle_s$ and $|\downarrow\rangle_s$.

After computing $\rho_f(x_1, x_2, t)$, upon applying a Hadamard transformation, I effectively rotate the bases from $|0\rangle \to \frac{1}{\sqrt{2}}(|0\rangle + |1\rangle)$ and $|1\rangle \to \frac{1}{\sqrt{2}}(|0\rangle - |1\rangle)$. The extraction of the phase then becomes a matter of calculating the probabilities of measuring $|0\rangle\langle 0|$ or $|1\rangle\langle 1|$. For the final density matrix a Hadamard transformation to the rotated basis yields

$$H\rho_f H = \frac{1}{2}\begin{pmatrix} a + b + 2A\cos\varphi & a - b + 2iA\sin\varphi \\ a - b - 2iA\sin\varphi & a + b - 2A\cos\varphi \end{pmatrix} \qquad (2.4.31)$$
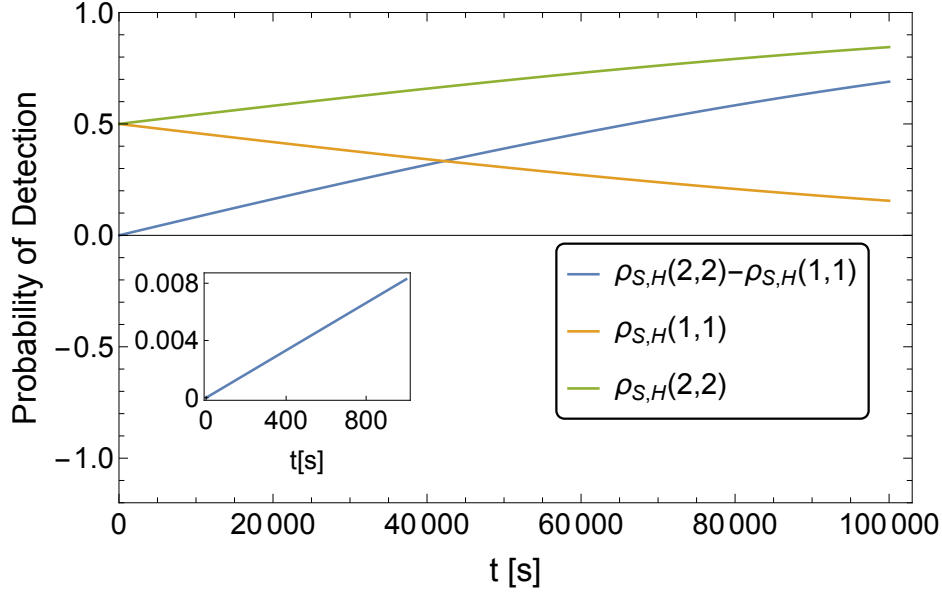
Figure 2.4: Phase accumulation due to coherent neutrino-nucleus scattering from Bismuth. The figure depicts the normalised matrix elements of the nucleus density matrix after performing the operations of a phase gate and subsequent Hadamard on the sensing system. Most notably, the blue line shows the change resulting from the scattering in terms of the sine of the accumulated phase.

and therefore, subtraction of the probabilities $p(0) - p(1)$ results in

$$p(0) - p(1) = 2A\cos\varphi. \tag{2.4.32}$$

As it is sometimes more practical to express the phase for small arguments via the sine, a phase gate of the form

$$S = \begin{pmatrix} 1 & 0 \\ 0 & e^{i\pi/2} \end{pmatrix} \tag{2.4.33}$$

is used before the Hadamard transformation to recover

$$p_{S,H}(1) - p_{S,H}(0) = 2A\sin\varphi. \tag{2.4.34}$$

For a crystal consisting of $N_{\text{Atoms}} = 5 \cdot 10^{21}$ of the element ^{209}Bi (crystal mass m $\sim$ 1 g) and the parameters as given in Tab. 2.1, I observe phase accumulation and its amplitude decay in Fig. 2.4. From the figure it is

clear that at time $\sim 10^5$ s, a very significant phase difference between the components of the superposition with a significant amplitude is obtained for a superposition of size $\Delta x = |\bar{x}_0 - \bar{x}_1| \sim 10^{-14}$ m. Reductions in the mass of the detector would linearly suppress the associated phase and hence one would require a large number of detectors (see section 2.5 for more details). The separation was optimized and this order of magnitude, which is about an order smaller than the average reactor neutrino's de Broglie wavelength, was found to give a detectable phase with minimal damping at $\sim 10^5$ s. This time-scale corresponds to a $\sim \pi/3 \sim 1$ phase shift. About thrice this time corresponds to a π phase shift as the phase growth is linear in time. For a π phase shift, if it can be ensured that there has been no other momenta imparting particle/effect, then this corresponds to the detection of one neutrino by the detector with 100% certainty (a "click" in the detector) as such a phase is measured in a single shot by measuring the spin state in the $\{|+\rangle_s, |-\rangle_s\}$ basis with the outcome $|+\rangle_s$ corresponding to no neutrinos, and the outcome $|-\rangle_s$ corresponding to one neutrino. The chance of more than one neutrino scattering in the given time-scale is exceptionally small. Smaller non-zero phases ascertained at earlier times using Eq.(2.4.34) and multiple measurements to determine probabilities (i.e. repeating the procedure with the same detector or conducting measurements on an array of detectors) will detect the neutrino stream coming from the reactor, but will not be a single shot "click" detector.

2.5   Creation of Quantum Superpositions of Macroscopic Objects

There are three requirements for the setup. Firstly, the crystal should stay suspended against gravity for the duration of $\sim 10^5$ s of the experiment, although I will outline methods of reducing this time by resorting to a detector array rather than a single detector. Using whatever means, the object has to be trapped in the vertical z direction. This could be achieved via the well demonstrated mechanism of diamagnetic levitation which will balance the crystal against gravity. Once created, the quantum superposition of $m \sim 1$ g, $\Delta x \sim 10^{-14}$ m has to be kept coherent for 10^5 s. This is a very long time, but the principal mechanisms of decoherence are known [78], namely the collisions with background gas (controlled by decreasing pressure), black-body radiation emission from the crystal (controlled by cooling the crystal internally) and absorption from the environment. Fig. 2.5 shows the requirements, with the unshaded region (outside the red bounded box) an allowed domain for coherence. It shows that pressures of $P \sim 10^{-16}$ Pa, already achieved in Penning traps, and temperatures of $T \sim 1$K should suffice to retain the extremely long coherence for 10^5 s. The effect of electromagnetic noise from the apparatus to create and probe the superposition is also of importance (analysed to some extent in [10]) and depends on the precise protocol, but essentially the exceptional stability of these sources, along with other proximal electromagnetic sensors will have to be used. For intertial noise, again, other sensors will have to be used to measure and take account of the noise. Alternatively, the detection can be done with two different materials in parallel, with the inertial noise being common. An in-depth noise analysis including vibrational noise will be discussed in future works. The explicit development of the above are beyond the scope of the current work, where I merely want to highlight the possibility
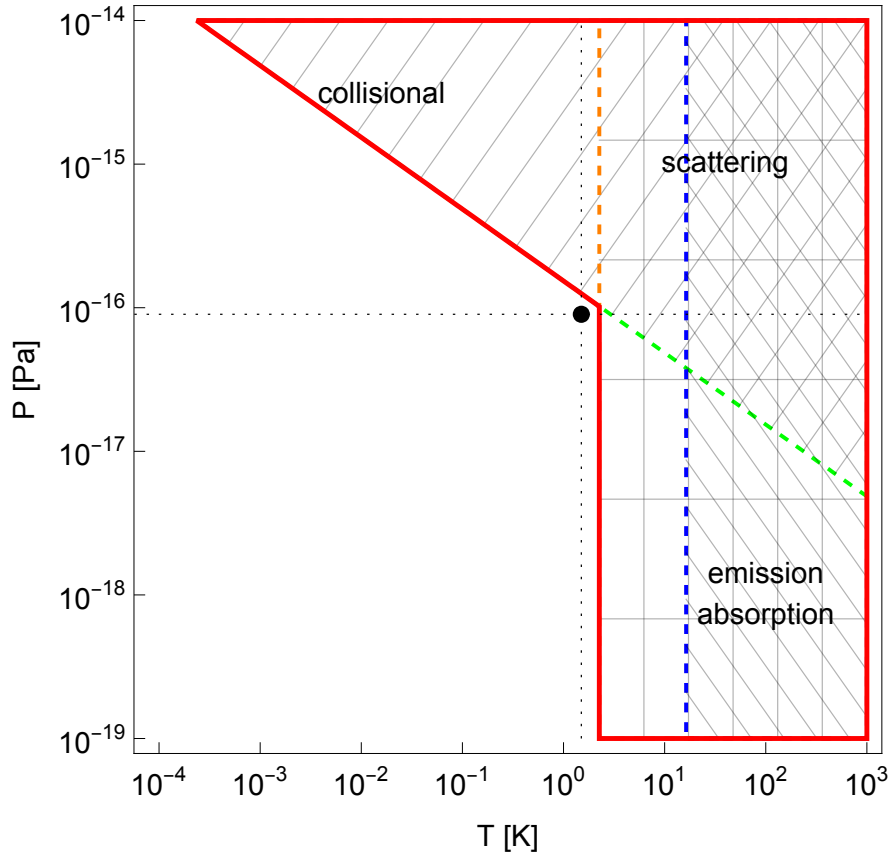
Figure 2.5: The diagram of the allowable region of pressure P and temperature T so that a $m \sim 1$ g crystal in a superposition of two positions separated by $\Delta x \sim 10^{-14}$ m can remain coherent for a time $t \sim 10^5$ s. The allowable region is unshaded. It can be seen that $P \sim 10^{-16}$ Pa and $T \sim 1$ K (the black dot) is an optimal point for the scheme.

of neutrino detection. Methods for creating superpositions of the form $|\Psi_0\rangle = \frac{1}{\sqrt{2}}\left(|\uparrow\rangle_s|\bar{x}_0\rangle_C + |\downarrow\rangle_s|\bar{x}_1\rangle_C\right)$ are still in development. Of course, the method discussed in this work will be applicable to superpositions created by any means, even to superpositions without an ancillary spin system, such as $\frac{1}{\sqrt{2}}\left(|\bar{x}_0\rangle_C + |\bar{x}_1\rangle_C\right)$, as long as there is a mechanism to measure the relative phase between the components by bringing them together to interfere. It is just simpler for a superposition of the form $|\Psi_0\rangle = \frac{1}{\sqrt{2}}\left(|\uparrow\rangle_s|\bar{x}_0\rangle_C + |\downarrow\rangle_s|\bar{x}_1\rangle_C\right)$, as the spin can be measured after the completion of interferometry to measure the phase. Here, I only outline schematics rather than fully detailed schemes. One can use a mass with a single quantum spin$-1/2$ system embedded in it and subject it to magnetic field gradients. The $m \sim 1$ g crystal with an embedded spin

is subjected to a $\frac{\partial B}{\partial x} \sim 10^6$ Tm^{-1} (produced, for example, at a $\sim$ cm distance from the surface of a $\sim$ cm radius wire [10] carrying 10^{13} A m^{-2} current densities). When exposed to this magnetic field gradient for a time $t_{\text{acc}} \sim 10^{-5}$ s, the centre of mass of the crystal acquires opposite final velocities of magnitude $v \sim \frac{\mu_B \frac{\partial B}{\partial x}}{m} \tau \sim 10^{-19}$ ms^{-1} for the $|\uparrow\rangle$ and $|\downarrow\rangle$ components respectively. It is not worth exposing the crystal to the high magnetic field gradient much longer as this gradient, in addition to the Stern-Gerlach splitting, also creates a diamagnetic trap of a frequency $\omega \sim \sqrt{\frac{\chi m}{\mu_0}} \frac{\partial B}{\partial x} \sim 10^5$ Hz in the x direction, which reverses the directions of the opposite accelerations after a quarter period. After this, the x gradient is switched off, and the mass is allowed to freely evolve for the exceptionally long time $\tau \sim 10^5$ s of the experiment in the diamagnetic trap in the vertical z direction. Since there is no trapping/potential in the x direction, the velocity difference is translated to a position difference $\Delta x \sim 2v\tau \sim 10^{-14}$ m. Note that during the stages in which the Stern-Gerlach effect is not used to actively accelerate the crystal, the electronic spin states used in the Stern-Gerlach splitting can be mapped on to nuclear spin states which maintain their quantum coherence for exceptionally long times [115].

Another method to create a quantum superposition will be through using an optomechanical interaction with a quantized microwave field in a cavity, with the cavity field subsequently mapped to spin qubits. In this case, the optomechanical force is sufficient to create the required superposition of a single $m \sim 1$ g mass directly. An electromagnetic field in a number state $|n\rangle$ in a cavity interacts with a crystal passing through it with the coupling strength $g \sim \frac{3V}{4V_c} \frac{\epsilon-1}{\epsilon+1} \omega_L$, where ω_L is the frequency of the electromagnetic field, V is the volume of the crystal, V_c is the cavity waist volume and ϵ the dielectric constant [116]. The optomechanical coupling Hamiltonian is $\hbar g k \hat{n} \hat{x}$, where $\hat{n}$ and $\hat{x}$ are the number and the

position operators of the field and the centre of mass of the crystal respectively, and k is the wavevector of the electromagnetic field. If interacting for a time t_kick, a crystal can receive a velocity kick $v_\text{kick} \sim \frac{\hbar g k n t_\text{kick}}{m}$. Assuming a $t_\text{kick} \sim 1\mu$s during which the 1 g mass traverses through the cavity waist, assuming both $V \sim V_c \sim 1$ cm^3 and $\omega_L \sim 10$ GHz, I get a velocity kick of $v_\text{kick} \sim 10^{-19}$ ms^{-1}. Thus, one can prepare the cavity in a quantum superposition $\frac{1}{\sqrt{2}}(|0\rangle_c + |1\rangle_c)$ and apply a kick to the crystal by letting it fall through the cavity for t_kick. After waiting for a time $\tau \sim 10^5$ s, one obtains a superposition $\frac{1}{\sqrt{2}}(|0\rangle_c|\bar{x}_0\rangle_C + |1\rangle_c|\bar{x}_1\rangle_C)$ [75]. The microwave cavity state can also be mapped to a long-lived nuclear spin states of trapped atoms after the state dependent velocity kicks are over.

Whatever the mechanism of trapping the masses and creating the spatial superpositions, randomness of the forces and pulses will also result in a decoherence at a rate of

$$\Gamma \sim \frac{S_{FF}(\Omega)(\Delta x)^2}{\hbar^2}, \tag{2.5.1}$$

where $S_{FF}(\Omega) = \int \delta F(0)\delta F(t)e^{i\Omega t}dt$ is the force noise spectrum at the frequency $\Omega \sim 1/\tau$ of the experiment. Keeping $\Gamma < 10^{-5}$Hz gives the constraint that random force noise should be kept below $\sqrt{S_{FF}} \sim 10^{-23}$ N/$\sqrt{\text{Hz}}$. Note that in all the above discussions, it is implicit that the interferometry has to be completed. So further spin or cavity field dependent impulses will be required at certain points to stop the growth of Δx and reverse it, as it is accomplished in various interferometric schemes [10, 48].

Note that the phase growth between the components of the superposition when subject to a neutrino flux is linear with time at a constant rate of $\sim 10^{-5}$ Hz, which reflects in population differences as seen form Fig.2.4. At $\sim 10^5$ s, the phase difference of the order π is obtained so

that the final state of the superposition is orthogonal and therefore fully distinguishable from the initial state. If I can further ensure that, by resorting to means such as those described in the context of temperature and pressure, variations of the phase with the location and direction relative to the neutrino source as well as the use of different materials, *only* neutrinos have been scattered during this duration, then an orthogonal spin state detection at $\sim 10^5$ s corresponds to a single neutrino detection (a click), as I am ensuring that nothing else causes a change in the phase and the chance of more than one neutrino having interacted with the gram scale detector is vanishingly small. Using an array of 10^4 such gram scale detectors, I should be able to ensure that one neutrino is detected every 10 s.

Note also that one can shorten both the duration of the experiment to τ/n and the mass required to m/n while keeping the detectability of the phase effect at the same level by using n^4 crystals. Each such crystal will get n times the velocity kick of a single crystal of mass m for the same t_{acc} or t_{kick} (I assume $\tau/n >> t_{\mathrm{acc}}, t_{\mathrm{kick}}$). Thus the time-scale of generation of a superposition of given size Δx will become shortened to τ/n. Note that the phase accrued by *each* crystal in this shorter time will decrease by a factor of n^2, i.e., ϕ becomes ϕ/n^2 as both the time and the mass to which the phase is directly proportional, decrease by n. Because of shot noise scaling n^4 interferometers can measure a phase of ϕ/n^2 with the same accuracy by measuring the spins of each interferometer. However, if one *only* reduced either the mass or the time of the interferometer by a factor of n, I would need n^2 detectors to achieve the same scaling. For example, if I were to split the system to milligram detectors, each with superposition size of 10^{-14}m, (note that this superposition size is much smaller than that required for all other suggested applications, and much smaller than those achieved for atoms and macromolecules), I would need

a million such detectors. Also note that recently large masses have been prepared in nearly the ground quantum state by feedback cooling [89] – so, by similar technology, one should also be able to prepare gram scale masses in pure quantum states, which can be a starting point of creating superpositions.

2.6 Challenges

I have discussed the conditions needed to meet one of the principal challenges, namely environment induced decoherence, in the previous section while discussing the generation of the superposition. However, I discuss below how some of the other requirements may be met.

2.6.1 Satisfying the Requirements of the Crystal Wavepacket

Note that the initial spread σ_c of each of the superposed Gaussian wavepackets of the crystal are required to satisfy a couple of conditions in order to meet some of the simplifying approximations of the calculations. Note that the position degree of freedom of all the nuclei (being part of a solid) are, to a good approximation (at least at the temperatures I consider) rigidly tied to the centre of mass of the crystal and thereby has the same position spread σ_c as that of the whole crystal. As stated in section 2.2, I require $\sigma_c \lesssim 1/q_x$, relating to the momentum transferred, which in this case corresponds to ensuring $\sigma_c \lesssim \Delta x \sim 10^{-14}$ m. On the other hand, I also require the initial maximum momenta of the crystal $k_i \sim 1/\sigma_c \lesssim m_{\text{nucl}} \sim 10^{-17}$ m, which stems from the assumption of the heavy nucleus being effectively at rest. Thus there is a window. An initial diamagnetic trap of 10^5 Hz in the x direction will therefore suit the objective of this work, with the ground state spread of the centre of mass of the crystal in such a trap being $\sim 10^{-16}$ m.

2.6.2 Coherence Length of the Neutrino

The consideration of processes involving neutrinos brings about several unknowns, one of which is the particle's coherence length. In ref [117] the authors opted for a wave-packet treatment of the neutrino and estimated that an energy uncertainty of $\sigma_{wp} = \frac{\sigma_\nu}{E(p_\nu)} \sim 0.01$ or larger would influence decoherence and dispersion effects and thereby reduce the detector efficiency of reactor anti-neutrino oscillation experiments. I take this value as a reference to estimate whether a scattering event could resolve the position of the nucleus and hence spoil the superposition. Considering $\sigma_x \sigma_\nu \sim \frac{\hbar}{2}$, I obtain an uncertainty $\sigma_x \sim 3 \cdot 10^{-12}$ m for a neutrino with energy $E_\nu \sim 10$ MeV. This means that a neutrino with $\sigma_{wp} \sim 0.01$ would indeed be able to resolve the position of any quantum object in a superposition larger than σ_x. Seeing as the matter of the actual wave packet shape and coherence length of the neutrino is not solved, the proposed experiment may also be able to serve as a means of testing the validity of plane wave approximations of the neutrino wave packet. Depending on the true wave packet shape of the neutrino, I expect to observe either a coherent phase gain or a decoherence effect.

2.6.3 Lattice Defects

The authors of [118] considered the structural damage effects of dark matter and neutrino scattering on dense materials with defect centers, such as nitrogen vacancy centers in diamond. In general, the deposited kinetic energies will exceed typical lattice binding energies of $\mathcal{O}(10)$eV. Hence, I anticipate the scattering of a neutrino to lead to the formation of such damage clusters, though they can be expected to be significantly smaller in size. Based on the analysis in [118], I estimate that a nucleus recoiling with an average kinetic energy of 3keV could generate $\mathcal{O}(10)$ lattice defects or interstitial sites. I require that these sites are created in such a manner that I cannot tell from which part of the superposition the

neutrino has scattered. Here this requirement is naturally fulfilled as the size of the superposition is much smaller than the interatomic spacing in the lattice.

2.6.4   Distribution of Momentum

It is the centre of mass of the whole crystal which is coupled to the embedded spin used for the superposition creation/recombination and the phase read-out. However, the neutrino is initially going to impart its energy to one of the nuclei in the whole crystal. At this stage, the energy imparted is localized to this nucleus, but the centre of mass already has the imparted momentum; however, the crystal cannot be considered as all rigidly connected nuclei moving together, which is required for the embedded spin to sense the transferred momentum. A local phonon is excited in the crystal at the site of the scattering neutrino. However, phonon relaxation times in crystals are generally $\sim 1 - 100$ ns [119], after which the energy would have been transferred to the centre of mass of the whole crystal.

2.7   Summary

I have described the detection of neutrinos from the relative phase they impart between the components of a quantum superposition of two spatially localized states of the centre of mass of a crystal. As naturally there is a distribution of momentum after the scattering, this process also causes a decoherence in addition to imparting a change in the relative phase. I thus formulated a master equation technique to evolve the full density matrix of the COM of a crystal under the scenario of the scattering of a relativistic particle from it. Solving that, I found that the optimal detection requires a ~ 1 g mass placed in a quantum superposition of states separated by a distance $\Delta x \sim 10^{-14}$ m. For completeness, I have also suggested a schematic and parameter domain by adopting

which such superpositions could be achieved and maintained for the long duration of the experiment, although much more analysis will be required for realistic scenarios.

It is worth clarifying the role of the various ingredients of the method proposed herewith. The superposition serves as a means to detect the momentum recoil k of the crystal in terms of the relative phase $k\Delta x$. Of course, that will happen for a crystal of any mass, including individual atoms in a superposition of states separated by Δx. However, in that case the cross section is very small. For a crystal of N_{Atoms}, the cross section is amplified N_{Atoms} times. While an uncorrelated collection of N_{Atoms} in the same superposition state will have the same cross section, the neutrino will only scatter from one of those atoms, and one has to measure each atom after appropriate basis rotations in order to measure whether one of them obtained a phase. In the case of a crystal with a single embedded spin, the phase gained by the neutrino hitting any one of the nuclei is mapped on to the relative phase between the COM states of the whole crystal. This is because of the very strong correlations between the positions of the atoms the N_{Atoms}, since they are all either clustered around the state $|\bar{x}_0\rangle$ or the state $|\bar{x}_1\rangle$. The positions of all the atoms are entangled when the centre of mass is placed in the superposition $|\bar{x}_0\rangle + |\bar{x}_1\rangle$. Moreover, due to the very mechanism of the interferometry, the embedded spin or other ancillary system is also entangled with the centre of mass during the interferometry, so that at the end, the phase can be estimated exclusively by measuring this single spin. The reason that I have used a regime in which the scattering from each nulceus is coherent is because it enhances the cross section by N^2 times (N being the number of neutrons in a nucleus), which makes the times-scales about 10^4 times less than what it would have been otherwise.

It is important to clarify that going to either higher or lower energy neutrinos is not a trivial problem. For higher energies, it is true that the cross section increases as $\propto E^2$, where E is the energy of the incident neutrinos. However, the momentum transferred may be too high and knock a nucleus completely out of the crystal so that the momentum is not imparted to the rest of the crystal. Moreover, $k\Delta x \sim 1$ implies that much smaller superpositions Δx will have to be used, which implies a great difficulty in satisfying the simplification assumptions $1/m_{\mathrm{nucl}} << \sigma_c << \Delta x \sim 1/k$ and the calculations will be needed to be performed in much more generality. For lower energies, cross section can both decrease due to the $\propto E^2$ effect or increase due to scope of scattering coherently from all atoms of the crystal. However, producing a larger $\Delta x \sim 1/k$ superposition becomes much more difficult, especially for the masses as large as the ones that are needed here.

The technique presented in this work should be adaptable to any relativistic particles scattering off a quantum superposition with appropriate modifications. Moreover, neutrinos will form a background to any other signals one may want to detect. The calculations here show that even a substantially large mass in a quantum superposition of distinct spatial states can remain coherent for a very long time close to a source of neutrinos so that there is an ample window for the detection of other signals.

Chapter 3

On the Optimality of the Superposition Size

Contents

Exploiting quantum mechanics for sensing offers unprecedented possibilities. State of the art proposals for novel quantum sensors often rely on the creation of large superpositions and generally detect a field. However, what is the optimal superposition size for detecting an incident particle (or an incident stream of particles) from a specific direction? This
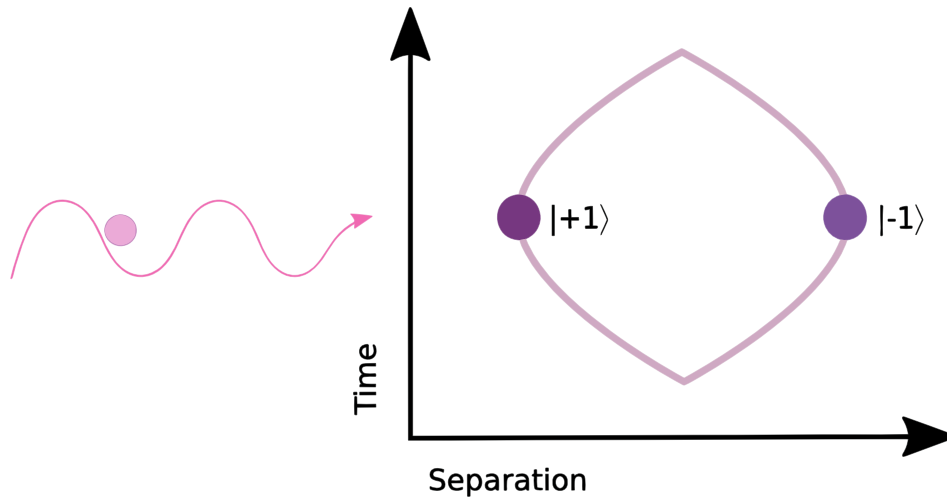
Figure 3.1: Basic schematics of a particle scattering from a quantum object (purple spheres) in a Stern-Gerlach type interferometric experiment.

question is nontrivial as, in general, this incident particle will scatter off with varied momenta, imparting varied recoils to the sensor, resulting in decoherence rather than a well defined measurable phase. By considering scattering interactions of directional particulate environments with a system in a quantum superposition, I find that there is an "optimal superposition" size for measuring incoming particles via a relative phase. As a consequence of the anisotropy of the environment, I observe a novel feature in the limiting behaviour of the real and imaginary parts of the system's density matrix, linking the optimality of the superposition size to the wavelength of the scatterer.

This chapter is based on the pre-print E. Kilian et al., "Optimal Superpositions for Particle Detection via Quantum Phase", Publisher: arXiv Version Number: 1, `10.48550/ARXIV.2307.15186` (2023).

3.1 The Context

Quantum sensing with matter-wave interferometers has prompted the development of a variety of commercial technologies and experiments,

offering some of the most precise sensors. State of the art experiments encompass research in the areas of metrology [121], gravimetry [47, 122], geophysics [123, 124] and quantum foundational principles [10, 13, 48, 72]. The quantum object as a sensor, whether atom or nanoparticle, is typically prepared in a near-classical or Gaussian (which can be somewhat quantum in the sense of being squeezed) initial state [96, 125], but the full potential of quantum mechanics becomes apparent when non-Gaussian quantum states are utilized. Optimization of the experimental setup and parameters in order to extract exquisitely weak signals is of utmost importance.

The sensing of potentials, such as a linear potential generated by electrostatic fields, or the gravitational potential near earth, often necessitates the realisation of quantum superposition states with large spatial separation δx between the superposed components, since the accumulated phase $\Delta \phi$ increases with increasing separation. For example, an object of mass m held in a quantum superposition of localized states separated vertically by δx for a time interval τ near earth's surface acquires the celebrated Collela Overhauser Werner (COW) phase of $\Delta \phi \sim mg\delta x\tau/\hbar$, while the phase due to the curvature of a proximal mass is $\propto (\delta x)^2$. For a dynamical monochromatic classical field of wavenumber magnitude k, again, while phase $k\delta x$ is defined modulo 2π, it surely does not harm the coherence of the superposition to have $\delta x > 1/k$. At the other extreme is the detection of particulate matter interacting with the sensing system via a coupling term. This is, however, phenomenologically different as it cannot be correctly approximated by a classical field, unless in the macroscopic limit of a very large number of particles in a coherent state. In this limit, the focus has been on detection of the particulate source via the decoherence of a quantum superposition as the particles scatter off the sensor mass, typically imparting random

momenta [13]. Thus, the measurement of a coherent phase is typically not associated with the detection of particles. Thus, as far as current understanding goes, the intuition is that if fields are concerned, a larger δx is typically better, and surely not harmful, while for particles, decoherence would be the prime signature.

In this work, I show that *neither* of the above intuitions are correct for particulate matter incident from a given direction: I find that there exists an *optimal* superposition size for quantum sensing in scattering experiments, depending on the characteristics of the environmental source. This arises due to a competition between a coherent phase contribution and a decoherence contribution. To illustrate this effect, I consider the basic blueprint consisting of an incoming particle (the signal) that scatters from a massive quantum system placed in a spatial superposition (the sensor). Working within the framework of open quantum systems, I compute the effects arising from the interaction of the system with a directional particulate matter environment and discuss in how far the superposition size impacts the accumulation of the phase. Contrary to expectations, reading the phase imparted due to scattering in the presence of decoherence induced by the same scattering may not be optimized at a trivial point. Aside the above fundamental point, I also present an application in single photon detection. I conclude by discussing the implications of the findings for present-day sensing experiments aimed toward capturing signatures of other/general scattering particles.

3.2   Sensing in Scattering Experiments

The appearance of the classical from the quantum is the cause of long-standing debate and a key element of all interpretations of quantum mechanics. The process of environmental decoherence offers one mechanism for this quantum-to-classical transition, through which the sup-

pression of certain superpositions of quantum states following measurements performed on a sensing system initially in superposition of several eigenstates may be described. In this context, the interaction of a superposed quantum object with gaseous particles and photons will constitute a measurement, since it involves the transfer of positional information into the environment. Following the work of Joos and Zeh [126], the authors of [110] have extended and generalised the mathematical model reflecting the localizing mechanism under the critical assumption that the scattering of the (weakly coupled) environment does not significantly disturb the sensor.

Concretely, in a non-relativistic theory, the reduced density matrix of a system interacting with a particulate environment through scattering [110] is governed by the following master equation

$$\frac{d\rho_S(\mathbf{x}, \mathbf{x}')}{dt} = \frac{1}{i\hbar}\langle\mathbf{x}|[H, \rho_S]|\mathbf{x}'\rangle - F(\mathbf{x} - \mathbf{x}')\rho_S(\mathbf{x}, \mathbf{x}') \tag{3.2.1}$$

where

$$F(\mathbf{x} - \mathbf{x}') = \int dq n(q) v(q) \int \frac{d\Omega d\Omega'}{4\pi} p(\Omega, \Omega')$$
$$\times (1 - e^{i(\mathbf{q} - \mathbf{q}')\cdot(\mathbf{x} - \mathbf{x}')})|f(\mathbf{q}, \mathbf{q}')|^2. \tag{3.2.2}$$

This result is derived through a careful perturbative treatment of the scattering interaction. The function $p(\Omega, \Omega')$ is a probabilistic function with incoming (outgoing) scattering angle θ (θ'), and where $p(\Omega, \Omega') = 1$ is the typical scenario where scatterers impart momentum from all directions. The quantities $n(q)$ and $v(q)$ refer to the number density and speed of particles with wavenumber q, the latter of which is closely related to their wavelength λ and momentum $\mathbf{q}$. The scattering amplitude of the relevant interaction process is denoted as $f(\mathbf{q}, \mathbf{q}')$. $F(\mathbf{x} - \mathbf{x}')$ is the localization rate. If it is real-valued, the sensing system exhibits a loss

of coherence over time, while an imaginary contribution manifests in the appearance of a phase $e^{i(\mathbf{q}-\mathbf{q}')\cdot(\mathbf{x}-\mathbf{x}')}$. Differences in the phases arising at $\mathbf{x}$ and $\mathbf{x}'$ can be measured and exploited in sensing with quantum systems.

For an incoming particle of wavelength λ, there are two regimes of interest to investigate in order to describe the behaviour of the sensing system. In the long-wavelength regime, where $\lambda \gg \delta x$, with $\delta x = |\mathbf{x}-\mathbf{x}'|$, the phase term in Eq (3.2.2) becomes small enough to warrant an approximate treatment of the exponential function by means of a Taylor-expansion of the argument. Calculating the expansion up to second order, a quadratic dependency of the localization rate on the superposition size $F(\mathbf{x}-\mathbf{x}') \propto \frac{1}{2}q^2(\hat{\mathbf{n}}-\hat{\mathbf{n}}')\cdot(\mathbf{x}-\mathbf{x}')^2$ is revealed. Assuming isotropy of the environmental source, the linear term in the expansion averages to zero due to the integration over the product of an even and odd function in directions $(\hat{\mathbf{n}}, \hat{\mathbf{n}}')$.

In the short-wavelength regime, the exponential function in Eq. (3.2.2) oscillates rapidly and hence, quickly averages out when performing the integrals. Master equations of the form Eq. (3.2.1) can be mapped to equations of the Lindblad-type and for $\hat{L}_k$ corresponding to a physical observable, namely that of the position operator $\hat{L}_k = \hat{\mathbf{x}}$, the equation that governs the evolution of the system can be expressed as

$$\frac{d\hat{\rho}_S(t)}{dt} = -i[\hat{H}_S, \hat{\rho}_S(t)] - \frac{\kappa}{2}[\hat{\mathbf{x}}[\hat{\mathbf{x}}, \hat{\rho}_S(t)]]. \qquad (3.2.3)$$

The quantity κ incorporates information contained in the localization rate $F(\mathbf{x} - \mathbf{x}')$ as written in Eq. (3.2.2). If a given environment is not isotropic and the scattering particles are instead impinging from a specific direction, the limiting behaviour reveals the emergence of an optimal superposition size where the detection of the particle is also from the phase imparted. In order to demonstrate this effect, I resort to a numerical

analysis of the reduced system density matrix for two explicit examples of the differential cross-section.

3.3 On the Emergence of an Optimal Superposition Size

To illustrate the emergence of an optimal superposition size, I will focus on two cases of a well-known example from the literature [110], where a special form of the differential cross-section is taken to be

$$|f(\mathbf{q}, \mathbf{q}')|^2 = gq^m \frac{1}{2}\left(1 + \left|\frac{\mathbf{q}\mathbf{q}'}{q^2}\right|^2\right). \tag{3.3.1}$$

For $m = 0$ and $g = r_e^2$ as the square of the classical electron radius, one recovers a differential cross-section for Thompson scattering, while values of $m = 4$ and $g = a^6|\frac{\epsilon-1}{\epsilon+1}|^2$ with a as the scatterer's radius and ϵ being the dielectric constant lead to a description of Rayleigh scattering.

In the long wavelength-limit, I am again able to expand the small exponent in Eq. (3.2.2) in orders of δx. In what follows, I assume the directional source of particles to travel along the z-Axis. This assumption is reflected in the choice of $p(\Omega, \Omega') = \delta(\theta)\delta(\phi)/\sin\theta$ for a spherical coordinate system. Further, I select the coordinates of the incoming and outgoing particle momenta to be $\mathbf{q} = q(0, 0, 1)$, $\mathbf{q}' = q(\cos\varphi'\sin\theta', \sin\varphi'\sin\theta', \cos\theta')$, where I notably keep the magnitude of the particle's momentum unchanged, which is a valid approximation for negligible momentum transfers.

If $m = 0$ and the superposition is oriented along z, calculating the Taylor expansion up to second order in δx and performing the subsequent

angular integration results in the following terms of the localization rate

$$F(\mathbf{x} - \mathbf{x}') = \int dq n(q) v(q) g\Big(-\frac{2}{3} iq\delta x \tag{3.3.2}$$
$$+ \frac{7}{15} q^2 \delta x^2 + \mathcal{O}(\delta x^3)\Big).$$

Similarly, I obtain a barely modified equation for $m = 4$

$$F(\mathbf{x} - \mathbf{x}') = \int dq n(q) v(q) g q^4\Big(-\frac{2}{3} iq\delta x \tag{3.3.3}$$
$$+ \frac{7}{15} q^2 \delta x^2 + \mathcal{O}(\delta x^3)\Big).$$

Concluding these findings, I observe the emergence of an imaginary linear (Hamiltonian) term in the master equation describing the evolution of the reduced density matrix. Importantly, this behavior appears to be independent of the exact form of the differential scattering cross section, surfacing merely due to the directional momentum impartment of the incoming scatterers. The limit of small wavelengths is more difficult to treat analytically due to the rapid oscillatory behaviour of the integrand. I can however significantly reduce the complexity of the problem by fixing the axes of the incoming particle to be aligned with the orientation of the superposition along the z-direction. I then subsequently employ the Jacobi-Anger expansion, noting the cosine appearing in the exponent. Through this type of expansion, the trigonometric function in the exponential is expressed in the basis of its cylindrical harmonics via the relation $e^{iz\cos\theta} = J_0 + 2\sum_{n=1}^{\infty} i^n J_n(z) \cos n\theta$. Figure 3.2 displays the trend of the real and imaginary parts for multiple values of the ratio $\frac{\delta x}{\lambda}$, where the factor $g = r_e^2$, effectively scaling the plot's y-axis, has been neglected and the momentum integration has not yet been performed (corresponding to the case of a delta-function in incident momentum and hence a specific q scattering). The visible decay of the imaginary phase contribution to zero and the saturation of the real part nonetheless confirm the expected limiting behaviour for large values of $\frac{\delta x}{\lambda}$. However, the way in
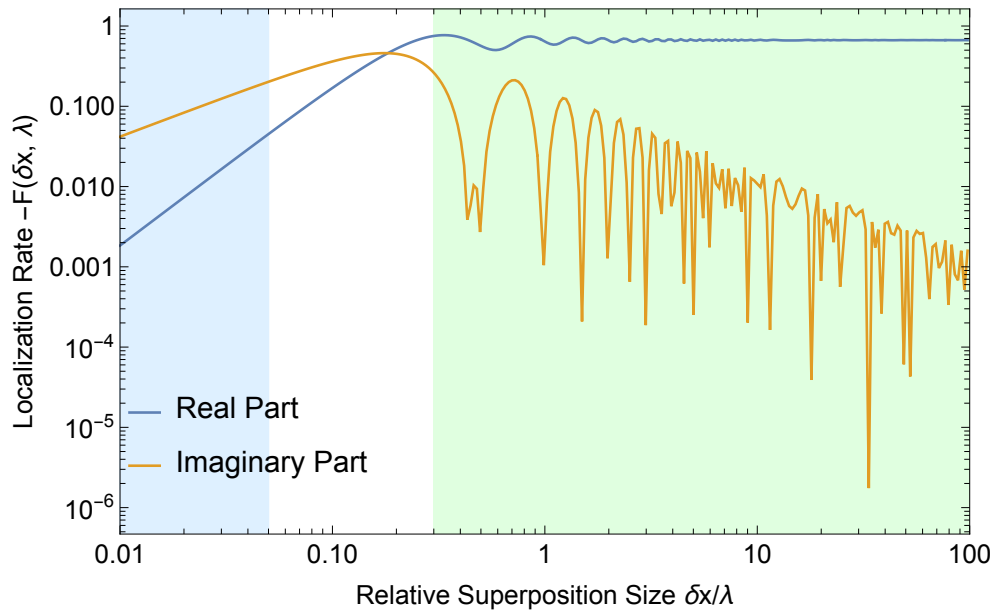
Figure 3.2: Short- and long-wavelength regimes of imaginary and real part quantum state evolution for Thompson scattering. The quantity λ is the incoming particle's wavelength and δx is the size of the superposition. The blue and the orange line refer to the real and imaginary parts of the localization rate's contribution to the quantum system's off-diagonal respectively. The real part is typically used to quantify decoherence. The imaginary part vanishes in an isotropic situation. In case of a directed (non-isotropic) source such as a wind however, the imaginary part can be used for sensing, as it gives a phase evolution.

which these limits are reached differs significantly from the case of random uniform scattering, where the exponential contribution habitually averages out due to rapid oscillations.

The second example for $m = 4$ reveals a similar trend, though the resulting localization function is again scaled by an additional factor of q^4 and the coupling g is dependent on the dielectric constant of the sensing material. Employing previous calculation methods will therefore lead to the same qualitative observation, namely the emergence of an optimal "Goldilocks zone" in relation to the accumulation of phase as is indicated in Fig. 3.2 and indirectly in Fig. 3.4.

3.4 Experimental Signature

The field of matter-wave interferometry offers a catalogue of schemes that enable the extraction of the phase contribution arising due to a scattering interaction. A popular approach is founded in the Stern-Gerlach interferometry of spin-mechanical systems [48, 84], where the magnetic manipulation of a mesoscopic test-mass with an embedded spin, such as levitated diamond with a nitrogen-vacancy-center, is used. After the initialization of the sensing system in a center-of-mass (COM) motional state $|c\rangle$ and a superposition of (its embedded) spin states $\frac{1}{\sqrt{2}}\big(|+1\rangle + |-1\rangle\big)$, the system is allowed to evolve. This evolution is spin-state dependent and leads to a spatial splitting of the COM, resulting in a combined quantum state of the form $|\psi(t)\rangle = \frac{1}{\sqrt{2}}\big(|c_{s=+1}(t)\rangle|+1\rangle + |c_{s=-1}(t)\rangle|-1\rangle\big)$. The difference in distinct phases arising between the components of the superposition due to a scattering interaction can be measured upon completion of the interferometer by means of orthogonal spin-state measurements, since the motional wave-packet is recombined at the end of the experiment. For an illustration of this scenario, see Fig. 3.1 on page 92.

For a simple initial density matrix

$$\rho = \frac{1}{2}\begin{pmatrix} a & Ae^{i\phi} \\ Ae^{-i\phi} & b \end{pmatrix}, \tag{3.4.1}$$

one method of extracting phase-differences arising between the off-diagonal components is to apply $\pi/2$-phase and Hadamard gate transformations S and H to the quantum state, which effectively results in a projection of the phases onto the diagonal.

$$\rho_f = HS\rho S^\dagger H \tag{3.4.2}$$

$$= \frac{1}{4}\begin{pmatrix} a+b+2A\sin\phi & a-b+2iA\cos\phi \\ a-b-2iA\cos\phi & a+b-2A\sin\phi \end{pmatrix}$$

Subtracting the (diagonals) probabilities $\rho_{f,11} - \rho_{f,22} = A\sin\phi$, hence relates to the sine of the accumulated phase ϕ. This experimental signature is plotted in Fig. 3.3 for the normalized initial state where $\rho_{11} = \rho_{22} = \rho_{12} = \rho_{21} = 1/2$ and evolved final states with varying values $\phi = 2\pi\delta x/\lambda$, at times $t = [0,5]s$. For the sake of generality, I have not chosen a specific distribution for the number density and speed of the particles and set the quantity $g = 1$ while the momentum distribution is taken to be a delta function (definite momentum), effectively plotting the contributions from $F(x-x')$ resulting from the angular integrations. Specific values for these quantities and subsequent integration over the momentum will lead to a shifted optimal range for the relative superposition size $\delta x/\lambda$. Although I do not strictly define the notion of optimality, it should be implicitly clear that values of the relative superposition size leading to a phase contribution of $\mathcal{O}(1)$ are considered as such. Benchmarking the range of suitable values for $\delta x/\lambda$ to, say, $\sin(\phi) = 0.95$ is one possible way of defining the window of optimality.
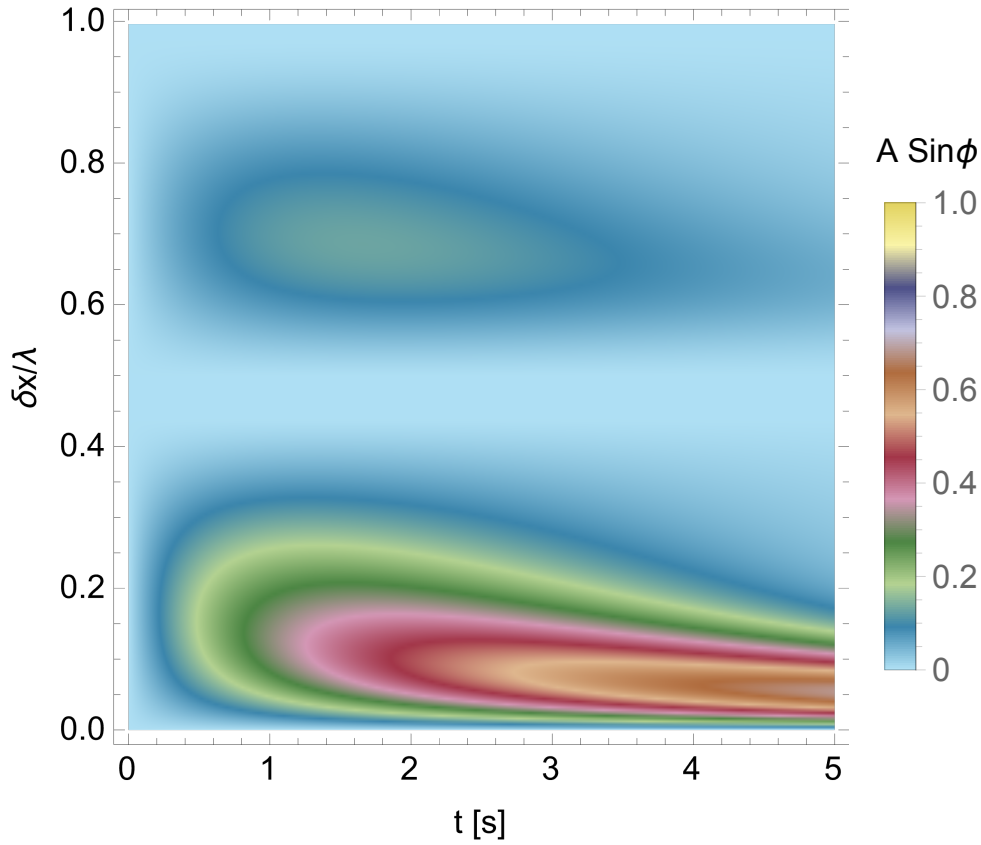
Figure 3.3: Accumulated phases (depth coloration) for varying ratios of $\delta x/\lambda$ over a time interval $t = [0,5]$ s, assuming Thompson scattering with $m = 0$ and constant pre-factors $n(q)v(q)g = 1$. The orange colored region in the plot indicates the maximization of the phase signature, which in turn is determined by the non-vanishing first order contribution in Eq. 3.3.2.

3.4.1   Single Photon Detection

To give a concrete example of an experimental application, I analyse the potential benefit of this novel effect for the detection of spatially shaped single-photons, such as those which may be emitted from a quantum dot source. With the aim of operating the sensing system as a "click" detector, I introduce what I term the detection efficiency as follows

$$\eta = \langle -|\rho_{in}|-\rangle \tag{3.4.3}$$
$$= \frac{1}{2}(1 - (\rho_{12}(t = 1s) + \rho_{21}(t = 1s))).$$

The efficiency η plotted in Fig. 3.4 quantifies the distinguishability of a system initially prepared in a superposition state $\rho_{in} = |+\rangle\langle+|$ from
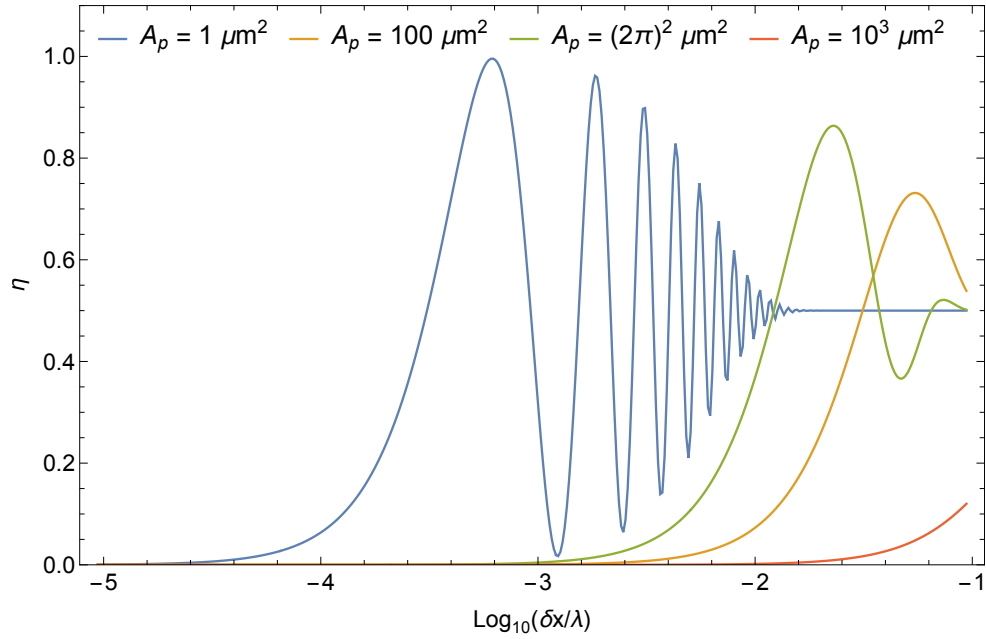
Figure 3.4: Quantum efficiency η for Rayleigh scattering of single photons with $\lambda = 1064$ nm on a 0.1 micron-sized sphere, assuming different spatial photon profiles A_p.

its final state. If the scattering of a photon results in a π phase shift, projecting the initial quantum state into the orthogonal state $|-\rangle$, the efficiency approaches its maximum. Figure 3.4 shows the crucial dependency of η on the choice of $\delta x / \lambda$ for different magnitudes of areal photon flux, corresponding to $n(q)v(q)$ in the master equation. Here, I consider a 0.1 micron sized particle. The contributions at a fixed time $t = 1s$ have been labeled as A_p and correspond to the spatial profile of a single photon, which in turn is related to $n(q)v(q)\tau \sim \frac{10^6}{A_p}$. Whereas certain choices of the superposition size will be suitable for operating the sensing system as a single photon detector, others will result in phase shifts that render the system insensitive to the signal.

3.5 Implications for Quantum Sensing and Experiments

The above observations are of critical relevance to experiments where a stream of imminent particles scattering from a superposition has a

unique or preferred direction and the environment cannot be treated in the fashion of an isotropic bath. Conversely, a similar observation can be made for a superposed object that is not held in place, but instead propagating with a given velocity with respect to the environment, such as a crystal with horizontal velocity in a motional superposition state moving through a gas of particles in the lab frame. A heuristic mathematical treatment of this scenario is described in the next section.

Several emergent experiments and technologies, especially in the context of quantum gravimetry, rely on the acceleration of the quantum mechanical sensor. Any such setup will be influenced by non-isotropic sources interacting with the sensing apparatus. I therefore want to emphasize the importance of the choice of the superposition size in relation to phase contributions arising through these directional effects. In turn, I also highlight the potential of these findings to be exploited for the purpose of intentional enhancement of a particular anisotropic signal.

3.6 Master Equation with Boosted Superposition

I now consider, without solving explicitly, the situation when a superposition sensor is boosted and moves through a static environment (in a loose sense a reverse of the situation considered in the previous chapters). Consider this general class of master equations in the Lindblad form

$$
\begin{aligned}
\frac{d\hat{\rho}_S(t)}{dt} = &-i[\hat{H}_S, \hat{\rho}_S(t)] \\
&- \sum_k G(k)\Big(\hat{L}_k\hat{\rho}_S(t)\hat{L}_k^\dagger - \frac{1}{2}\{\hat{L}_k^\dagger\hat{L}_k, \hat{\rho}_S(t)\}\Big)
\end{aligned} \tag{3.6.1}
$$

where the kernel $G(k)$ is a function of the momentum k and $\hat{L}_k = e^{ik\hat{x}}$. This non-dissipative master equation is in itself an approximation of the dissipative model, where $\hat{L}_{\hat{p},k} = e^{ik\hat{x}}\hat{B}(\hat{p}, k)$. Let $\sqrt{G(k)}$ be absorbed into

$\hat{L}_{\hat{p},k}$ and assume that the sensing system is not stationary, but instead moves towards a given direction. I therefore apply a boost operation to the superposed object, essentially computing $\rho_S \mapsto U\rho_S U^\dagger$, where $U = e^{\frac{i}{\hbar}mv\hat{x}}$ with v being the boost velocity and m denoting the mass of the system.

$$U\dot{\hat{\rho}}_S(t)U^\dagger = -\sum_k \Big(\hat{L}_{\hat{p},k}U\hat{\rho}_S(t)U^\dagger\hat{L}_{\hat{p},k}^\dagger$$
$$-\frac{1}{2}\{\hat{L}_{\hat{p},k}^\dagger\hat{L}_{\hat{p},k}, U\hat{\rho}_S(t)U^\dagger\}\Big), \qquad (3.6.2)$$

$$\dot{\hat{\rho}}_S(t) = -\sum_k \Big(U^\dagger\hat{L}_{\hat{p},k}U\hat{\rho}_S(t)U^\dagger\hat{L}_{\hat{p},k}^\dagger U$$
$$-U^\dagger\frac{1}{2}\{\hat{L}_{\hat{p},k}^\dagger\hat{L}_{\hat{p},k}, U\hat{\rho}_S(t)U^\dagger\}U\Big) \qquad (3.6.3)$$

The operator $\hat{B}(\hat{p},k)$ transforms as $U^\dagger\hat{B}(\hat{p},k)U = \hat{B}(\hat{p}+\bar{k},k)$, where $\bar{k} = mv$. I then use the relation $\hat{L}(\hat{p}+\bar{k},k) = \hat{L}(\hat{p},k-\bar{k})$. It essentially states that adding momentum to the system is taking momentum away from the environment. This yields a master equation of the form

$$\dot{\hat{\rho}}_S(t) = -\sum_k G(k-\bar{k})\Big(e^{i(k-\bar{k})\hat{x}}\hat{B}(\hat{p},k-\bar{k})\hat{\rho}_S(t)$$
$$\times \hat{B}^\dagger(\hat{p},k-\bar{k})e^{-i(k-\bar{k})\hat{x}}$$
$$-\frac{1}{2}\{\hat{B}^\dagger(\hat{p},k-\bar{k})\hat{B}(\hat{p},k-\bar{k}), \hat{\rho}_S(t)\}\Big). \qquad (3.6.4)$$

The result illustrates a change in $G(k)$ (and therefore the function $p(\Omega, \Omega')$) under the influence of a boost operation performed on the system. Thus the evolution of the density matrix should be able to capture this movement of the interferometer. I leave concrete calculations following from the reverse case discussed in this section as a matter of future investigation.

3.7 Summary

Considering two limiting regimes for the wavelength of an incoming scatterer interacting with a quantum sensor, I have numerically shown that the imaginary contribution arising due to the interaction is, in specific scenarios, non-vanishing. This relative phase may be used for the detection of weak environmental signatures. Moreover, I have observed the emergence of an optimal parameter-choice for the superposition size δx when it comes to measuring special types of particulate environments. The findings presented will doubtlessly result in improvements of state-of-the-art quantum sensors and may be utilized to enhance signals which are typically difficult to capture.

Chapter 4

Non-Gaussian Superpositions & Entanglement in Atom-Nanoparticle Ion Trap Hybrids

Contents

In this chapter I examine the creation of superpositions of mesoscopic and macroscopic objects for levitated optomechanical systems through their interaction with atoms. Although fundamentally distinct, this work is in close relation to cold ion experiments, where Mølmer-Sørensen [127] gates relying on optical manipulation and the Coulomb repulsion be-

tween ions or techniques such as that proposed by Mintert and Wunderlich [128] utilising an inhomogenious magnetic field are used to generate entanglement between the ions. In contrast, I discuss here the feasibility of creating and evidencing a spatial superposition of the nanoparticle through the appearance of interference fringes and comment on a novel method for the experimental verification of the entanglement between the atom and nanoparticle.

4.1 Schematic Protocol
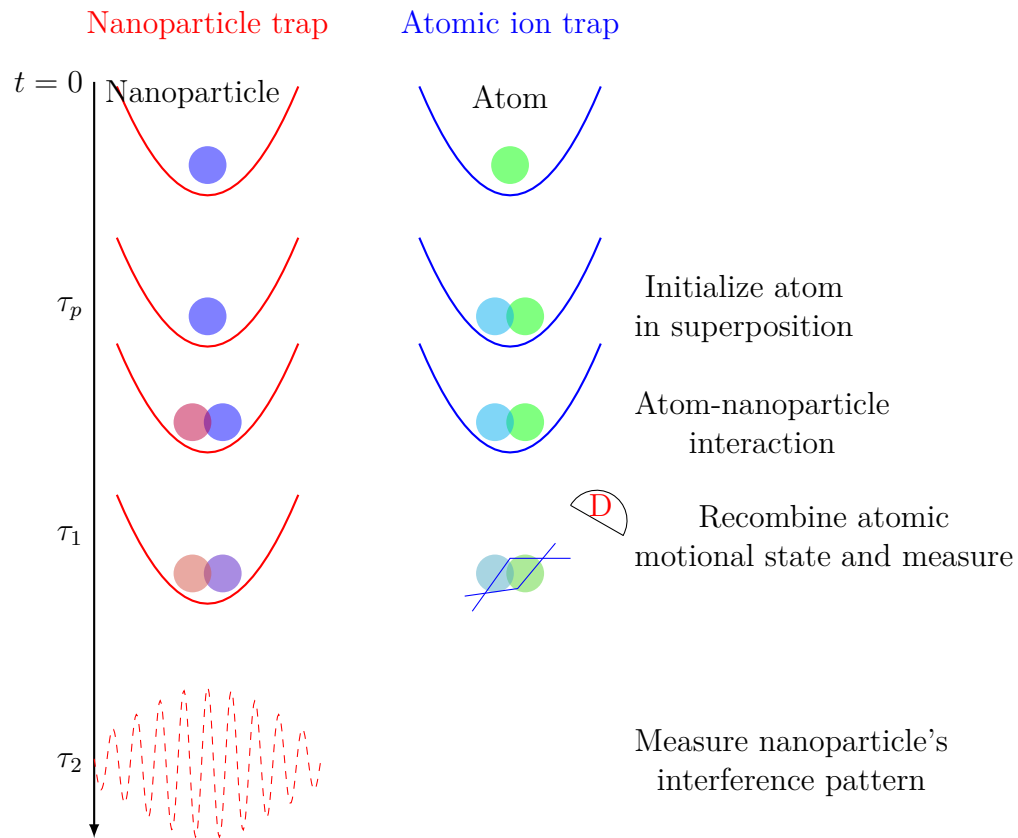
Figure 4.1: Schematic protocol for generating entanglement between a single trapped (charged) atom and a nanoparticle consisting of several tightly-bound atoms. In step (1), both particles are trapped. Subsequently in step (2) a pulse τ_p is used to place the atom in superposition. (3) The particles are allowed to interact for a time τ_1, at which point the atom is measured as indicated by the detector symbol D in red. (4) The nanoparticle is allowed to evolve for a time τ_2, then its fringes in position are measured throughout multiple repetitions of the protocol.

The implementation of sensing schemes relying on joint quantum sys-

tems consisting of trapped atoms and mesoscopic particles may be experimentally challenging, yet it is a promising avenue for the practical realisation of large-mass superpositions and the study of entanglement between the two systems. Entanglement of an atom-nanoparticle system, where the atom is trapped in the intensity maxima of a trapped nanoparticle's evanescent field has been studied in [129]. Here, I am considering a different experimental configuration. I investigate the concrete scenario of a single and separately trapped atom interacting with an object consisting of several tightly-bound atoms, such as a nanosphere, which is equally confined in a harmonic potential. Trapping both in an ion trap, I essentially use the electrostatic interaction between them to generate an entangled state and from that, a quantum superposition of states of the nanoparticle. To quantify the superposition sizes in the nanoparticle one can realistically expect to achieve and subsequently evidence the entanglement generated due to the atom-nanoparticle interaction, I am considering the following protocol:

- The nanoparticle and atom are held in two separate ion-traps of frequencies ω_n and ω_a.

- Through the application of a light pulse, the atom is initialized in a superposition of two spatially distinct states. This light-pulse aided generation of the superposition of the atom is so fast that the nanoparticle hardly evolves during this interval. The assumption is justified if the pulse time for the generation $\tau_p \ll 1/\omega_n, 1/g$, where g is the coupling of the atom and nanoparticle, to be calculated later, in frequency units.

- The systems interact for a time τ_1, during which the atom is held in the superposition state. A motional superposition is induced in the nanoparticle.

- Through the application of another pulse, the atomic motional

state is recombined. The population states are measured in the $|+\rangle$, $|-\rangle$ basis.

- Evolving the nanoparticle state for a time $t = \tau_2 = \frac{\pi}{2\omega_n}$ effects a rotation in phase space, resulting in the delocalized nanoparticle wavepackets overlapping in position, leading to the appearance of interference fringes in position.

- The interference pattern is measured by measuring the position of the nanoparticle and obtaining the spatial distribution of its position. On the other hand, this position detection will be accomplished by scattering light from the nano-object and detecting an interference pattern between incident and scattered light, which is a technique for very high resolution position detection [130, 131]. Methods for mapping the interference fringes to a spatial qubit can in principle also be used to witness the atom-nanoparticle entanglement.

4.2   Mathematical Model

The dynamics of the center-of-mass motion of the harmonically trapped nanoparticle correspond to that of a harmonic oscillator, whereas the atom's motion along with its internal levels will be treated as an effective two-state system – this requires assumptions about the state of the atom, as will be clarified below. A quantum superposition in the initial state of the atom will naturally influence the evolution of the more massive object due to their interaction. There are two main ways in which the atomic interferometer for trapped motional states can be realised

- through the application of a magnetic field gradients in a Stern-Gerlach type interferometer, or

- through the application of Raman pulses, for example in a Ramsey-Bordé interferometer or in an ion trap

which will result in slightly different Hamiltonians for the atomic system, while the Hamiltonian for combined atom-nanoparticle system will be characterized only through an effective coupling strength g which will depend on the Coulomb interaction. For a Stern-Gerlach interferometer with an external gradient $\frac{\partial B_z}{\partial x}$, and $B_z = 0$ at $x = 0$, the atomic Hamiltonian is

$$H_a = \hbar\omega_a b^\dagger b + \mu_B \delta_x \frac{\partial B_z}{\partial x}\tilde{\sigma}_z(b + b^\dagger), \qquad (4.2.1)$$

where $\delta_x = \sqrt{\frac{\hbar}{2m_a\omega_a}}$ and the creation operators b and $b^\dagger$ are for the quantized centre of mass vibration in the x direction. The last term is the Zeeman term, which gives the magnetic gradient Stern-Gerlach force F_{mag} and $\tilde{\sigma}_z = |\uparrow\rangle\langle\uparrow| - |\downarrow\rangle\langle\downarrow|$. In order to keep uniform notation and to make the nano-particle superposition creation method independent of *how* the atomic superposition is created, the symbols $|e\rangle$ and $|g\rangle$ will be used for the spin state $|\uparrow\rangle$ and $|\downarrow\rangle$, even though they are degenerate in the absence of a magnetic field. At a time $t = 0$, the magnetic field gradient is switched on for an interval $\tau_p = \pi/\omega_a$ which results in the state

$$|e\rangle|L\rangle + |g\rangle|R\rangle, \qquad (4.2.2)$$

where $|L\rangle$ and $|R\rangle$ are spatially localized states separated by a splitting

$$l_{\max} \sim \frac{F_{mag}}{m_a\omega_a^2} = \frac{\mu_B}{m_a\omega_a^2}\frac{\partial B_z}{\partial x}. \qquad (4.2.3)$$

For a Raman-pulse method in an ion-trap, after conducting all the approximations relating to the internal level energy differences, detunings, trap frequency and simultaneously setting the red and blue detuned transition, the effective Hamiltonian of the atom is recovered as described in

Eq. (1.3.21), giving

$$H_a = \hbar\eta\Omega_{\text{eff}}(b^\dagger + b)\sigma_y, \qquad (4.2.4)$$

which generates a superposition of the same form as Eq. (4.2.2) up to local unitary operations on the atomic state, with $l_{\max}$ being given as

$$l_{\max} \sim \frac{F_{Raman}}{m_a\omega_a^2} = \frac{\hbar\eta\Omega_{\text{eff}}}{m\omega_a^2\delta_z} = \frac{\hbar k\Omega_{\text{eff}}}{m_a\omega_a^2}, \qquad (4.2.5)$$

where the Raman pulse induced force is understood to be imparted as the equivalent of one photon momentum kick $\hbar k$ per Rabi oscillation period $1/\Omega_{\text{eff}}$.

I discuss here the calculation after choosing the first scenario, although it should hold similarly for the second scenario. To do so, I consider the quantum motion of the nanoparticle in the x direction to be coupled to the atom, the other directions of the nanoparticle trap are so tightly confined that they are hardly affected. A simplistic model for the interaction of a charged atom and nanoparticle can be made if one assumes that the atom's spatial superposition of size $l_{\max}$, once generated, can be held still for the interaction time τ_1. Since both particles are electrically charged, they interact via the Coulomb potential

$$V_{Coulomb} = \frac{e^2}{4\pi\epsilon_0|x_n - x_a|} \qquad (4.2.6)$$

where x_n and x_a are the respective positions of the nanoparticle and atom. Normally, if none of the systems are placed in spatially delocalized superpositions, and cooled to their ground states at the centres of their traps, they are at positions $-d/2$ (nanoparticle) and $d/2$ (atom). This implies that the centres of the traps are separated by d. For small variations in the positions $x_n \to -d/2 + \delta x_n$ and $x_a \to d/2 + \delta x_a$, the

potential becomes

$$V_{Coulomb} = \frac{e^2}{4\pi\epsilon_0 d}\frac{1}{1 + (\delta x_a - \delta x_n)/d}. \tag{4.2.7}$$

Expanding the expression in terms of the redefined distance parameter $((\delta x_a - \delta x_n)/d)$ up to second order while requiring that $\delta x_a, \delta x_n \ll d$ results in the three terms

$$V_{Coulomb} \sim \frac{e^2}{4\pi\epsilon_0 d}\left(1 + \frac{\delta x_a - \delta x_n}{d} - \frac{(\delta x_a - \delta x_n)^2}{d^2}\right). \tag{4.2.8}$$

Quantization of the positions will promote the variations δx_n and δx_a in the expression to operators, of which only combinations of the form $\hat{x}_n\hat{x}_a$ would generate entanglement between the two quantum systems. Moreover, since the position of the atom is either $d/2 - l_{\max}/2$ for the component $|e\rangle|L\rangle$ or $d/2 + l_{\max}/2$ for the component $|g\rangle|R\rangle$, its position $\hat{x}_a$ can be replaced by the discrete operator

$$\hat{x}_a = d/2 + \frac{l_{\max}}{2}\sigma_z, \tag{4.2.9}$$

where

$$\sigma_z = |e\rangle|L\rangle\langle e|\langle L| - |g\rangle|R\rangle\langle g|\langle R|. \tag{4.2.10}$$

This substitution has also been done in Ref. [132]. It leads to an effective interaction Hamiltonian between the nano-particle and atom that is of the form

$$H_{n,a}^{int} = \hbar g_C \sigma_z (a + a^\dagger), \tag{4.2.11}$$

where $a, a^\dagger$ are the creation/annihilation operators for the harmonic oscillator nanoparticle. There will be a nanoparticle Hamiltonian $H_n = \hbar\omega_n a^\dagger a$ added to the above interaction Hamiltonian. In writing the above, the

term proportional to $a + a^\dagger$ has been omitted, as it is simply a position shift of the centre of the nanoparticle's harmonic well. The coupling g_C in frequency units is given by

$$g_C = \frac{e^2 \delta x_n l_{\max}}{\hbar \, 4\pi\epsilon_0 d^3}, \tag{4.2.12}$$

where $\delta x_n = \sqrt{\frac{\hbar}{2m\omega_n}}$ is the initial position of the nanoparticle and $l_{\max}$ the maximal spatial separation of the atomic superposition state. The full Hamiltonian is then

$$H_{n,a} = \hbar\omega_n a^\dagger a + \hbar g_C \sigma_z (a + a^\dagger), \tag{4.2.13}$$

where the first term corresponds to the evolution of the nanoparticle and the last contribution encompasses interactions of the nanoparticle with the ion, for which the strength of the interaction is determined by the coupling g_C. The individual evolution of the atom is negligible, because I have assumed that the superposition of the atom is generated and held still while $H_{n,a}$ acts.

4.3 Spatial Superposition Generation

At the beginning of the protocol, the atom is initialized in a superposition of motional states. Since the motion is coupled to the intrinsic energy levels, the combined initial state of the nanoparticle and atom is

$$|\alpha\rangle(|e\rangle|L\rangle + |g\rangle|R\rangle) \tag{4.3.1}$$

where it is assumed that the nanoparticle is prepared in a coherent state $|\alpha\rangle$. Until further comment, I shall henceforth implicitly carry forward the ground and excited states in the full expression and denote the atom's superposition state merely by the left and right components of the motional degree of freedom. The time evolution in step 3 of the protocol is

obtained by applying the unitary

$$U(t) = e^{-i\frac{H_{n,a}t}{\hbar}} = e^{-i\omega_n a^\dagger a t - i g_C \sigma_z (a + a^\dagger) t} \tag{4.3.2}$$

$$= D^\dagger\left(\tfrac{g_C}{\omega_n}\sigma_z\right) e^{-i\omega_n a^\dagger a t} D\left(\tfrac{g_C}{\omega_n}\sigma_z\right) \tag{4.3.3}$$

for the duration of a time $t = \tau_1$. Thus, the initial state evolves to

$$|\psi(t = \tau_1)\rangle = N\Big(|\alpha e^{-i\omega_n \tau_1} + \tfrac{g_C}{\omega_n}(1 - e^{-i\omega_n \tau_1})\rangle|L\rangle \tag{4.3.4}$$

$$+ |\alpha e^{-i\omega_n \tau_1} - \tfrac{g_C}{\omega_n}(1 - e^{-i\omega_n \tau_1})\rangle|R\rangle\Big).$$

where N is an appropriate normalisation factor. Assuming a ground state cooled nanoparticle, $\alpha = 0$ and the quantum state simplifies to

$$|\psi(t = \tau_1)\rangle = \frac{1}{\sqrt{2}}\Big(|\tfrac{g_C}{\omega_n}(1 - e^{-i\omega_n \tau_1})\rangle|L\rangle \tag{4.3.5}$$

$$+ |-\tfrac{g_C}{\omega_n}(1 - e^{-i\omega_n \tau_1})\rangle|R\rangle\Big)$$

$$= \frac{1}{\sqrt{2}}\Big(|+\beta\rangle|L\rangle + |-\beta\rangle|R\rangle\Big), \tag{4.3.6}$$

where $\beta = \tfrac{g_C}{\omega_n}(1 - e^{-i\omega_n \tau_1})$. To reveal the entanglement and verify the superposition in the nanoparticle through the presence of interference fringes, the motional wavepacket of the atom is brought back together as $|L, e\rangle \to |C, e\rangle$ and $|R, g\rangle \to |C, g\rangle$, where C is now the center, and the interferometer is closed so that the joint ion-nanoparticle state becomes

$$|\psi(t = \tau_1)\rangle = N\Big(|\tfrac{g_C}{\omega_n}(1 - e^{-i\omega_n \tau_1})\rangle|e\rangle \tag{4.3.7}$$

$$+ |-\tfrac{g_C}{\omega_n}(1 - e^{-i\omega_n \tau_1})\rangle|g\rangle\Big)|C\rangle$$

$$= N\Big(|+\beta\rangle|e\rangle + |-\beta\rangle|g\rangle\Big)|C\rangle \tag{4.3.8}$$

In order for highly non-Gaussian spatial superposition states of the nanoparticle to be produced, a measurement has to be performed in the x-basis $\{\tfrac{1}{\sqrt{2}}(|g\rangle + |e\rangle), \tfrac{1}{\sqrt{2}}(|g\rangle - |e\rangle)\}$ of the atom. Conditionally, the nanoparticle

(a) Wigner function of $|\psi_+(\tau_2)\rangle$.   **(b)** Wigner function of $|\psi_-(\tau_2)\rangle$.
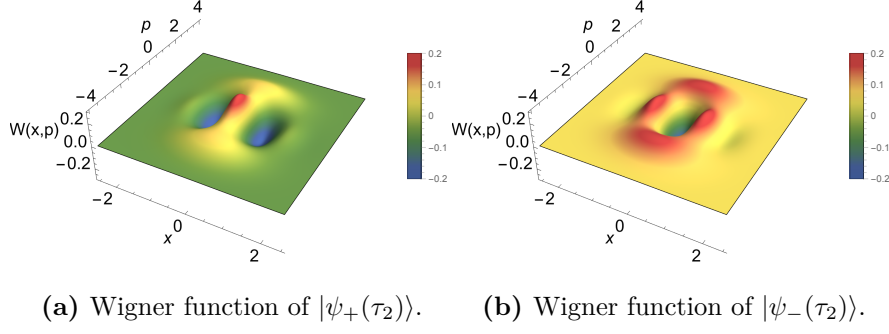
Figure 4.2: Three-dimensional depiction of the Wigner functions W(x,p) for the states (a) $|\psi_+(\tau_2)\rangle$ and (b) $|\psi_-(\tau_2)\rangle$ for displacement values $\beta = \sqrt{2}$. The colour bars indicate the value of W(x,p) for different values of position x and momentum p. In the above, I have used adimensional $x \to \sqrt{2}\sigma_1 x$ and corresponding p.

is projected to the state

$$|\psi_{n,\pm}\rangle = N_\pm(\beta)\Big(|+\beta\rangle \pm |-\beta\rangle\Big) \tag{4.3.9}$$

where the normalization is $N_\pm(\beta) = \frac{1}{\sqrt{2\pm 2e^{-2|\beta|^2}}}$. From the normalization, one can find the probability for each outcome. For the $|+\rangle = \frac{1}{\sqrt{2}}\Big(|g\rangle + |e\rangle\Big)$ state, it is $N_+^2(\beta)$ while for the $|-\rangle = \frac{1}{\sqrt{2}}\Big(|g\rangle - |e\rangle\Big)$ state, it is $N_-^2(\beta)$. At this point in the experiment, the conditional quantum state of the nanoparticle is recovered as

$$|\psi_{n,\pm}\rangle = N_\pm(\beta)\left(\frac{1}{2\pi\delta x_n^2}\right)^{\frac{1}{4}} \int_{-\infty}^{\infty}\left(e^{-\frac{(x+2\beta\delta x_n)^2}{4\delta x_n^2}} \pm e^{-\frac{(x-2\beta\delta x_n)^2}{4\delta x_n^2}}\right)|x\rangle dx \tag{4.3.10}$$

in position space, where I have assumed the wavepacket representation of a coherent state

$$\psi(x,0) = \left(\frac{1}{2\pi\delta x_n^2}\right)^{\frac{1}{4}} e^{-\frac{(x-x_0)^2}{4\delta x_n^2}+ip_0 x} \tag{4.3.11}$$

to have $p_0 = \langle p \rangle = 0$ for the sake of simplicity. The state in Eq. 4.3.10 is non-classical, as is demonstrated by the Wigner functions $W(x,p) = \frac{1}{\hbar\pi}\int_{-\infty}^{\infty}\psi^*(x+y)\psi(x-y)e^{\frac{2ipy}{\hbar}}dy$ in Fig. 4.2. To evidence this nonclassicality experimentally, one has to look for interferometric fringes, while

the measurements generally available are position measurements, which could be highly precise. In the state described in Eq. 4.3.10, the fringes are actually in the momentum quadrature. Thus to obtain position fringes, the system is now allowed to evolve for a time $t = \tau_2 = \frac{\pi}{2\omega_n}$, corresponding to a $\pi/2$ rotation in phase space that maps momentum to position $p \leftrightarrow m\omega_n x$ (or $x \leftrightarrow \frac{p}{m\omega_n}$). The time-evolution of coherent states of a simple harmonic oscillator [133] is given by

$$\Phi_\beta(x,t) = \left(\frac{1}{2\pi\delta x_n^2}\right)^{\frac{1}{4}} e^{-i\frac{\omega_n t}{2}} e^{\frac{\beta^2 e^{-2i\omega_n t} - |\beta|^2}{2}} e^{-\frac{1}{4\delta x_n^2}(x - 2\delta x_n \beta e^{-i\omega_n t})^2} \quad (4.3.12)$$

for a general coherent state. The time evolution at time τ_2 follows accordingly and is

$$\Phi_\beta(x,\tau_2) = \left(\frac{1}{2\pi\delta x_n^2}\right)^{\frac{1}{4}} e^{-i\frac{\pi}{4}} e^{\frac{-\beta^2 - |\beta|^2}{2}} e^{-\frac{1}{4\delta x_n^2}(x + i2\delta x_n \beta)^2} \quad (4.3.13)$$

which simplifies again if β is assumed to be real. For the superposition in the nanoparticle state, the evolution yields

$$|\psi_{n,\pm}(\tau_2)\rangle = \int dx N_\pm(\beta) \left(\frac{1}{2\pi\delta x_n^2}\right)^{\frac{1}{4}} \left(e^{-i\frac{\pi}{4}} e^{-\beta^2} e^{-\frac{1}{4\delta x_n^2}(x + i2\delta x_n \beta)^2}\right. \quad (4.3.14)$$
$$\left. \pm e^{-i\frac{\pi}{4}} e^{-\beta^2} e^{-\frac{1}{4\delta x_n^2}(x - i2\delta x_n \beta)^2}\right)|x\rangle$$
$$= \int dx N_\pm(\beta) \left(\frac{1}{2\pi\delta x_n^2}\right)^{\frac{1}{4}} e^{-i\frac{\pi}{4}} e^{-\frac{x^2}{4\delta x_n^2}} \left(e^{-\frac{i\beta x}{\delta x_n}} \pm e^{+\frac{i\beta x}{\delta x_n}}\right)|x\rangle$$

The probability for finding the nanoparticle in the position x is then

$$p(x) = |\langle x|\psi_{n,+}(\tau_2)\rangle|^2 \quad (4.3.15)$$
$$= |N_+(\beta)|^2 \left(\frac{1}{2\pi\delta x_n^2}\right)^{\frac{1}{2}} e^{-\frac{x^2}{2\delta x_n^2}} 4\cos^2\left(\frac{\beta x}{\delta x_n}\right)$$

with a sine term for the state of opposite sign. This implies that in order to obtain the fringes, the position x has to be measured better than to a

precision $\pm\epsilon$ given by

$$\epsilon \sim \delta x_n/\beta. \tag{4.3.16}$$

As the envelop function $e^{-\frac{x^2}{2\delta x_n^2}}$ decays over the ground state spread δx_n, the measurement of the fringes has to occur within this Gaussian, implying $\beta > 1$ is needed, which in turn implies a detection precision ϵ to better than the standard quantum limit [134] δx_n. For a phonon loss rate [135] of the nanoparticle of γ, a decoherence rate is proportional to $\Gamma \sim \gamma|\beta|^2$, which requires γ to be reduced to below an appropriate value.

4.4 Estimates in Physical Realizations

From Eq. (4.3.14) it follows that the size of the spatial superposition of the nanoparticle which is created is

$$\Delta x_n = 4\beta\delta x_n \sim 4\frac{g_C}{\omega_n}\delta x_n. \tag{4.4.1}$$

To determine the strength of the coupling g_C, the size of the atomic superposition $l_{\max}$ has to be estimated first. Aiming for an $l_{\max} \sim 1\,\mu$m, I will now examine the requirements for that. Following the Stern-Gerlach method, with an atomic mass of $m_a \sim 10^{-25}\,$kg and $\omega_a \sim 100\,$kHz, yields

$$l_{\max} \sim \frac{\mu_{\mathrm{B}}}{m_a\omega_a^2}\frac{\partial B_z}{\partial x} \sim 10^{-8}\frac{\partial B_z}{\partial x}\,\mathrm{m}. \tag{4.4.2}$$

Thus by choosing $\frac{\partial B_z}{\partial x} \sim 100$ T/m, a superposition size $l_{\max} \sim 1\,\mu$m can be obtained. Similarly following the Raman scheme, with a Rabi frequency $\Omega_{\mathrm{eff}} \sim 1\,$MHz [136], but with n_{pulse} number of pulses,

$$l_{\max} \sim n_{\mathrm{pulse}}\frac{\hbar k\Omega_{\mathrm{eff}}}{m_a\omega_a^2} \sim n_{\mathrm{pulse}}10^{-8}\,\mathrm{m}. \tag{4.4.3}$$

In conclusion, a hundred Raman pulses [18] can generate the desired superposition. For a distance $d \sim 10\,\mu$m between the traps, a nanoparticle of mass $m_n \sim 10^{-14}$ kg in a trap of frequency $\omega_n \sim 100$ Hz [137] and a ground state spread $\delta x_n = \sqrt{\frac{\hbar}{2m_n\Omega_n}} \sim 0.1$ Å, the coupling g_C becomes

$$g_C = \frac{e^2 \delta x_n l_{\max}}{\hbar \; 4\pi\epsilon_0 d^3} \sim 10^4 \text{Hz}. \tag{4.4.4}$$

Thus, the size of the nanoparticle superposition is

$$\Delta x_n = 4\frac{g_C}{\omega_n}\delta x_n \sim 4\text{nm}. \tag{4.4.5}$$

The value of the superposition in phase space $\sim 4\beta \sim 400$. While the above estimates for $l_{\max}$ and hence Δx_n amount to relatively large displacements, smaller superposition sizes with smaller displacements β should only be much easier to generate. Assuming $\beta \sim 10$, the required spatial resolution [130] is 10 picometer.

4.5   Verification of Entanglement

In addition to verifying the superposition through the fringe patterns in position as described, it may also be of interest to try and verify the atom-nanoparticle entanglement directly. All previous measurements of entanglement of two continuous variable systems have either been through an indirect method or only for Gaussian two-mode entangled states through Gaussian (EPR) witnesses [138]. If the states in Eq. (4.3.8) are labelled $|+\beta\rangle = |0\rangle, |-\beta\rangle = |1\rangle$, the result is a two qubit entangled state. Note that it is not the maximally entangled state

$$\frac{1}{\sqrt{2}}\Big(|0\rangle|e\rangle + |1\rangle|g\rangle\Big) \tag{4.5.1}$$

unless $\beta \to \infty$, but it is already a reasonable approximation for $\beta \sim 2$ as the overlap decays as $\langle 0|1\rangle \sim e^{-4|\beta|^2}$. A recently proposed method to

evidence the entanglement of the atom and nanoparticle is based on the notion of encoding a spatial qubit in the nanoparticle's spatial degree of freedom [139], inspired by work on encoding photonic spatial qubits [140]. This treatment has so far been applied to freely propagating, untrapped systems but not yet been investigated for nanoparticles in ion traps. In general, to measure the entanglement of the state in Eq. (4.3.14), an entanglement witness such as $W = X \otimes X + Y \otimes Y$ has to be measured. A measurement in the X basis for the atom and a measurement of the nanoparticle in the X basis as well, and similarly measuring both in the respective Y basis. The measurement of the ion in two complementary bases is straightforward: $\{\frac{1}{\sqrt{2}}\big(|g\rangle + |e\rangle\big), \frac{1}{\sqrt{2}}\big(|g\rangle - |e\rangle\big)\}$ for the X-basis and $\{\frac{1}{\sqrt{2}}\big(|g\rangle + i|e\rangle\big), \frac{1}{\sqrt{2}}\big(|g\rangle - i|e\rangle\big)\}$ for the Y-basis. When spatial qubit states $|\psi_{+,n}\rangle = \frac{1}{\sqrt{2}}(|0\rangle \pm |1\rangle)$ are prepared, the probability distributions $p_\pm(x)$ of positions in the fringe pattern correspond to X eigenvalues of $+1$ and -1 respectively. Similarly, when the state $|\psi_{+i,n}\rangle = \frac{1}{\sqrt{2}}(|0\rangle \pm i|1\rangle)$ is prepared, the probability distributions of positions in the fringe pattern $p_{i\pm}(x)$ correspond to Y eigenvalues of $+1$ and -1 respectively. The measurements in the X and Y bases on the atom therefore project the nanoparticle's quantum state into either of the states $N_{\pm(i)}(\beta)(|+\beta\rangle \pm (i)|-\beta\rangle)$ with $N_\pm(\beta) = \frac{1}{\sqrt{2 \pm 2e^{-2|\beta|^2}}}$ and $N_{\pm i}(\beta) = \frac{1}{\sqrt{2}}$. However, the above described measurement of the nanoparticle in the X and Y basis for the spatial qubit states is non-trivial and does not exactly correspond to measuring an interference pattern as the latter is obtained by averaging over a large ensemble. The form of the spatial qubit Pauli operators have not been rigorously worked out in terms of position measurements (assuming that this is the most easily measured observable – the position of a nanoparticle). Rather, only a heuristic argument has been made. The construction of appropriate X_n and Y_n operators for the nanoparticle, when it is treated as a qubit, will now be described formally. Subtleties regarding the explicit computation of the entanglement witness that have

not been discussed in [139] will be addressed.

4.5.1   Pauli Operators for the Spatial Qubit

In a number of trapped ion or photon experiments, the spin of an ion or the polarisation of a photon are regularly used to define a two-level system. The quantum bit can however also be encoded in a continuous variable system, such as the center-of-mass motion of a trapped nanoparticle. The Pauli basis, together with the identity operator, allows for the decomposition of any 2×2 density operator representing the qubit state. This decomposition is also known as the Bloch decomposition. An ideal qubit can hence be characterized through the Pauli matrices, which are themselves traceless hermitian and unitary. A Pauli operator is typically expressed through combinations of the complete orthonormal computational basis states $\{|0\rangle, |1\rangle\}$ or the basis states $\{|+\rangle, |-\rangle\}$. For example, the Pauli matrix σ_x, which can be understood as both a π-rotation around the x-axis of the Bloch sphere and a representation of the quantum analogue of a logical NOT operation, can be written in terms of its eigenbasis as $\sigma_x = |+\rangle\langle+| - |-\rangle\langle-|$. I will use this notation to find an expression for a position measurement operator intended to realise a Pauli measurement on the nanoparticle. Since the spatial distribution of the nanoparticle positions will be used to construct these Pauli operators by placing detectors at specific locations, it will become apparent that the implementation of ideal Pauli measurements is non-trivial because the nanoparticle basis states $|\psi_{+,n}\rangle$, $|\psi_{-,n}\rangle$ are not orthogonal in an approximate sense.

To realise a logical X_n measurement on the nanoparticle and construct a spatial qubit, the Pauli operator $\sigma_{x_n} = |\psi_{+,n}\rangle\langle\psi_{+,n}| - |\psi_{-,n}\rangle\langle\psi_{-,n}|$, where the subscript n labels the quantum state as the state of the nanoparticle, has to be measured. However, since this operator can-

not be readily measured due to the absence of spatial fringes at τ_1, an equivalent operator $\sigma_{x_n}(\tau_2) = X_n$ has to be constructed which acts on the time evolved state. It is imperative to express the operator in the position basis using a truncated form of the identity resolution

$$X_{\text{spatial}} = \frac{1}{4L^2} \int_{-L}^{L} \int_{-L}^{L} |x\rangle\langle x|X_n|x'\rangle\langle x'|dxdx'. \qquad (4.5.2)$$

Since the atom has been measured accordingly in its X basis and the nanoparticle has been projected and time evolved into either of the two states in Eq. (4.3.14), these states (with the subscript n dropped) can be used for the construction of X_{spatial}. Writing $X_n = |\psi_+(\tau_2)\rangle\langle\psi_+(\tau_2)| - |\psi_-(\tau_2)\rangle\langle\psi_-(\tau_2)|$,

$$\begin{aligned}
X_{\text{spatial}} &= \frac{1}{4L^2} \int_{-L}^{L} \int_{-L}^{L} \langle x|X_n|x'\rangle|x\rangle\langle x'|dxdx' \qquad (4.5.3) \\
&= \frac{1}{4L^2} \int_{-L}^{L} \int_{-L}^{L} \langle x|\psi_+(\tau_2)\rangle\langle\psi_+(\tau_2)|x'\rangle|x\rangle\langle x'|dxdx' \\
&\quad - \frac{1}{4L^2} \int_{-L}^{L} \int_{-L}^{L} \langle x|\psi_-(\tau_2)\rangle\langle\psi_-(\tau_2)|x'\rangle|x\rangle\langle x'|dxdx'.
\end{aligned}$$

It can already be seen from this general expression that the resulting operator X_{spatial} is not diagonal in the position basis. Inserting the expression of the time-evolved superposition states at τ_2, one recovers

$$\begin{aligned}
X_{\text{spatial}} &= \frac{1}{L^2} \int_{-L}^{L} \int_{-L}^{L} N_+^2(\beta)\Big(\frac{1}{2\pi\delta x_n^2}\Big)^{\frac{1}{2}} e^{-\frac{(x^2+x'^2)}{4\delta x_n^2}} \qquad (4.5.4) \\
&\quad \times \cos\Big(\frac{\beta x}{\delta x_n}\Big)\cos\Big(\frac{\beta x'}{\delta x_n}\Big)|x\rangle\langle x'|dxdx' \\
&\quad - \frac{1}{L^2} \int_{-L}^{L} \int_{-L}^{L} N_-^2(\beta)\Big(\frac{1}{2\pi\delta x_n^2}\Big)^{\frac{1}{2}} e^{-\frac{(x^2+x'^2)}{4\delta x_n^2}} \\
&\quad \times \sin\Big(\frac{\beta x}{\delta x_n}\Big)\sin\Big(\frac{\beta x'}{\delta x_n}\Big)|x\rangle\langle x'|dxdx'.
\end{aligned}$$

It is the role of each part of the operator X_{spatial} for the overlaps of nearly orthogonal states to be infinitesimally small and ideally zero. In the finite support approximation of $|\psi_+\rangle\langle\psi_+|$, the first term should not have any overlap with $|\psi_-\rangle\langle\psi_-|$. In the case of freely propagating nanoparticles,

this condition can be fulfilled by introducing two assumptions. In particular, in Eq. (4.5.4), the first assumption requires the integrals to be split into separate spatial regions, where a select subset of the regions is discarded, and the second assumption is that $x \approx x' \approx 0$. Similarly, for finite support approximation of $|\psi_-\rangle\langle\psi_-|$, the second term should not have any overlap with the $|\psi_+\rangle\langle\psi_+|$ term. This is fulfilled for $x \approx x' \approx \frac{\pi\delta x_n}{2\beta}$, once the integrals have again been split into separate selected regions and integrated over small variations in position.

Similarly for Y_n, the general spatial representation is

$$Y_{\text{spatial}} = \frac{1}{4L^2} \int_{-L}^{L} \int_{-L}^{L} N_{+i}^2(\beta) \Big(\frac{1}{2\pi\delta x_n^2}\Big)^{\frac{1}{2}} e^{-\frac{(x^2+x'^2)}{4\delta x_n^2}} f_1(x,x')|x\rangle\langle x'|dxdx'$$

$$(4.5.5)$$

$$-\frac{1}{4L^2} \int_{-L}^{L} \int_{-L}^{L} N_{-i}^2(\beta) \Big(\frac{1}{2\pi\delta x_n^2}\Big)^{\frac{1}{2}} e^{-\frac{(x^2+x'^2)}{4\delta x_n^2}} f_2(x,x')|x\rangle\langle x'|dxdx'$$

where

$$f_1(x,x') = 2\sin\Big(\frac{\beta x}{\delta x_n}\Big)\sin\Big(\frac{\beta x'}{\delta x_n}\Big) + 2\cos\Big(\frac{\beta x}{\delta x_n}\Big)\cos\Big(\frac{\beta x'}{\delta x_n}\Big) \qquad (4.5.6)$$
$$-2\sin\Big(\frac{\beta x}{\delta x_n}\Big)\cos\Big(\frac{\beta x'}{\delta x_n}\Big) - 2\cos\Big(\frac{\beta x}{\delta x_n}\Big)\sin\Big(\frac{\beta x'}{\delta x_n}\Big)$$
$$f_2(x,x') = 2\sin\Big(\frac{\beta x}{\delta x_n}\Big)\sin\Big(\frac{\beta x'}{\delta x_n}\Big) + 2\cos\Big(\frac{\beta x}{\delta x_n}\Big)\cos\Big(\frac{\beta x'}{\delta x_n}\Big) \qquad (4.5.7)$$
$$+2\sin\Big(\frac{\beta x}{\delta x_n}\Big)\cos\Big(\frac{\beta x'}{\delta x_n}\Big) + 2\cos\Big(\frac{\beta x}{\delta x_n}\Big)\sin\Big(\frac{\beta x'}{\delta x_n}\Big).$$

Due to the non-vanishing overlaps, it may not be possible to trivially approximate X_{spatial} and Y_{spatial} as diagonal projectors of the form $\int_{L1} dx|x\rangle\langle x| - \int_{L2} dx|x\rangle\langle x|$ onto two distinct spatial regions $L1$ and $L2$ as has been suggested in [139]. Using X_{spatial} as an example, I will discuss why and in how far the general case of the spatial qubit method for trapped nanoparticles differs from the approximate form of the spatial qubit operators assumed in previous works.

Motivated by the idea of associating the placement of two detectors at specific locations $L1$ and $L2$ in order to conduct an effective X_{spatial} measurement, the first and second terms in Eq. (4.5.4) are split into sums of integrations over separate spatial regions. Regions where the contributions from the cosine and sine are respectively small are discarded. This discarding in and of itself is already to be taken with a grain of salt and will have to be included in the probability of not detecting the position of the nanoparticle in either detector locations associated with X_{spatial} or Y_{spatial} measurements. In keeping with the approximation however,

$$\tilde{X}_{\text{spatial}} = \frac{1}{\epsilon^2} \int_{L1-\epsilon}^{L1+\epsilon} \int_{L1-\epsilon}^{L1+\epsilon} N_+^2(\beta) \Big(\frac{1}{2\pi\delta x_n^2}\Big)^{\frac{1}{2}} e^{-\frac{(x^2+x'^2)}{4\delta x_n^2}} \tag{4.5.8}$$

$$\times \cos\Big(\frac{\beta x}{\delta x_n}\Big)\cos\Big(\frac{\beta x'}{\delta x_n}\Big)|x\rangle\langle x'|dxdx'$$

$$- \frac{1}{\epsilon^2} \int_{L2-\epsilon}^{L2+\epsilon} \int_{L2-\epsilon}^{L2+\epsilon} N_-^2(\beta) \Big(\frac{1}{2\pi\delta x_n^2}\Big)^{\frac{1}{2}} e^{-\frac{(x^2+x'^2)}{4\delta x_n^2}}$$

$$\times \sin\Big(\frac{\beta x}{\delta x_n}\Big)\sin\Big(\frac{\beta x'}{\delta x_n}\Big)|x\rangle\langle x'|dxdx'.$$

where the locations are selected as $L_1 = 0$ and $L_2 = \frac{\pi\delta x_n}{2\beta}$. For overlaps which may be well approximated as delta functions in position, $\tilde{X}_{\text{spatial}}$ can be approximated by an operator diagonal in the position basis over narrow supports

$$\tilde{X}_{\text{spatial,d}} = \frac{1}{2\epsilon} \int_{-\epsilon}^{\epsilon} |x\rangle\langle x|dx \tag{4.5.9}$$

$$- \frac{1}{2\epsilon} \int_{\frac{\pi\delta x_n}{2\beta}-\epsilon}^{\frac{\pi\delta x_n}{2\beta}+\epsilon} |x\rangle\langle x|dx.$$

To illustrate why, I refer to the two terms comprising $\tilde{X}_{\text{spatial}}$ as $\tilde{X}_{\text{spatial}}^{(1)}$

and $\tilde{X}^{(2)}_{\text{spatial}}$, where

$$\tilde{X}^{(1)}_{\text{spatial}} = \frac{1}{\epsilon^2} \int_{L1-\epsilon}^{L1+\epsilon} \int_{L1-\epsilon}^{L1+\epsilon} N_+^2(\beta) \Big(\frac{1}{2\pi\delta x_n^2}\Big)^{\frac{1}{2}} e^{-\frac{(x^2+x'^2)}{4\delta x_n^2}} \tag{4.5.10}$$

$$\times \cos\Big(\frac{\beta x}{\delta x_n}\Big) \cos\Big(\frac{\beta x'}{\delta x_n}\Big) dx dx'$$

$$\tilde{X}^{(2)}_{\text{spatial}} = -\frac{1}{\epsilon^2} \int_{L2-\epsilon}^{L2+\epsilon} \int_{L2-\epsilon}^{L2+\epsilon} N_-^2(\beta) \Big(\frac{1}{2\pi\delta x_n^2}\Big)^{\frac{1}{2}} e^{-\frac{(x^2+x'^2)}{4\delta x_n^2}} \tag{4.5.11}$$

$$\times \sin\Big(\frac{\beta x}{\delta x_n}\Big) \sin\Big(\frac{\beta x'}{\delta x_n}\Big) dx dx'.$$

In the limit $\epsilon \to 0$, the function $\tilde{X}^{(1)}_{\text{spatial}}$ tends to 1 and the function $\tilde{X}^{(2)}_{\text{spatial}}$ tends to an expression proportional to the overlap $e^{-\frac{\pi^2}{8\beta^2}}$, which for large values of β may also tend to $\mathcal{O}(1)$. In this sense, as a rough approximation, it provides a justification for treating X_{spatial} as $\tilde{X}_{\text{spatial,d}}$. The spatial variation ϵ can of course also be set to realise a wider box, for example one with $\epsilon \to \frac{\pi\delta x_n}{8\beta}$.

In more general situations, the approximations from the previous paragraph will no longer apply. For small values of β, the exponential envelope in the second term $\tilde{X}^{(2)}_{\text{spatial}}$ will not approach 1 and the operator X_{spatial} will also not be diagonal. In order to show that any approximation of X_{spatial} works well, what is generally required is to show that

$$\langle\psi_+(\tau_2)|\tilde{X}^{(2)}_{\text{spatial}}|\psi_+(\tau_2)\rangle \approx 0 \tag{4.5.12}$$

and

$$\langle\psi_-(\tau_2)|\tilde{X}^{(1)}_{\text{spatial}}|\psi_-(\tau_2)\rangle \approx 0. \tag{4.5.13}$$

Similar arguments and position diagonal approximations for Y_{spatial} can be made with its first part approximated by a narrow integral near $L1 = \frac{\pi\delta x_n}{4\beta}$ and $L2 = -\frac{\pi\delta x_n}{4\beta}$. In this case,

$$\langle\psi_{+i}(\tau_2)|\tilde{Y}^{(2)}_{\text{spatial}}|\psi_{+i}(\tau_2)\rangle \approx 0 \tag{4.5.14}$$

and

$$\langle\psi_{-i}(\tau_2)|\tilde{Y}_{\text{spatial}}^{(1)}|\psi_{-i}(\tau_2)\rangle \approx 0. \qquad (4.5.15)$$

It will be up to future works aiming to treat nanoparticles as spatial qubits to prove both of these requirements on an individual case by case basis. The specific realisations of X_{spatial} depend on a number of experimental factors, such as the types of detectors (e.g. the characteristic of the available optical fields in case of optical detection) and the geometry of the experiment.

4.6 Summary

A specific protocol for creating superpositions of nanoparticles through interactions with ions via the Coulomb force has been investigated. I find that superpositions on the scale of $\Delta x \sim 10$ nm should be readily achievable in settings where both particles are confined in separate ion traps. Upon repetition of the experimental protocol, the nanoparticle's fringes in position can be used to evidence the superposition, provided the position can be measured to better than the standard quantum limit and the principal mechanisms of decoherence are sufficiently suppressed. I further introduce a method of entanglement verification, which requires the placement of detectors at specific locations in order to map select regions of the spatial fringes of the nanoparticle to measurements in complementary bases that correspond to the eigenbases of Pauli operators. I outline some of the difficulties in constructing such types of approximate spatial qubit operators and highlight cases in which the approximation may not hold, since near orthogonality of the measurement eigenstates cannot be ensured.

A future direction of research will be to analyse the possibility of squeez-

ing the nanoparticle's quantum state after the atom has been measured, which may result in requiring less precise fringe measurements. Another area of investigation will consist of devising a rigorous theoretical framework in order to test the validity of the spatial qubit method for nanoparticle experiments.

Chapter 5

Conclusion

This thesis provides contributions to the field of quantum sensing, in particular its possible applications to the detection of particles. In Chapter 2, I have explored how quantum superpositions of massive objects may be used to sense low energy neutrinos produced by a reactor source via their momentum transfer to the superposed object. Assuming an interferometic matter-wave sensing scheme, the momentum transfer due to the weak coherent neutral-current scattering of neutrinos from the nuclei in the target is reflected in the accumulation of a relative phase between the components of the superposition. A total detector mass larger than the current demonstrated record holder [44], or an array of several slightly lighter masses [141], is needed in order to obtain significant phase signatures. While the required minimum detector mass presents an experimental challenge, the use of quantum sensors for fundamental physics research is in general an upcoming field of research that will doubtlessly gain even more traction in the coming years. This is the case because most large-scale particle physics detectors lack the ability to resolve low momentum transfer interactions. In future work, a more complete picture of the actual experimental signatures may be obtained by including other types of possible neutrino interactions on the one hand and resorting to other mathematical models to account for high-energy particle scattering on the other.

In principle, large-mass interferometers may also be used for searches of select dark matter candidates. The detection of particulate winds, referring to a directional stream of particles, may present an especially interesting application for interferometric matter-wave sensors. In the future, superpositions of large masses may also find wider commercial application, for example as sensors for precision measurements of gas particles or leakages.

The sensing of directional particle sources through quantum superpositions has been treated in more generality in Chapter 3. There, I have shown how the size of the superposition in the sensing object's motional states may be optimally chosen in order to coherently sense directional environments. A concrete example for single photon detection has been presented. Calculations with other incident particles are in the works.

In order to complete the picture, I have discussed in Chapter 4 a promising scheme for the experimental realisation of the large mass superpositions required for the detection of elusive and scarcely interacting particles. The chapter provides the blueprint for the aim of exploiting large Coulomb force couplings of charged trapped nanoparticles and ions. The ion, which is more easily controlled, is prepared in a motional superposition state. Entanglement of the ion-nanoparticle system is generated through the interaction and represents the underlying mechanism for creating a superposition in the nanoparticle's motional states. This can be regarded as a *remote* version of Stern-Gerlach interferometry, with the spin (here replaced by atomic internal levels, possibly hyperfine levels) outside the nanoparticle. The obvious advantage is that the internal levels can be more easily addressed via lasers, which may not penetrate the nanoparticle well enough to address an embedded single atomic qubit. I further describe how the superposition of the nanoparticle can be evidenced through the presence of interference fringes in position and present the idea of treating the nanoparticle as a spatial qubit, where I

emphasize the technical difficulties of constructing spatial Pauli operators to be used for witnessing the entanglement. A future line of investigation will be to extend the notion of a spatial qubit encoding for the nanoparticle to qudits. This may enable one to avoid the inefficiency of the experiment with spatial qubits, where a large number of outcomes, where the nanoparticle is not detected close to either of the detection regions is discarded. Qudits may also have a natural application in grating based nanoparticle interferometry [46]. Another area of research is motivated by the recently experimentally demonstrated dipole-dipole interaction between optically levitated nanoparticles [142] and how this observed interaction may be utilized to generate large mass superpositions in neutral atom-nanoparticle systems. Further improvements of the presented scheme may be achieved by looking at the influence of squeezing the nanoparticle state. Of course, one of the most important questions is whether nanoparticle based quantum sensors will really be useful in comparison to extant sensors, both classical, and quantum such as those using atom interferometry or quantum light. These questions should become clearer in the future, as full analysis of these setups in the presence of possible noise sources are investigated.

Bibliography

[1] De Broglie, Louis, "Recherches sur la théorie des Quanta", Ann. Phys. **10**, 22–128 (1925) (cit. on p. 25).

[2] C. Davisson and L. H. Germer, "Diffraction of Electrons by a Crystal of Nickel", Phys. Rev. **30**, 705–740 (1927) (cit. on p. 25).

[3] L. Marton, J. A. Simpson, and J. A. Suddeth, "Electron Beam Interferometer", Physical Review **90**, Publisher: American Physical Society, 490–491 (1953) (cit. on p. 25).

[4] C. Jönsson, "Elektroneninterferenzen an mehreren künstlich hergestellten Feinspalten", Zeitschrift für Physik **161**, 454–474 (1961) (cit. on pp. 25, 38).

[5] J Baudon, R Mathevet, and J Robert, "Atomic interferometry", Journal of Physics B: Atomic, Molecular and Optical Physics **32**, R173 (1999) (cit. on p. 25).

[6] M. D. Lachmann, H. Ahlers, D. Becker, A. N. Dinkelaker, J. Grosse, O. Hellmig, H. Müntinga, V. Schkolnik, S. T. Seidel, T. Wendrich, A. Wenzlawski, B. Carrick, N. Gaaloul, D. Lüdtke, C. Braxmaier, W. Ertmer, M. Krutzik, C. Lämmerzahl, A. Peters, W. P. Schleich, K. Sengstock, A. Wicht, P. Windpassinger, and E. M. Rasel, "Ultracold atom interferometry in space", Nature Communications **12**, 1317 (2021) (cit. on p. 25).

[7] A. D. Cronin, J. Schmiedmayer, and D. E. Pritchard, "Optics and interferometry with atoms and molecules", Rev. Mod. Phys. **81**, 1051–1129 (2009) (cit. on pp. 25, 34).

[8]   K. Hornberger, S. Gerlich, P. Haslinger, S. Nimmrichter, and M. Arndt, "Colloquium: Quantum interference of clusters and molecules", Rev. Mod. Phys. **84**, Publisher: American Physical Society, 157–173 (2012) (cit. on p. 25).

[9]   S. Pedalino, T. de Sousa, Y. Y. Fein, S. Gerlich, and M. Arndt, "Exploring metal nanoparticles for matter-wave interferometry", Phys. Rev. A **106**, Publisher: American Physical Society, 023312 (2022) (cit. on p. 25).

[10] R. J. Marshman, A. Mazumdar, G. W. Morley, P. F. Barker, S. Hoekstra, and S. Bose, "Mesoscopic interference for metric and curvature & gravitational wave detection", New Journal of Physics **22**, Publisher: IOP Publishing, 083012 (2020) (cit. on pp. 26, 59, 78, 81, 83, 84, 93).

[11] B. Canuel, A. Bertoldi, L. Amand, E. Pozzo Di Borgo, T. Chantrait, C. Danquigny, M. Dovale Alvarez, B. Fang, A. Freise, R. Geiger, J. Gillot, S. Henry, J. Hinderer, D. Holleville, J. Junca, G. Lefevre, M. Merzougui, N. Mielec, T. Monfret, S. Pelisson, M. Prevedelli, S. Reynaud, I. Riou, Y. Rogister, S. Rosat, E. Cormier, A. Landragin, W. Chaibi, S. Gaffet, and P. Bouyer, "Exploring gravity with the MIGA large scale atom interferometer", en, Scientific Reports **8**, 14064 (2018) (cit. on p. 26).

[12] D. Carney, K. G. Leach, and D. C. Moore, "Searches for Massive Neutrinos with Mechanical Quantum Sensors", PRX Quantum **4**, Publisher: American Physical Society, 010315 (2023) (cit. on pp. 26, 54).

[13] C. J. Riedel, "Direct detection of classically undetectable dark matter through quantum decoherence", Phys. Rev. D **88**, Publisher: American Physical Society, 116005 (2013) (cit. on pp. 26, 39, 59, 93, 94).

[14] C. J. Riedel, "Decoherence from classically undetectable sources:
      Standard quantum limit for diffusion", Phys. Rev. A **92**, Publisher:
      American Physical Society, 010101 (2015) (cit. on pp. 26, 39, 59).

[15] G. Wolfowicz and J. J. Morton, "Pulse Techniques for Quantum
      Information Processing", en, in *eMagRes*, edited by R. K. Harris
      and R. L. Wasylishen (John Wiley & Sons, Ltd, Chichester, UK,
      Dec. 2016), pp. 1515–1528 (cit. on p. 26).

[16] "Atomic quantum information carriers", in *Introduction to Optical
      Quantum Information Processing*, edited by B. W. Lovett and P.
      Kok (Cambridge University Press, Cambridge, 2010), pp. 210–252
      (cit. on p. 27).

[17] D. Wineland, C. Monroe, W. Itano, D. Leibfried, B. King, and
      D. Meekhof, "Experimental issues in coherent quantum-state ma-
      nipulation of trapped atomic ions", Journal of Research of the
      National Institute of Standards and Technology **103**, 259 (1998)
      (cit. on p. 30).

[18] K. G. Johnson, J. D. Wong-Campos, B. Neyenhuis, J. Mizrahi,
      and C. Monroe, "Ultrafast creation of large Schrödinger cat states
      of an atom", Nature Communications **8**, 697 (2017) (cit. on pp. 34,
      119).

[19] S. Chu, "Nobel Lecture: The manipulation of neutral particles",
      Rev. Mod. Phys. **70**, Publisher: American Physical Society, 685–
      706 (1998) (cit. on p. 34).

[20] R. H. Parker, C. Yu, W. Zhong, B. Estey, and H. Müller, "Mea-
      surement of the fine-structure constant as a test of the Standard
      Model", Science **360**, Publisher: American Association for the Ad-
      vancement of Science, 191–195 (2018) (cit. on p. 34).

[21] G. Lamporesi, A. Bertoldi, L. Cacciapuoti, M. Prevedelli, and
      G. M. Tino, "Determination of the Newtonian Gravitational Con-

stant Using Atom Interferometry", Phys. Rev. Lett. **100**, Publisher: American Physical Society, 050801 (2008) (cit. on p. 34).

[22] G. Rosi, F. Sorrentino, L. Cacciapuoti, M. Prevedelli, and G. M. Tino, "Precision measurement of the Newtonian gravitational constant using cold atoms", Nature **510**, 518–521 (2014) (cit. on p. 34).

[23] M. J. Snadden, J. M. McGuirk, P. Bouyer, K. G. Haritos, and M. A. Kasevich, "Measurement of the Earth's Gravity Gradient with an Atom Interferometer-Based Gravity Gradiometer", Phys. Rev. Lett. **81**, Publisher: American Physical Society, 971–974 (1998) (cit. on p. 34).

[24] G. Rosi, L. Cacciapuoti, F. Sorrentino, M. Menchetti, M. Prevedelli, and G. M. Tino, "Measurement of the Gravity-Field Curvature by Atom Interferometry", Phys. Rev. Lett. **114**, Publisher: American Physical Society, 013001 (2015) (cit. on p. 34).

[25] A. Peters, K. Y. Chung, and S. Chu, "Measurement of gravitational acceleration by dropping atoms", Nature **400**, 849–852 (1999) (cit. on p. 34).

[26] R. Kaiser, C. Westbrook, and F. David, eds., *Coherent atomic matter waves*, en, Vol. 72, Les Houches - Ecole d'Ete de Physique Theorique (Springer Berlin Heidelberg, Berlin, Heidelberg, 2001) (cit. on p. 34).

[27] O. Carnal and J. Mlynek, "Young's double-slit experiment with atoms: A simple atom interferometer", Physical Review Letters **66**, Publisher: American Physical Society, 2689–2692 (1991) (cit. on pp. 34, 38).

[28] D. W. Keith, C. R. Ekstrom, Q. A. Turchette, and D. E. Pritchard, "An interferometer for atoms", Physical Review Letters **66**, Publisher: American Physical Society, 2693–2696 (1991) (cit. on p. 34).

[29] F. Riehle, T. Kisters, A. Witte, J. Helmcke, and C. J. Bordé, "Optical Ramsey spectroscopy in a rotating frame: Sagnac effect in a matter-wave interferometer", Physical Review Letters **67**, Publisher: American Physical Society, 177–180 (1991) (cit. on p. 35).

[30] M. Kasevich and S. Chu, "Atomic interferometry using stimulated Raman transitions", Physical Review Letters **67**, Publisher: American Physical Society, 181–184 (1991) (cit. on p. 35).

[31] A. Bonnin, N. Zahzam, Y. Bidel, and A. Bresson, "Simultaneous dual-species matter-wave accelerometer", Phys. Rev. A **88**, Publisher: American Physical Society, 043615 (2013) (cit. on p. 35).

[32] T. L. Gustavson, P. Bouyer, and M. A. Kasevich, "Precision Rotation Measurements with an Atom Interferometer Gyroscope", Phys. Rev. Lett. **78**, Publisher: American Physical Society, 2046–2049 (1997) (cit. on p. 35).

[33] P. A. Altin, M. T. Johnsson, V. Negnevitsky, G. R. Dennis, R. P. Anderson, J. E. Debs, S. S. Szigeti, K. S. Hardman, S. Bennetts, G. D. McDonald, L. D. Turner, J. D. Close, and N. P. Robins, "Precision atomic gravimeter based on Bragg diffraction", New Journal of Physics **15**, Publisher: IOP Publishing, 023009 (2013) (cit. on p. 35).

[34] K. Bongs, M. Holynski, J. Vovrosh, P. Bouyer, G. Condon, E. Rasel, C. Schubert, W. P. Schleich, and A. Roura, "Taking atom interferometric quantum sensors from the laboratory to real-world applications", Nature Reviews Physics **1**, 731–739 (2019) (cit. on p. 35).

[35] C. Foot, *Atomic Physics*, Oxford Master Series in Physics (OUP Oxford, 2005) (cit. on p. 35).

[36]   S. Machluf, Y. Japha, and R. Folman, "Coherent Stern–Gerlach momentum splitting on an atom chip", Nature Communications **4**, 2424 (2013) (cit. on p. 36).

[37]   O. Amit, Y. Margalit, O. Dobkowski, Z. Zhou, Y. Japha, M. Zimmermann, M. A. Efremov, F. A. Narducci, E. M. Rasel, W. P. Schleich, and R. Folman, "T^3 Stern-Gerlach Matter-Wave Interferometer", Phys. Rev. Lett. **123**, Publisher: American Physical Society, 083601 (2019) (cit. on p. 36).

[38]   Y. Margalit, O. Dobkowski, Z. Zhou, O. Amit, Y. Japha, S. Moukouri, D. Rohrlich, A. Mazumdar, S. Bose, C. Henkel, and others, "Realization of a complete Stern-Gerlach interferometer: Toward a test of quantum gravity", Science advances **7**, Publisher: American Association for the Advancement of Science, eabg2879 (2021) (cit. on pp. 36, 58, 61).

[39]   M. Keil, S. Machluf, Y. Margalit, Z. Zhou, O. Amit, O. Dobkowski, Y. Japha, S. Moukouri, D. Rohrlich, Z. Binstock, Y. Bar-Haim, M. Givon, D. Groswasser, Y. Meir, and R. Folman, "Stern-Gerlach Interferometry with the Atom Chip", in *Molecular Beams in Physics and Chemistry: From Otto Stern's Pioneering Exploits to Present-Day Feats*, edited by B. Friedrich and H. Schmidt-Böcking (Springer International Publishing, Cham, 2021), pp. 263–301 (cit. on pp. 37, 61).

[40]   A. Tonomura, J. Endo, T. Matsuda, T. Kawasaki, and H. Ezawa, "Demonstration of single-electron buildup of an interference pattern", American Journal of Physics **57**, 117–120 (1989) (cit. on p. 38).

[41]   H. Rauch, W. Treimer, and U. Bonse, "Test of a single crystal neutron interferometer", Physics Letters A **47**, 369–371 (1974) (cit. on p. 38).

[42] M. Arndt, O. Nairz, J. Vos-Andreae, C. Keller, G. van der Zouw, and A. Zeilinger, "Wave–particle duality of C60 molecules", Nature **401**, 680–682 (1999) (cit. on p. 38).

[43] O. Nairz, B. Brezger, M. Arndt, and A. Zeilinger, "Diffraction of Complex Molecules by Structures Made of Light", Phys. Rev. Lett. **87**, Publisher: American Physical Society, 160401 (2001) (cit. on p. 38).

[44] Y. Y. Fein, P. Geyer, P. Zwick, F. Kiałka, S. Pedalino, M. Mayor, S. Gerlich, and M. Arndt, "Quantum superposition of molecules beyond 25 kDa", Nature Physics **15**, 1242–1245 (2019) (cit. on pp. 38, 59, 128).

[45] C. Gonzalez-Ballestero, M. Aspelmeyer, L. Novotny, R. Quidant, and O. Romero-Isart, "Levitodynamics: Levitation and control of microscopic objects in vacuum", Science **374**, eabg3027 (2021) (cit. on p. 38).

[46] J. Bateman, S. Nimmrichter, K. Hornberger, and H. Ulbricht, "Near-field interferometry of a free-falling nanoparticle from a point-like source", Nature Communications **5**, 4788 (2014) (cit. on pp. 39, 58, 130).

[47] C. Wan, M. Scala, G. W. Morley, A. A. Rahman, H. Ulbricht, J. Bateman, P. F. Barker, S. Bose, and M. S. Kim, "Free Nano-Object Ramsey Interferometry for Large Quantum Superpositions", Phys. Rev. Lett. **117**, Publisher: American Physical Society, 143003 (2016) (cit. on pp. 39, 58, 61, 93).

[48] S. Bose, A. Mazumdar, G. W. Morley, H. Ulbricht, M. Toroš, M. Paternostro, A. A. Geraci, P. F. Barker, M. S. Kim, and G. Milburn, "Spin Entanglement Witness for Quantum Gravity", Phys. Rev. Lett. **119**, 240401 (2017) (cit. on pp. 39, 59, 78, 84, 93, 100).

[49]   C. Marletto and V. Vedral, "Gravitationally Induced Entangle-
       ment between Two Massive Particles is Sufficient Evidence of Quan-
       tum Effects in Gravity", Phys. Rev. Lett. **119**, 240402 (2017) (cit.
       on pp. 39, 59).

[50]   R. Kaltenbaek, M. Arndt, M. Aspelmeyer, P. F. Barker, A. Bassi,
       J. Bateman, A. Belenchia, J. Bergé, C. Braxmaier, S. Bose, B.
       Christophe, G. D. Cole, C. Curceanu, A. Datta, M. Debiossac, U.
       Delić, L. Diósi, A. A. Geraci, S. Gerlich, C. Guerlin, G. Hechen-
       blaikner, A. Heidmann, S. Herrmann, K. Hornberger, U. Johann,
       N. Kiesel, C. Lämmerzahl, T. W. LeBrun, G. J. Milburn, J. Millen,
       M. Mohageg, D. C. Moore, G. W. Morley, S. Nimmrichter, L.
       Novotny, D. K. L. Oi, M. Paternostro, C. J. Riedel, M. Rodrigues,
       L. Rondin, A. Roura, W. P. Schleich, T. Schuldt, B. A. Stick-
       ler, H. Ulbricht, C. Vogt, and L. Wörner, "Research campaign:
       Macroscopic quantum resonators (MAQRO)", Quantum Science
       and Technology **8**, Publisher: IOP Publishing, 014006 (2023) (cit.
       on p. 39).

[51]   C. J. Riedel and I. Yavin, "Decoherence as a way to measure ex-
       tremely soft collisions with dark matter", Phys. Rev. D **96**, Pub-
       lisher: American Physical Society, 023007 (2017) (cit. on pp. 39,
       59).

[52]   W. Pauli, *Pauli letter collection: letter to Lise Meitner*, 1930 (cit.
       on p. 39).

[53]   F. Deppisch, I. o. P. G. Britain), and M. C. Publishers, *A Modern
       Introduction to Neutrino Physics*, IOP concise physics (Morgan &
       Claypool Publishers, 2019) (cit. on pp. 40, 41).

[54]   E. Fermi, "Versuch einer Theorie der -Strahlen. I", Zeitschrift für
       Physik **88**, 161–177 (1934) (cit. on p. 40).

[55] F. Reines and C. L. Cowan, "Detection of the Free Neutrino", Phys. Rev. **92**, Publisher: American Physical Society, 830–831 (1953) (cit. on p. 40).

[56] S. L. Glashow, "Partial-symmetries of weak interactions", Nuclear Physics **22**, 579–588 (1961) (cit. on p. 41).

[57] S. Weinberg, "A Model of Leptons", Phys. Rev. Lett. **19**, Publisher: American Physical Society, 1264–1266 (1967) (cit. on p. 41).

[58] S. L. Glashow, J. Iliopoulos, and L. Maiani, "Weak Interactions with Lepton-Hadron Symmetry", Phys. Rev. D **2**, Publisher: American Physical Society, 1285–1292 (1970) (cit. on p. 41).

[59] M. Srednicki, *Quantum Field Theory* (Cambridge University Press, Cambridge, 2007) (cit. on pp. 41, 42, 48).

[60] K. Zuber, *Neutrino Physics*, en, 3rd ed. (CRC Press, Boca Raton, May 2020) (cit. on pp. 44, 50).

[61] P. Vogel, L. Wen, and C. Zhang, "Neutrino oscillation studies with reactors", Nature Communications **6**, 6935 (2015) (cit. on p. 48).

[62] J. A. Formaggio and G. P. Zeller, "From eV to EeV: Neutrino cross sections across energy scales", Reviews of Modern Physics **84**, 1307–1341 (2012) (cit. on p. 49).

[63] M. Cadeddu, F. Dordei, and C. Giunti, "A view of coherent elastic neutrino-nucleus scattering", Europhysics Letters **143**, Publisher: EDP Sciences, IOP Publishing and Società Italiana di Fisica, 34001 (2023) (cit. on p. 51).

[64] A. BELLERIVE, "REVIEW OF SOLAR NEUTRINO EXPERIMENTS", International Journal of Modern Physics A **19**, 1167–1179 (2004) (cit. on p. 52).

[65] G. Bellini, A. Ianni, L. Ludhova, F. Mantovani, and W. McDonough, "Geo-neutrinos", Progress in Particle and Nuclear Physics **73**, 1–34 (2013) (cit. on p. 52).

[66] D. H. Hartmann and S. E. Woosley, "The cosmic supernova neutrino background", Astroparticle Physics **7**, 137–146 (1997) (cit. on p. 52).

[67] C. Lunardini, "Theory and phenomenology of supernova neutrinos", AIP Conference Proceedings **1666**, 070001 (2015) (cit. on p. 52).

[68] M. Ahlers, K. Helbing, and C. Pérez de los Heros, "Probing particle physics with IceCube", The European Physical Journal C **78**, 924 (2018) (cit. on p. 52).

[69] Y. Fukuda, T. Hayakawa, E. Ichihara, K. Inoue, K. Ishihara, H. Ishino, Y. Itow, T. Kajita, J. Kameda, S. Kasuga, and others, "Evidence for Oscillation of Atmospheric Neutrinos", Physical Review Letters **81**, 1562–1567 (1998) (cit. on pp. 53, 57).

[70] A. d. Gouvêa and I. Martinez-Soler, "Reactor antineutrino oscillations at Super-Kamiokande", Physics Letters B **809**, 135751 (2020) (cit. on p. 53).

[71] H. Abele, G. Angloher, A. Bento, L. Canonica, F. Cappella, L. Cardani, N. Casali, R. Cerulli, A. Chalil, A. Chebboubi, I. Colantoni, J.-P. Crocombette, A. Cruciani, G. Del Castello, M. del Gallo Roccagiovine, D. Desforge, A. Doblhammer, E. Dumonteil, S. Dorer, A. Erhart, A. Fuss, M. Friedl, A. Garai, V. M. Ghete, A. Giuliani, C. Goupy, F. Gunsing, D. Hauff, F. Jeanneau, E. Jericha, M. Kaznacheeva, A. Kinast, H. Kluck, A. Langenkämper, T. Lasserre, A. Letourneau, D. Lhuillier, O. Litaize, M. Mancuso, P. de Marcillac, S. Marnieros, T. Materna, B. Mauri, A. Mazzolari, E. Mazzucato, H. Neyrial, C. Nones, L. Oberauer, T. Ortmann, A. Ouzriat, L. Pattavina, L. Peters, F. Petricca, D. V. Poda, W. Potzel, F. Pröbst, F. Reindl, R. Rogly, M. Romagnoni, J. Rothe, N. Schermer, J. Schieck, S. Schönert, C. Schwertner, L. Scola, O. Serot, G. Soum-Sidikov, L. Stodolsky, R. Strauss, M. Tamisari,

L. Thulliez, C. Tomei, M. Vignati, M. Vivier, V. Wagner, and A. Wex, "Observation of a Nuclear Recoil Peak at the 100 eV Scale Induced by Neutron Capture", Phys. Rev. Lett. **130**, Publisher: American Physical Society, 211802 (2023) (cit. on p. 53).

[72] E. Kilian, M. Toroš, F. F. Deppisch, R. Saakyan, and S. Bose, "Requirements on quantum superpositions of macro-objects for sensing neutrinos", Phys. Rev. Res. **5**, 023012 (2023) (cit. on pp. 56, 93).

[73] F. Reines and C. L. Cowan Jr., "The Neutrino", Nature **178**, 446–449 (1956) (cit. on p. 57).

[74] The KATRIN Collaboration, M. Aker, A. Beglarian, J. Behrens, A. Berlev, U. Besserer, B. Bieringer, F. Block, S. Bobien, M. Böttcher, B. Bornschein, and others, "Direct neutrino-mass measurement with sub-electronvolt sensitivity", Nature Physics **18**, 160–166 (2022) (cit. on p. 57).

[75] S. Bose, K. Jacobs, and P. L. Knight, "Scheme to probe the decoherence of a macroscopic object", Physical Review A **59**, Publisher: APS, 3204 (1999) (cit. on pp. 58, 84).

[76] A. D. Armour, M. P. Blencowe, and K. C. Schwab, "Entanglement and decoherence of a micromechanical resonator via coupling to a Cooper-pair box", Physical Review Letters **88**, Publisher: APS, 148301 (2002) (cit. on p. 58).

[77] W. Marshall, C. Simon, R. Penrose, and D. Bouwmeester, "Towards quantum superpositions of a mirror", Physical Review Letters **91**, Publisher: APS, 130401 (2003) (cit. on p. 58).

[78] O. Romero-Isart, "Quantum superposition of massive objects and collapse models", Phys. Rev. A **84**, Publisher: American Physical Society, 052121 (2011) (cit. on pp. 58, 81).

[79] O. Romero-Isart, A. C. Pflanzer, F. Blaser, R. Kaltenbaek, N. Kiesel, M. Aspelmeyer, and J. I. Cirac, "Large quantum superpositions and interference of massive nanometer-sized objects", Physical Review Letters **107**, Publisher: APS, 020405 (2011) (cit. on p. 58).

[80] M. Scala, M. S. Kim, G. W. Morley, P. F. Barker, and S. Bose, "Matter-Wave Interferometry of a Levitated Thermal Nano-Oscillator Induced and Probed by a Spin", Physical Review Letters **111**, 180403 (2013) (cit. on pp. 58, 61).

[81] Z. Q. Yin, T. Li, X. Zhang, and L. M. Duan, "Large quantum superpositions of a levitated nanodiamond through spin-optomechanical coupling", Physical Review A **88**, Publisher: APS, 033614 (2013) (cit. on pp. 58, 61).

[82] J. S. Pedernales, G. W. Morley, and M. B. Plenio, "Motional dynamical decoupling for interferometry with macroscopic particles", Physical Review Letters **125**, Publisher: APS, 023602 (2020) (cit. on pp. 58, 61).

[83] B. Wood, S Bose, and G. Morley, "Spin dynamical decoupling for generating macroscopic superpositions of a free-falling nanodiamond", Physical Review A **105**, Publisher: APS, 012824 (2022) (cit. on pp. 58, 61).

[84] R. J. Marshman, A. Mazumdar, R. Folman, and S. Bose, "Constructing nano-object quantum superpositions with a Stern-Gerlach interferometer", Phys. Rev. Res. **4**, 023087 (2022) (cit. on pp. 58, 61, 100).

[85] L. Magrini, P. Rosenzweig, C. Bach, A. Deutschmann-Olek, S. G. Hofer, S. Hong, N. Kiesel, A. Kugi, and M. Aspelmeyer, "Real-time optimal quantum control of mechanical motion at room temperature", Nature **595**, 373–377 (2021) (cit. on p. 59).

[86] U. Delić, M. Reisenbauer, K. Dare, D. Grass, V. Vuletić, N. Kiesel, and M. Aspelmeyer, "Cooling of a levitated nanoparticle to the motional quantum ground state", Science **367**, 892 (2020) (cit. on p. 59).

[87] F. Tebbenjohanns, M. Frimmer, V. Jain, D. Windey, and L. Novotny, "Motional sideband asymmetry of a nanoparticle optically levitated in free space", Physical Review Letters **124**, Publisher: APS, 013603 (2020) (cit. on p. 59).

[88] F. Tebbenjohanns, M. L. Mattana, M. Rossi, M. Frimmer, and L. Novotny, "Quantum control of a nanoparticle optically levitated in cryogenic free space", Nature **595**, 378–382 (2021) (cit. on p. 59).

[89] C. Whittle, E. D. Hall, S. Dwyer, N. Mavalvala, V. Sudhir, R Abbott, A Ananyeva, C Austin, L Barsotti, J Betzwieser, and others, "Approaching the motional ground state of a 10-kg object", Science **372**, Publisher: American Association for the Advancement of Science, 1333–1336 (2021) (cit. on pp. 59, 86).

[90] M. Rademacher, J. Millen, and Y. L. Li, "Quantum sensing with nanoparticles for gravimetry: when bigger is better", Advanced Optical Technologies **9**, 227–239 (2020) (cit. on p. 59).

[91] R. J. Marshman, A. Mazumdar, and S. Bose, "Locality and entanglement in table-top testing of the quantum nature of linearized gravity", Physical Review A **101**, Publisher: APS, 052110 (2020) (cit. on p. 59).

[92] S. Bose, A. Mazumdar, M. Schut, and M. Toroš, "Mechanism for the quantum natured gravitons to entangle masses", Phys. Rev. D **105**, 106028 (2022) (cit. on p. 59).

[93] P. F. Barker, S. Bose, R. J. Marshman, and A. Mazumdar, "Entanglement based tomography to probe new macroscopic forces", Phys. Rev. D **106**, L041901 (2022) (cit. on p. 59).

[94] S. Bose, A. Mazumdar, M. Schut, and M. Toroš, "Entanglement Witness for the Weak Equivalence Principle", Entropy **25**, 10 . 3390/e25030448 (2023) (cit. on p. 59).

[95] F. Monteiro, G. Afek, D. Carney, G. Krnjaic, J. Wang, and D. C. Moore, "Search for composite dark matter with optically levitated sensors", Physical Review Letters **125**, Publisher: APS, 181102 (2020) (cit. on p. 59).

[96] G. Afek, D. Carney, and D. C. Moore, "Coherent Scattering of Low Mass Dark Matter from Optically Trapped Sensors", Phys. Rev. Lett. **128**, Publisher: American Physical Society, 101301 (2022) (cit. on pp. 59, 93).

[97] J. Bateman, I. McHardy, A. Merle, T. R. Morris, and H. Ulbricht, "On the Existence of Low-Mass Dark Matter and its Direct Detection", Scientific Reports **5**, 8058 (2015) (cit. on p. 59).

[98] D. Z. Freedman, "Coherent effects of a weak neutral current", Physical Review D **9**, 1389–1392 (1974) (cit. on p. 60).

[99] D. Akimov, J. B. Albert, P. An, C. Awe, P. S. Barbeau, B. Becker, V. Belov, A. Brown, A. Bolozdynya, B. Cabrera-Palmer, and others, "Observation of coherent elastic neutrino-nucleus scattering", Science **357**, 1123 (2017) (cit. on p. 60).

[100] V. Domcke and M. Spinrath, "Detection prospects for the Cosmic Neutrino Background using laser interferometers", Journal of Cosmology and Astroparticle Physics **2017**, 055–055 (2017) (cit. on p. 60).

[101] R. Strauss, J. Rothe, G. Angloher, A. Bento, A. Gütlein, D. Hauff, H. Kluck, M. Mancuso, L. Oberauer, F. Petricca, F. Pröbst, J. Schieck, S. Schönert, W. Seidel, and L. Stodolsky, "The -cleus experiment: a gram-scale fiducial-volume cryogenic detector for

the first detection of coherent neutrino–nucleus scattering", The European Physical Journal C **77**, 506 (2017) (cit. on p. 60).

[102] N. Bar-Gill, L. M. Pham, A. Jarmola, D. Budker, and R. L. Walsworth, "Solid-state electronic spin coherence time approaching one second", Nature communications **4**, Publisher: Nature Publishing Group, 1–6 (2013) (cit. on pp. 61, 78).

[103] M. Niethammer, M. Widmann, T. Rendler, N. Morioka, Y.-C. Chen, R. Stöhr, J. U. Hassan, S. Onoda, T. Ohshima, S.-Y. Lee, and others, "Coherent electrical readout of defect spins in silicon carbide by photo-ionization at ambient conditions", Nature communications **10**, Publisher: Nature Publishing Group, 1–8 (2019) (cit. on p. 61).

[104] A. M. Jakob, S. G. Robson, V. Schmitt, V. Mourik, M. Posselt, D. Spemann, B. C. Johnson, H. R. Firgau, E. Mayes, J. C. McCallum, and others, "Deterministic Shallow Dopant Implantation in Silicon with Detection Confidence Upper-Bound to 99.85% by Ion–Solid Interactions", Advanced Materials **34**, Publisher: Wiley Online Library, 2103235 (2022) (cit. on p. 61).

[105] M. Lindner, W. Rodejohann, and X.-J. Xu, "Coherent neutrino-nucleus scattering and new neutrino interactions", en, Journal of High Energy Physics **2017**, 97 (2017) (cit. on p. 65).

[106] K. Scholberg, "Coherent elastic neutrino-nucleus scattering", Journal of Physics: Conference Series **606**, 012010 (2015) (cit. on p. 66).

[107] M. Abdullah, H. Abele, D. Akimov, G. Angloher, D. Aristizabal-Sierra, C. Augier, A. B. Balantekin, L. Balogh, P. S. Barbeau, L. Baudis, A. L. Baxter, C. Beaufort, G. Beaulieu, V. Belov, A. Bento, L. Berge, I. A. Bernardi, J. Billard, A. Bolozdynya, A. Bonhomme, G. Bres, J.-. L. Bret, A. Broniatowski, A. Brossard, C. Buck, M. Cadeddu, M. Calvo, L. Canonica, F. Cappella, L.

Cardani, N. Casali, A. Cazes, R. Cerulli, D. Chaize, C. Chang, M. Chapellier, L. Chaplinsky, G. Chemin, R. Chen, I. Colantoni, J. Colas, P. Coloma, E. C. Corcoran, S. Crawford, A. Cruciani, A. D. Fard, M. De Jesus, P. de Marcillac, V. De Romeri, G. del Castello, M. del GalloRoccagiovine, D. Delicato, M. Demarteau, Y. Deng, J. B. Dent, P. B. Denton, K. Dering, A. Doblhammer, F. Dordei, S. Dorer, L. Dumoulin, D. Dunford, B. Dutta, A. Erhart, O. Exshaw, S. Ferriol, E. Figueroa-Feliciano, J. B. Filippini, L. J. Flores, J. A. Formaggio, M. Friedl, S. Fuard, F. Gao, A. Garai, E. A. Garces, J. Gascon, J. Gehrlein, G. Gerbier, V. M. Ghete, I. Giomataris, G. Giroux, A. Giuliani, C. Giunti, P. Gorel, C. Goupy, J. Goupy, C. Goy, M. P. Green, M. Gros, C. Guerin, V. Guidi, O. Guillaudin, E. Guy, C. Ha, D. Hauff, J. Hakenmuller, P. M. Harrington, S. Hedges, S. T. Heine, S. Hertel, M. Heusch, C. Hoarau, M. Hoferichter, E. W. Hoppe, Z. Hong, S. Horiuchi, P. Huber, J. C. Ianigro, N. Jachowicz, E. Jericha, Y. Jin, J. P. Johnston, A. Juillard, I. Katsioulas, S. Kazarcev, M. Kaznacheeva, F. Kelly, K. J. Kelly, D. Kim, A. Kinast, L. Klinkenberg, H. Kluck, P. Knights, Y. J. Ko, T. S. Kosmas, L. Kwon, J. Lamblin, R. F. Lang, A. Langenkamper, S. Langrock, T. Lasserre, H. Lattaud, P. Lautridou, H. S. Lee, B. G. Lenardo, D. Lhuillier, M. Li, S. C. Li, Y. F. Li, Z. Li, M. Lindner, J. Liu, D. Loomba, A. Lubashevskiy, P. A. N. Machado, M. Mancuso, W. Maneschg, D. M. Markoff, S. Marnieros, R. Martin, R. D. Martin, B. Mauri, D. W. Mayer, A. Mazzolari, E. Mazzucato, J. Menendez, J. Minet, O. G. Miranda, D. Misiak, J. P. Mols, A. Monfardini, F. Mounier, J. F. Muraz, T. Neep, R. Neilson, J. Newby, J. L. Newstead, H. Neyrial, K. Ni, K. Nikolopoulos, C. Nones, D. Norcini, V. Pandey, P. O'Brien, C. A. J. O'Hare, L. Oberauer, W. Oliver, E. Olivieri, A. Onillon, C. Oriol, T. Ortmann, R. Owen, K. J. Palladino, D. K. Papoulias,

J. C. Park, D. S. Parno, P. K. Patel, L. Pattavina, E. Peinado, E. Perbet, L. Peters, F. Petricca, H. D. Pinckney, M. C. Piro, D. Ponomarev, D. Poda, W. Potzel, F. Probst, F. Pucci, F. Rarbi, R. Rapp, H. Ray, J. S. Real, F. Reindl, G. C. Rich, J. S. Ricol, T. Rink, T. Redon, R. Rogly, A. Robert, J. Rothe, S. Rozov, I. Rozova, T. Salagnac, E. S. Garcia, G. S. Garcia, O. Sanders, V. Sanglard, D. Santos, Y. Sarkis, V. Savu, G. Savvidis, I. Savvidis, N. Schermer, J. Schieck, B. Schmidt, S. Schonert, K. Scholberg, A. Schwenk, C. Schwertner, L. Scola, Y. Shevchik, S. Shin, V. Sibille, I. M. Shoemaker, D. P. Snowden-Ifft, T. Soldner, G. Soum, N. J. C. Spooner, J. Stachurska, L. Stodolsky, R. Strauss, L. E. Strigari, A. Stutz, B. D. Suh, J. Suhonen, Z. Tabrizi, V. Takhistov, A. Thompson, C. Tomei, M. Tortola, M. Tripathi, L. Vagneron, J. W. F. Valle, K. v. Mirbach, W. Van De Ponteseele, M. Vignati, M. Vivier, F. V. d. S. Fernandez, F. Vezzu, M. Vidal, V. Wagner, J. W. Walker, R. Ward, A. Wex, L. Winslow, H. T. Wong, M. H. Wood, J. Xu, L. Yang, E. Yakushev, M. Zampaolo, J. Zettlemoyer, Y. Y. Zhang, and D. Zinatulina, "Coherent elastic neutrino-nucleus scattering: Terrestrial and astrophysical applications", Publisher: arXiv Version Number: 1, `10.48550/ARXIV.2203.07361` (2022) (cit. on p. 66).

[108]   G. S. Agarwal, *Quantum Optics* (Cambridge University Press, 2012) (cit. on p. 67).

[109]   M. D. Schwartz, *Quantum field theory and the standard model* (Cambridge University Press, New York, 2014) (cit. on p. 69).

[110]   M. R. Gallis and G. N. Fleming, "Environmental and spontaneous localization", Physical Review A **42**, 38–48 (1990) (cit. on pp. 75, 95, 97).

[111]   D. Lunney, J. M. Pearson, and C. Thibault, "Recent trends in the determination of nuclear masses", Reviews of Modern Physics **75**,

Publisher: American Physical Society, 1021–1082 (2003) (cit. on p. 76).

[112]   A. C. Hayes and P. Vogel, "Reactor Neutrino Spectra", Annual Review of Nuclear and Particle Science **66**, 219–244 (2016) (cit. on p. 76).

[113]   Y. Kim, "Detection of Antineutrinos for Reactor Monitoring", Nuclear Engineering and Technology **48**, 285–292 (2016) (cit. on p. 76).

[114]   M. A. Nielsen and I. L. Chuang, *Quantum computation and quantum information*, 10th anniversary ed (Cambridge University Press, Cambridge ; New York, 2010) (cit. on p. 78).

[115]   M. Zhong, M. P. Hedges, R. L. Ahlefeldt, J. G. Bartholomew, S. E. Beavan, S. M. Wittig, J. J. Longdell, and M. J. Sellars, "Optically addressable nuclear spins in a solid with a six-hour coherence time", Nature **517**, Publisher: Nature Publishing Group, 177–180 (2015) (cit. on p. 83).

[116]   D. E. Chang, C. Regal, S. Papp, D. Wilson, J Ye, O Painter, H. J. Kimble, and P Zoller, "Cavity opto-mechanics using an optically levitated nanosphere", Proceedings of the National Academy of Sciences **107**, Publisher: National Acad Sciences, 1005–1010 (2010) (cit. on p. 83).

[117]   Y.-L. Chan, M.-C. Chu, K. M. Tsui, C. F. Wong, and J. Xu, "Wave-packet treatment of reactor neutrino oscillation experiments and its implications on determining the neutrino mass hierarchy", The European Physical Journal C **76**, 310 (2016) (cit. on p. 87).

[118]   S. Rajendran, N. Zobrist, A. O. Sushkov, R. Walsworth, and M. Lukin, "A method for directional detection of dark matter using spectroscopy of crystal defects", Physical Review D **96**, 035009 (2017) (cit. on p. 87).

[119]   H. Zhao and J. B. Freund, "Full-spectrum phonon relaxation times
        in crystalline Si from molecular dynamics simulations", Journal of
        Applied Physics **104**, Publisher: American Institute of Physics,
        033514 (2008) (cit. on p. 88).

[120]   E. Kilian, M. Toroš, P. F. Barker, and S. Bose, "Optimal Super-
        positions for Particle Detection via Quantum Phase", Publisher:
        arXiv Version Number: 1, `10.48550/ARXIV.2307.15186` (2023)
        (cit. on p. 92).

[121]   L. Pezzè, A. Smerzi, M. K. Oberthaler, R. Schmied, and P. Treut-
        lein, "Quantum metrology with nonclassical states of atomic en-
        sembles", Rev. Mod. Phys. **90**, Publisher: American Physical So-
        ciety, 035005 (2018) (cit. on p. 93).

[122]   S. Qvarfort, A. Serafini, P. F. Barker, and S. Bose, "Gravimetry
        through non-linear optomechanics", Nature Communications **9**,
        3690 (2018) (cit. on p. 93).

[123]   Y. Bidel, N. Zahzam, C. Blanchard, A. Bonnin, M. Cadoret, A.
        Bresson, D. Rouxel, and M. F. Lequentrec-Lalancette, "Absolute
        marine gravimetry with matter-wave interferometry", Nature Com-
        munications **9**, 627 (2018) (cit. on p. 93).

[124]   B. Stray, A. Lamb, A. Kaushik, J. Vovrosh, A. Rodgers, J. Winch,
        F. Hayati, D. Boddice, A. Stabrawa, A. Niggebaum, M. Langlois,
        Y.-H. Lien, S. Lellouch, S. Roshanmanesh, K. Ridley, G. de Vil-
        liers, G. Brown, T. Cross, G. Tuckwell, A. Faramarzi, N. Metje,
        K. Bongs, and M. Holynski, "Quantum sensing for gravity cartog-
        raphy", Nature **602**, 590–594 (2022) (cit. on p. 93).

[125]   S. C. Burd, R. Srinivas, J. J. Bollinger, A. C. Wilson, D. J. Wineland,
        D. Leibfried, D. H. Slichter, and D. T. C. Allcock, "Quantum am-
        plification of mechanical oscillator motion", Science **364**, _eprint:

https://www.science.org/doi/pdf/10.1126/science.aaw2884, 1163–1165 (2019) (cit. on p. 93).

[126] E. Joos and H. D. Zeh, "The emergence of classical properties through interaction with the environment", Zeitschrift für Physik B Condensed Matter **59**, 223–243 (1985) (cit. on p. 95).

[127] A. Sørensen and K. Mølmer, "Entanglement and quantum computation with ions in thermal motion", Phys. Rev. A **62**, Publisher: American Physical Society, 022311 (2000) (cit. on p. 107).

[128] F. Mintert and C. Wunderlich, "Ion-Trap Quantum Logic Using Long-Wavelength Radiation", Phys. Rev. Lett. **87**, Publisher: American Physical Society, 257904 (2001) (cit. on p. 108).

[129] M. Toroš, S. Bose, and P. F. Barker, "Creating atom-nanoparticle quantum superpositions", Phys. Rev. Res. **3**, Publisher: American Physical Society, 033218 (2021) (cit. on p. 109).

[130] J. Gieseler, B. Deutsch, R. Quidant, and L. Novotny, "Subkelvin Parametric Feedback Cooling of a Laser-Trapped Nanoparticle", Phys. Rev. Lett. **109**, Publisher: American Physical Society, 103603 (2012) (cit. on pp. 110, 119).

[131] J. Vovrosh, M. Rashid, D. Hempston, J. Bateman, M. Paternostro, and H. Ulbricht, "Parametric feedback cooling of levitated optomechanics in a parabolic mirror trap", Journal of the Optical Society of America B **34**, Publisher: Optica Publishing Group, 1421–1428 (2017) (cit. on p. 110).

[132] D. Carney, G. Krnjaic, D. C. Moore, C. A. Regal, G. Afek, S. Bhave, B. Brubaker, T. Corbitt, J. Cripe, N. Crisosto, and others, "Mechanical quantum sensing in the search for dark matter", Quantum Science and Technology **6**, Publisher: IOP Publishing, 024002 (2021) (cit. on p. 113).

[133] S. A. Buyukasik and Z. Cayic, "Time-evolution of squeezed coherent states of a generalized quantum parametric oscillator", Journal of Mathematical Physics **60**, 062104 (2019) (cit. on p. 117).

[134] V. B. Braginsky, F. Y. Khalili, and K. S. Thorne, *Quantum Measurement* (Cambridge University Press, Cambridge, 1992) (cit. on p. 118).

[135] D. F. Walls and G. J. Milburn, "Effect of dissipation on quantum coherence", Phys. Rev. A **31**, Publisher: American Physical Society, 2403–2408 (1985) (cit. on p. 118).

[136] M. Ivory, W. J. Setzer, N. Karl, H. McGuinness, C. DeRose, M. Blain, D. Stick, M. Gehl, and L. P. Parazzoli, "Integrated Optical Addressing of a Trapped Ytterbium Ion", Phys. Rev. X **11**, Publisher: American Physical Society, 041033 (2021) (cit. on p. 118).

[137] A. Pontin, H. Fu, M. Toroš, T. S. Monteiro, and P. F. Barker, "Simultaneous cavity cooling of all six degrees of freedom of a levitated nanoparticle", Nature Physics, `10.1038/s41567-023-02006-6` (2023) (cit. on p. 119).

[138] L.-M. Duan, G. Giedke, J. I. Cirac, and P. Zoller, "Entanglement Purification of Gaussian Continuous Variable Quantum States", Phys. Rev. Lett. **84**, Publisher: American Physical Society, 4002–4005 (2000) (cit. on p. 119).

[139] B. Yi, U. Sinha, D. Home, A. Mazumdar, and S. Bose, *Massive Spatial Qubits for Testing Macroscopic Nonclassicality and Casimir Induced Entanglement*, arXiv:2106.11906 [quant-ph], Sept. 2021 (cit. on pp. 120, 121, 123).

[140] G. Taguchi, T. Dougakiuchi, N. Yoshimoto, K. Kasai, M. Iinuma, H. F. Hofmann, and Y. Kadoya, "Measurement and control of spatial qubits generated by passing photons through double slits",

Phys. Rev. A **78**, Publisher: American Physical Society, 012307 (2008) (cit. on p. 120).

[141]   A. K. Chauhan, O. Cernotik, and R. Filip, "Tuneable Gaussian entanglement in levitated nanoparticle arrays", npj Quantum Information **8**, 151 (2022) (cit. on p. 128).

[142]   J. Rieser, M. A. Ciampini, H. Rudolph, N. Kiesel, K. Hornberger, B. A. Stickler, M. Aspelmeyer, and U. Delić, "Tunable light-induced dipole-dipole interaction between optically levitated nanoparticles", Science **377**, Publisher: American Association for the Advancement of Science, 987–990 (2022) (cit. on p. 130).